A hybrid spectral element method for the time domain solution of wave scattering problems.

Davies, Richard Wyn

Davies, Richard Wyn (2007) *A hybrid spectral element method for the time domain solution of wave scattering problems..* thesis, Swansea University.
http://cronfa.swan.ac.uk/Record/cronfa42272

Swansea University
Prifysgol Abertawe

A Hybrid Spectral Element Method for the Time Domain Solution of Wave Scattering Problems

Richard Wyn Davies

Thesis submitted to Swansea University
in candidature for the degree of Doctor of Philosophy

25th October 2007

Civil and Computational Engineering Centre
School of Engineering
Swansea University
Singleton Park, Swansea SA2 8PP
Wales, United Kingdom

Acknowledgements

Over the past three years, Professor Ken Morgan's guidance has been of paramount importance to the formulation and execution of this research work. His vast knowledge and experience of numerous mathematical, scientific and engineering fields has been evident throughout and has been matched by his willingness to share his thoughts and assist whenever possible. I would also like to express my appreciation for his time, opinions and advice during the preparation of this thesis and make note of his cheerful and kind manner, ensuring that my time as a postgraduate researcher has been both enjoyable and fulfilling.

My gratitude must also extend to Professor Oubay Hassan, who's knowledge in the fields of fluid mechanics, computational methods and mesh generation, to name but a few, has proved invaluable.

Within the Civil & Computational Engineering Centre, I would also like to thank Dr Paul Ledger, Dr Jason Jones and Dr Mohammed El Hachemi for their assistance during the course of this work.

Finally, I end by expressing my utmost gratitude to my family and friends, especially to my parents, Euros and Liz, my sister, Catrin, and my girlfriend, Alex, who have provided support and encouragement throughout and in every aspect of my life. Thank you.

Summary

This thesis considers the development and analysis of a hybrid spectral element method for the solution of two-dimensional wave scattering problems in the time domain. The components, namely a quadrilateral formulation of the diagonal mass matrix spectral element method and a triangular formulation of the spectral discontinuous Galerkin finite element method, are introduced and tested separately before being coupled to form the final hybrid procedure. Subsequently, a simple circular scattering problem is analysed to validate the computational model and various methods of curved boundary representation are tested to assess their impact on solution accuracy. Finally, a range of two-dimensional wave scattering problems are modelled, showing the computational efficiency of the higher order approximation in comparison with low order linear models.

Contents

List of Figures

List of Tables

Nomenclature

$\boldsymbol{A}, \boldsymbol{B}$	Jacobian matrices in x and y
A^e	Element area
α	Time-stepping parameter
$\boldsymbol{B}$	Magnetic flux density
$\boldsymbol{B}$	Iterative matrix
C_{IJ}	Convection matrix component
c_0	Speed of wave propagation
c_n, d_n	Amplitude coefficients
$\boldsymbol{D}$	Electric flux density
$\boldsymbol{E}$	Electric field intensity
e	Specific internal energy
ε	Dielectric permittivity
$\boldsymbol{F}, \boldsymbol{G}, \boldsymbol{H}$	Flux vector components in x, y and z
f	Arbitrary function
f_i	Flux vector component
g_i	Polynomial basis
Γ	Problem domain boundary
$\boldsymbol{H}$	Magnetic field intensity
$H_n^{(1)}, H_n^{(2)}$	Hankel functions of the first and second kinds
H	Hilbert space
h	Polynomial approximation
h_x, h_y	Quadrilateral element length in x and y
i	Imaginary unit
$\|\|I_N\|\|$	Lebesgue constant of degree N
$\boldsymbol{J}$	Jacobian spatial transformation

$\boldsymbol{J_c}$	Electric current density
J_n	Bessel function of the first kind of order n
K_{IJ}	Diffusion matrix component
$\boldsymbol{k}$	Wavenumber
k	Diffusion coefficient
L, M	Linear differential operators
M_{IJ}	Mass matrix component
$\boldsymbol{M}^S$	Magnetic current
μ	Magnetic permeability
$\boldsymbol{n}$	Computational boundary normal vector
$\boldsymbol{N}$	Physical boundary normal vector
N_I, P_I, Q_I	Interpolation functions
(ξ, η)	Computational space coordinates
p	Pressure
$\boldsymbol{\Phi}, \boldsymbol{\Psi}$	Function spaces
ϕ	Unknown scalar variable
$\boldsymbol{R}$	Typical right hand side vector
(r, ϕ, z)	Cylindrical coordinates
ρ	Density
ρ_v	Electric charge density
S	Arbitrary surface
S_i	Source term
σ	Electric conductivity
t	Time
u, v, w	Velocity components in x, y and z
$\boldsymbol{U}$	Unknown vector
$\boldsymbol{V}$	Vandermonde matrix
V	Speed
W	Weighting function

(x, y, z)	Cartesian coordinates
$\chi(\phi)$	Scattering width
Y_n	Bessel function of the second kind of order n
Z_n	General Bessel function of order n
ω	Angular frequency
Ω	Problem domain

Chapter 1

Introduction

1.1 Waves: A Brief Introduction

Wave scattering and propagation occur in many different forms and, as a consequence, are of interest in a diverse range of research fields. Governed by typical experiences, the waveforms with which we are naturally most familiar are likely to be those that we see in our everyday lives, such as surface waves on a lake or compression waves travelling along a spring. However, it could be argued that our lives are more profoundly affected by those waves which may be slightly harder to visualise.

With recent technological advances, such as mobile communications and wireless networks, our exposure to electromagnetic fields has become commonplace in every environment: from home to office, both indoors and out. Passing through such fields on a regular basis, their possible effects on the human body has become a keenly debated and controversial topic, leading to extensive medical research and governmental advice.

These electromagnetic fields, which emanate from various electronic and electrical devices, can also interact with each other. A well known example where this occurrence can be dangerous is the use of mobile phones whilst aboard an aeroplane. The possibility that the signals required to make a phone call could affect the onboard circuitry controlling the aircraft is enough to warrant legislation to forbid such an act.

Although possibly unfortunate to experience at first-hand, an example that may be easier to feel, if not see, are the waves caused by an earthquake. The movement and collision of the tectonic plates, which comprise the outer layer of Earth's crust, can cause vast amounts of energy to be transported as elastic waves. These waves propagate from the site of the initial disturbance to further afield. As seen frequently on international news broadcasts, these events can cause devastation to nearby populated areas as the waves destroy buildings and infrastructure, potentially leading to a significant loss of life.

However, the intention is not to dishearten the reader at this early stage. There are, of course, numerous examples to consider where the outcomes are more beneficial. Firstly, it should be noted, that the problems associated with the electromagnetic wave examples cited above are the accepted relatively minor risks of a technology that would be unimaginably missed if taken from us. Furthermore, these waves can be used to our advantage in various ways, including, for example, the detection of objects and features which would be practically impossible by any other means.

To control and maintain the safe passage of millions of commuters every year, civilian radar systems are used by air-traffic control service providers to guide aeroplanes through the sky. Radar systems work by measuring the electromagnetic scattering profile generated by the surface of an aircraft. Therefore, due to the volume of traffic, they must be able to identify and distinguish between various objects that they encounter. While military radar systems endeavour to provide the same information, the nature of military activities often require that the radar profile of its aircrafts be minimised in the hope of gaining some strategic advantage.

A similar technique, where electromagnetic waves are used to illuminate undercover objects and the resulting scattering pattern is observed and recorded to facilitate recognition, is used in geophysical exploration. This is useful for both military applications, where hidden land mines can be found, and for such scientific and leisure activities as performed in the field of archeology. An analogous acoustic example, related to the propagation and scattering of mechanical pressure waves, is the use of sonar. In this case, the technique identifies hidden objects from the scattering of incident pressure waves and, for example, is commonly used in the marine environment.

Both types of wave, electromagnetic and acoustic, are also used extensively for medical applications. These offer a means by which non-intrusive examinations can take place, thus minimising the discomfort and apprehension felt by the patient. Furthermore, similar techniques are used frequently in other fields where intrusive examinations would be equally impractical or undesirable, such as the detection of faults or defects in a completed building structure.

It is obvious, therefore, that there are numerous scientific and industrial fields where wave scattering and propagation are of paramount importance. The brief introduction given above provides only an indication of the variety of research concerning this physical phenomenon.

1.2 Methods of Analysis

Having identified some of the possible fields of research in which wave scattering provides considerable interest, we will now look at the general methods used by scientists and engineers to analyse this behaviour.

1.2.1 Experimental and Theoretical Analysis

For fundamental wave scattering models, involving simple geometries, theoretical procedures are a viable method of analysis and provide accurate expressions for scattering solutions. However, this confined area of application proves overly restrictive, as their use for more practical models, where the geometries are typically more complex, is unsuitable.

Therefore, in the past, experimental methods of analysis were very popular, being the only feasible method of replicating more complex problems. Given sufficient amounts of time and financial resources, any model could be set-up and analysed. However, in industry, as these quantities are strictly limited, this brought about other limitations. Considering the example of aircraft development, for every modification in design, a new carefully crafted model would be required, providing a suitably scaled replica with accurate material properties. Taking both time and money to prepare, this would inhibit and delay the initial stages of the design and development process: a crucial phase required to ensure that the expenses of later development and manufacturing work are not wasted on an inferior or faulty design.

1.2.2 Computational Analysis

Necessity being the mother of invention, faster and more economical methods were sought. At a time when computer technology was beginning to infiltrate the commercial and industrial worlds, the mid 20^{th} century witnessed the first examples of practical large-scale numerical analyses. These methods brought forth the capability to examine various aspects of a physical problem by simply changing a few commands or parameters in a computer program. Saving time and the preparation cost of a physical replica, computational analysis was seen to be ideally suited to the initial development phase. Furthermore, with time, as the numerical methods became more accurate and reliable, every aspect of the design could conceivable be completed without a single physical experiment.

Due to the vast range of research fields and the diversity of computational techniques used in each, it would be impossible to cover all of the numerical schemes devised and used since the advent of this analysis method. However, in the section that follows, an attempt is made to introduce the reader to the most pertinent methods used in the fields of wave scattering research. This, hopefully, will set the scene for the research work presented in this thesis.

1.3 Existing Computational Methods

Initially, in search of an appropriately simple form of wave scattering to permit the progression of this work, the scattering and propagation considered here will primarily be of acoustic waves. However, as will be seen in the remainder of this thesis, the simplifications applied to the governing equations, introduced in Chapter 2, enable direct application of the computational model to another field, namely electromagnetic wave scattering. Therefore, the results presented in the later chapters will be increasingly directed towards this field. It should also be noted that similar connections could also be made to other fields, such as the analysis of elastic wave scattering considered in geodynamics. This serves to enlarge the scope of previous research of relevance to this work, a fact which will be reflected in this review.

In the infancy of computational simulation, one of the most popular numerical techniques was the finite difference method. The fundamental simplicity of this approach made it an obvious starting point in this emerging discipline. Therefore, until recently in the field of electromagnetics, the most popular numerical scheme for the solution of Maxwell's governing equations was that proposed by Yee in the 1960s [1]. Using an efficient leapfrog finite difference technique, this scheme used the structure of the governing equations to obtain a second order accurate pointwise approximation on equidistant staggered grids. However, as time progressed and the modelling requirements in the field of electromagnetics became more intense, the application of the simple Yee scheme to these newer problems became less suitable. With increasingly complex models came more intricate, possibly curved, boundaries and enlarged electrical lengths: a measure of the size of a scattering object in relation to the length of the incident electromagnetic wave. Numerous modifications to this original scheme were derived in an attempt to resolve these difficulties, some of which can be found in [2, 3, 4, 5]. However, the additional complication of the scheme negated its original advantage and, in conjunction with the inherent limitation of pointwise approximation, the use of other numerical methods was investigated.

As such, the wealth of computational procedures employed in other areas of research provided a good foundation to begin this search. Within the field of computational fluid dynamics, volume based methods, such as the the finite element and finite volume schemes, have seen much success and development. In particular, the finite element method [6], which in general terms can actually be considered as the top-tier method encompassing both finite difference and finite volume techniques [7], has proved very flexible and robust. Initially developed for structural analysis in the aerospace industry, its use has spread to almost every corner of computational mechanics research. One of its main strengths is that it can be used upon unstructured meshes, thus enabling the solution of problems with complex geometries. Therefore, in light of these properties, successful initial attempts were made showing the possible transfer of this technique to the electromagnetics field, an example of which can be seen in [8].

Yet, to satisfy the requirements noted above, further development of the finite element procedure was needed. Due to the increasing electrical size of the scattering models, the level of refinement with standard linear (or bi-linear) elements quickly becomes overly restrictive. Therefore, the obvious progression was an increase in approximation order. Over the past 20 years, the development of higher order finite element schemes has been the common goal of an extensive range of research work [9]. A vast number of schemes, aimed at the solution of Maxwell's equations in the frequency domain, have been investigated, a selection of which can be found in [10, 11, 12]

For the time domain solution of electromagnetic wave scattering problems, the development of spectral discontinuous Galerkin (DG) approximations has been most significant, with key contributions from Hesthaven and Warburton [13] and, for more general convection dominated problems, Cockburn and Shu [14]. Further details of the range of methods used for the time-domain solution of Maxwell's equations are available in the comprehensive review [15]. Work of a similar high-order nature encountered in the geodynamics field for elastic wave scattering [16, 17, 18] has seen greater emphasis on continuous Galerkin finite element procedures, following the foremost work of Patera on the spectral element method (SEM) for fluid flow [19]. Extension of this method to triangular elements, based on the use of Fekete points, has also been achieved [20, 21].

Some other interesting fields of research in which these high order spectral element methods are employed include oceanic shallow water models [22] and atmospheric modelling for numerical weather prediction [23].

Work concerning various aspects of the boundary representation within the computational model has also been acknowledged to be of equal importance. Appropriate truncation methods for the infinite domains encountered in external wave scattering problems have been given significant attention, ranging from the early first order accurate differential absorbing boundary conditions [24, 25] to more recent work centering on the perfectly matched layer (PML) as formulated by Berenger for electromagnetic models [26]. Numerous adaptations of this technique have since been presented, examples of which can be seen in [27, 28, 29, 30]. Furthermore, the need for accurate representation of curved scattering surfaces has also been confirmed [31, 32, 33].

1.4 Requirements of the Model

The ultimate goal of this work would be the analysis of the complex scattering geometries encountered in industrial applications. As mentioned previously, the requirements of such physical models are high and thus govern the desirable properties of the computational method. Due to the relative size of the scattering objects compared with the wavelength of the incident field and the potentially intricate scattering boundaries, the proposed approximation procedure must possess the following attributes: be able to resolve complex boundaries, maintain the accuracy of the waveform over many cycles and perform the computations in an efficient manner.

To achieve this, a hybrid solution procedure is proposed, which applies a higher order finite element method to both triangular and quadrilateral elements. It is hoped that this formulation will permit the high fidelity to the scattering geometry required for accurate approximations, while minimising unwarranted computational expense.

1.5 Thesis Composition

To ensure that the proposed hybrid solution method is developed and validated in a structured and transparent manner, the main components of the procedure are initially separated, to facilitate their discussion. Subsequently, these components are combined and an analysis of the complete hybrid procedure is performed.

As further clarification of the contents of this thesis, a summary is provided here describing the work contained within each of the following chapters.

Chapter 2 is divided into two main parts. In the first part, the governing equations for both acoustic and electromagnetic waves are introduced. Subsequently, the simplifications applied to each set are explained, leading to a discussion of the correspondence of these simplified equations. Analytical solutions for comparison with the approximations generated in later chapters are also obtained. The second part is devoted to a brief introduction of the finite element method. This includes a discussion of its application to convection-dominated problems and the methods of overcoming the possible instability.

In Chapter 3 the first component of the proposed hybrid solution procedure is examined, namely the spectral element method. Formulations are derived for both quadrilateral and triangular elements, including, in the latter case, a proposed mass iteration scheme intended to improve the accuracy of the solution within the triangular discretisation. However, the iterative method used here is discovered to be unstable for higher order approximations. Therefore, it is concluded that an alternative procedure is required for the triangular discretisation, to be discussed in the following chapter. Meanwhile, validation of the quadrilateral implementation continues.

In Chapter 4 a spectral discontinuous Galerkin method is put forward as an alternative solution procedure on triangular elements. Validation of the method is performed with the same simple model as for the SEM in the previous chapter.

Having presented and tested each component of the proposed hybrid method separately, Chapter 5 summarises the complete formulation and repeats the validation procedure. Further components of the model, including the PML and curved boundary representation, are addressed to complete the essential elements needed to analyse wave scattering problems. Subsequently, an initial example of wave scattering from a circular object is attempted, thus enabling comparison with an analytical solution. A further, more complex circular model of larger electrical length is also used to ensure that the hybrid procedure is performing adequately. Finally, an initial assessment of the potential computational efficiency of the higher order approximations is made. This is achieved by comparison with linear models using equivalent levels of discretisation.

With the hybrid solution procedure in place, further examples of increasing complexity are analysed in Chapter 6. These include scattering from a dihedral object, an open cavity, a two-dimensional cross-section of a NACA0012 aerofoil and a simple multi-object scattering example. Further assessments of computational efficiency are attempted for each of these models.

To finish, in Chapter 7, we review the work that has been completed, noting the conclusions which can be drawn. This is accompanied by some suggestions for further work, which could extend the capabilities of the current model.

Chapter 2

Governing Equations and Solution Procedures

2.1 Introduction

This chapter consists of two main parts. The first will begin with an introduction to the governing equations applicable to the various fields under consideration. Subsequently, derivation of the simplified equations, used in the production and validation of the numerical models, is conducted for several reasons: to demonstrate the origins of the equations, the assumptions made to facilitate generation of the model and, hopefully, to enable the reader to appreciate possible extensions of the method or applications in other areas.

In the second part, we turn our attention to the finite element solution procedure. As the basis of the solution methods used in this thesis, an introduction and description of the general theory will be given. Subsequently, the convective nature of the problems considered here and the associated instabilities which can occur when standard finite element procedures are applied to their solution are discussed. Consequently, an explanation will be given of the stabilisation method used here to overcome these undesirable effects.

2.2 Acoustic Equations

2.2.1 Linearized Euler Equations

The governing equations for acoustic waves are the linearized Euler equations of fluid flow. The full non-linear Euler equations, shown here in strong conservation form for a Cartesian coordinate system

$$\frac{\partial \boldsymbol{U}}{\partial t} + \frac{\partial \boldsymbol{F}}{\partial x} + \frac{\partial \boldsymbol{G}}{\partial y} + \frac{\partial \boldsymbol{H}}{\partial z} = 0 \tag{2.1}$$

where

$$\begin{aligned}
\boldsymbol{U} &= [\rho\ , \rho u\ , \rho v\ , \rho w\ , \rho(e + \frac{V^2}{2})]^T \\
\boldsymbol{F} &= [\rho u\ , \rho u^2 + p\ , \rho v u\ , \rho w u\ , \rho(e + \frac{V^2}{2})u + pu]^T \\
\boldsymbol{G} &= [\rho v\ , \rho u v\ , \rho v^2 + p\ , \rho w v\ , \rho(e + \frac{V^2}{2})u + pv]^T \\
\boldsymbol{H} &= [\rho w\ , \rho u w\ , \rho v w\ , \rho w^2 + p\ , \rho(e + \frac{V^2}{2})u + pw]^T
\end{aligned}$$

are themselves a simplification of the governing equations of general viscous fluid flow, namely the Navier-Stokes equations, and are obtained by neglecting viscous and heat transfer effects. Reducing this set of equations by considering only two spatial dimensions and by making the assumption that we are dealing with an isentropic flow, the Euler equations become

$$\frac{\partial \boldsymbol{U}}{\partial t} + \frac{\partial \boldsymbol{F}}{\partial x} + \frac{\partial \boldsymbol{G}}{\partial y} = 0 \tag{2.2}$$

where the vector variables are

$$\begin{aligned}
\boldsymbol{U} &= [\rho\ , \rho u\ , \rho v]^T \\
\boldsymbol{F} &= [\rho u\ , \rho u^2 + p\ , \rho v u]^T \\
\boldsymbol{G} &= [\rho v\ , \rho u v\ , \rho v^2 + p]^T
\end{aligned}$$

and the scalar components of these vectors are the density, ρ, the pressure, p, and the fluid velocities, u and v, in the x and y directions respectively. In this system, the first equation represents continuity, while the second and third are the momentum equations in the x and y coordinate directions. Linearization of these equations can now be performed by expressing the dependent variables in terms of small variations from a time-averaged value, for which the time-averaged pressure and velocity are taken as zero: $\rho = \rho_0 + \rho'$, $p = p'$, $u = u'$ and $v = v'$. Subsequently, substitution of these variables into (2.2), noting that the prime used to indicate the small variation in the variables has been removed for clarity and that all unknowns in these equations now represent small variations from the time-averaged quantity, leads to the linearized Euler equations

$$\frac{\partial \rho}{\partial t} + \rho_0 \frac{\partial u}{\partial x} + \rho_0 \frac{\partial v}{\partial y} = 0 \tag{2.3a}$$

$$\frac{\partial p}{\partial x} + \rho_0 \frac{\partial u}{\partial t} = 0 \tag{2.3b}$$

$$\frac{\partial p}{\partial y} + \rho_0 \frac{\partial v}{\partial t} = 0 \tag{2.3c}$$

Furthermore, as our assumptions include that of isentropic flow, we can use the equality

$$c_0^2 = \left.\frac{\partial p}{\partial \rho}\right|_S \tag{2.4}$$

taken along a streamline S, where c_0 represents the speed of wave propagation, to remove the density variable from the linearized continuity equation. With the additional assumptions of unit time-averaged density, ρ_0, and wave speed, c_0, the equations ultimately become

$$\frac{\partial p}{\partial t} = -\left(\frac{\partial u}{\partial x} + \frac{\partial v}{\partial y}\right) \tag{2.5a}$$

$$\frac{\partial v}{\partial t} = -\frac{\partial p}{\partial y} \tag{2.5b}$$

$$\frac{\partial u}{\partial t} = -\frac{\partial p}{\partial x} \tag{2.5c}$$

2.2.2 Scalar Wave Equation

Additionally, the linearised Euler equation system can also be combined into a single second order partial differential equation. Once again, applying the isentropic condition (2.4) to (2.3a) yields

$$\frac{1}{c_0^2}\frac{\partial p}{\partial t}+\rho_0\frac{\partial u}{\partial x}+\rho_0\frac{\partial v}{\partial y}=0$$

Taking the temporal derivative of this expression and rearranging the derivatives of the second and third terms gives

$$\frac{1}{c_0^2}\frac{\partial^2 p}{\partial t^2}+\frac{\partial}{\partial x}\left(\rho_0\frac{\partial u}{\partial t}\right)+\frac{\partial}{\partial y}\left(\rho_0\frac{\partial v}{\partial t}\right)=0$$

which, upon substitution of (2.3b,2.3c), leads ultimately to the classical scalar wave equation

$$\frac{1}{c_0^2}\frac{\partial^2 p}{\partial t^2}=\frac{\partial^2 p}{\partial x^2}+\frac{\partial^2 p}{\partial y^2} \tag{2.6}$$

This provides an alternative equation for modelling acoustic wave propagation. Research work, previously conducted in [34], concerning the numerical solution of these various forms of the wave equations demonstrated that the equation system (2.3) offers a good alternative to the scalar wave equation (2.6) when modelling wave propagation problems and, hence, will be the chosen form for this work.

2.3 Maxwell's Equations

Maxwell's equations in general differential form can be expressed as

$$\nabla\cdot\boldsymbol{D}=\rho_\nu \tag{2.7a}$$

$$\nabla\cdot\boldsymbol{B}=0 \tag{2.7b}$$

$$\nabla\times\boldsymbol{E}=-\frac{\partial\boldsymbol{B}}{\partial t} \tag{2.7c}$$

$$\nabla\times\boldsymbol{H}=\boldsymbol{J}_c+\frac{\partial\boldsymbol{D}}{\partial t} \tag{2.7d}$$

where $\boldsymbol{E}$ and $\boldsymbol{H}$ are the electric and magnetic field intensities respectively, $\boldsymbol{D}$ and $\boldsymbol{B}$ are the electric and magnetic flux densities respectively, $\boldsymbol{J}_c$ is the electric current density and ρ_ν is the electric charge density. The set is completed by the addition of four auxiliary vector equations;

the continuity equation

$$\nabla \cdot \boldsymbol{J}_c + \frac{\partial \rho_\nu}{\partial t} = 0 \tag{2.8a}$$

and three constitutive equations

$$\boldsymbol{D} = \varepsilon \boldsymbol{E} \tag{2.8b}$$

$$\boldsymbol{B} = \mu \boldsymbol{H} \tag{2.8c}$$

$$\boldsymbol{J}_c = \sigma \boldsymbol{E} \tag{2.8d}$$

where ε is the permittivity, μ is the permeability and σ is the conductivity. In this work, the above set of 8 vector equations are simplified by assuming the following conditions;

i. The electric charge density is zero $\rho_\nu = 0$

ii. Problems will be electrically and magnetically homogeneous and isotropic

ii. The conductivity of the materials is negligible $\sigma = 0$ [1]

With these assumptions, the governing system of equations for electromagnetics become

$$\nabla \cdot \boldsymbol{E} = 0 \tag{2.9a}$$

$$\nabla \cdot \boldsymbol{H} = 0 \tag{2.9b}$$

$$\nabla \times \boldsymbol{E} = -\mu \frac{\partial \boldsymbol{H}}{\partial t} \tag{2.9c}$$

$$\nabla \times \boldsymbol{H} = \varepsilon \frac{\partial \boldsymbol{E}}{\partial t} \tag{2.9d}$$

Furthermore, if (2.9a,2.9b) hold initially, then they can be shown to hold for all time. Consequently, consideration can be focused solely upon (2.9c,2.9d) as the first two equations will, in theory, be satisfied automatically.

---

[1] The reader should note that this assumption will not hold in the perfectly matched layer region, as can be seen within the formulation in Section 5.4, in which the conductivity is used as an artificial absorption parameter.

2.3.1 TM^z Polarization

A transverse magnetic polarization to the z-axis (TM^z) assumes that the magnetic field oscillations can occur only in the x-y plane. Correspondingly, as electric and magnetic field oscillations are orthogonal, the only non-zero component of the electric field must lie in the z-axis. Therefore, the magnetic and electric field vectors can be expressed as $\boldsymbol{H} = [H_x \ H_y \ 0]$ and $\boldsymbol{E} = [0 \ 0 \ E_z]$ respectively.

Insertion of the TM^z polarized field vectors into (2.9c,2.9d) leads to the governing equations of this simplified model, written as

$$\frac{\partial H_x}{\partial t} = -\frac{\partial E_z}{\partial y} \tag{2.10a}$$

$$\frac{\partial H_y}{\partial t} = \frac{\partial E_z}{\partial x} \tag{2.10b}$$

$$\frac{\partial E_z}{\partial t} = \frac{\partial H_y}{\partial x} - \frac{\partial H_x}{\partial y} \tag{2.10c}$$

2.3.2 TE^z Polarization

In a similar manner, the transverse electric polarization to the z-axis (TE^z) assumes that only the electric oscillations occur in the x-y plane and that, as a result, the magnetic field can only appear in the z-axis. Consequently, in this case, the field vectors are expressed as $\boldsymbol{E} = [E_x \ E_y \ 0]$ and $\boldsymbol{H} = [0 \ 0 \ H_z]$ and following insertion into (2.9c,2.9d) we obtain the governing equations for this polarization as

$$\frac{\partial E_x}{\partial t} = \frac{\partial H_z}{\partial y} \tag{2.11a}$$

$$\frac{\partial E_y}{\partial t} = -\frac{\partial H_z}{\partial x} \tag{2.11b}$$

$$\frac{\partial H_z}{\partial t} = -\left(\frac{\partial E_y}{\partial x} - \frac{\partial E_x}{\partial y}\right) \tag{2.11c}$$

2.4 Linearity of the Equations

Note, due to the linearity of the equations, that the variables of the equations presented in Sections 2.2 and 2.3 can be separated into their incident and scattered components. For example, the total field solution can be expressed generally in terms of its components as

$$\phi = \phi^i + \phi^s \tag{2.12}$$

where ϕ, ϕ^i and ϕ^s denote the total, incident and scattered fields respectively. This is an extremely useful property of the equations, which means that solutions can be sought solely in terms of the scattered field. Subsequently, where the total wave field is required, the incident wave component can be incorporated by simple summation to the scattered field.

This property will be used throughout the work and we will focus, particularly in the numerical approximation stage, on the evaluation of the scattered field component. Consequently, the analytical solutions obtained in the next section will be in terms of the scattered component. Furthermore, it will be seen that the component nature of the wave field will be relied upon within the derivation procedure to obtain the final analytical expressions.

2.5 Analytical Solutions

The derivation of an analytical solution for wave scattering from a two dimensional circular scatterer follows that described in Balanis [35]. In [35], the solutions for EM wave scattering from a perfect electrical conductor (PEC), in both transverse electric (TE^z) and transverse magnetic (TM^z) polarizations, are given using a three dimensional representation of an infinite circular cylinder. Subsequently, in this thesis, the correspondence of these EM models to hard and soft acoustic scattering problems will be demonstrated.

2.5.1 Prerequisites: Bessel and Hankel Functions and Cylindrical Wave Transformations

Before the derivation of analytical solutions is attempted for the various wave scattering models under consideration, we must first familiarize ourselves with some useful and necessary functions and transformations. A summary of these concepts is included in [35], with a much broader discussion for the interested reader to be found in [36].

Bessel Functions

In general, the most important and common Bessel functions are defined as solutions to Bessel's differential equation when expressed in the form

$$x^2\frac{d^2Z_n}{dx^2}+x\frac{dZ_n}{dx}+(x^2-n^2)=0 \tag{2.13}$$

where n is an integer. As this is a second order differential equation it must be satisfied by two linearly independent solutions, thus giving the two main classes of Bessel functions. The first independent solution, namely Bessel functions of the first kind, can be expressed as

$$J_n(x)=\sum_{m=0}^{\infty}\frac{(-1)^m}{m!(m+n)!}\left(\frac{x}{2}\right)^{2m+n} \tag{2.14a}$$

and

$$J_{-n}(x)=\sum_{m=0}^{\infty}\frac{(-1)^m}{m!(m-n)!}\left(\frac{x}{2}\right)^{2m-n} \tag{2.14b}$$

whereas, the second linearly independent solution, Bessel functions of the second kind, are given by

$$Y_n(x)=\frac{J_n(x)\cos(n\pi)-J_{-n}(x)}{\sin(n\pi)} \tag{2.15}$$

Hankel Functions

Hankel functions of the first and second kinds, sometimes referred to as Bessel functions of the third kind, are a linear combination of the first and second Bessel functions, and are themselves linearly independent solutions of Bessel's differential equation. These functions can be expressed respectively as

$$H_n^{(1)}(x)=J_n(x)+\mathrm{i}Y_n(x) \tag{2.16a}$$

and

$$H_n^{(2)}(x) = J_n(x) - \mathrm{i}Y_n(x) \tag{2.16b}$$

where $\mathrm{i} = \sqrt{-1}$ is the imaginary unit, and are commonly used to express outward or inward propagating cylindrical waves.

Recurrence Relation

Additionally, an alternative definition of Bessel functions, which can also aid the computation of these functions, is that they must satisfy the recurrence relations

$$Z_{n+1} + Z_{n-1} = \frac{2n}{x} Z_n \tag{2.17a}$$

and

$$Z_{n+1} - Z_{n-1} = -2\frac{dZ_n}{dx} \tag{2.17b}$$

Note that these relations hold for all of the various types of Bessel functions introduced above.

Cylindrical Wave Transform

Finally, the cylindrical wave transformation

$$e^{-ikx} = e^{-ikrcos\phi} = \sum_{n=-\infty}^{+\infty} i^{-n} J_n(kr) e^{in\phi} \tag{2.18}$$

will also be required to enable the plane incident wave to be expressed in a similar infinite series form as will be proposed for the scattered field.

2.5.2 Solution Procedure

The analytical solution will be obtained for the case of a plane wave striking a circular cylindrical scatterer of infinite length at normal incidence. Therefore, assuming a Cartesian coordinate system, where the infinite z dimension can be considered to lie perpendicular to the plane of the page, the incident field will be defined to propagate in a positive direction parallel to the x axis. Within this field, a circular cylinder of diameter a is placed with its centre at the origin, as shown on Fig 2.1.

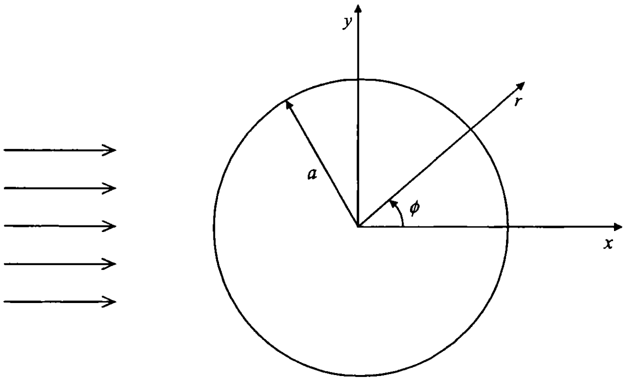

Figure 2.1: Circular cylindrical scatterer geometry

2.5.3 TM^z Polarization

For a transverse magnetic (TM^z) polarization, where the magnetic field oscillations are defined to occur solely in the x-y plane and to which the electric field oscillations must be orthogonal, we can write

$$\boldsymbol{E} = [0\ 0\ E_z]^T$$

For an incident plane TM^z wave, the non-zero component of this electric field can be expressed as

$$E_z^i = E_0 e^{-ik_x x}$$

and, when transformed into cylindrical polar coordinates, this becomes

$$E_z^i = E_0 e^{-ik_x r cos\phi}$$

Using the cylindrical wave transformation of equation (2.18), this can be expressed as

$$E_z^i = E_0 \sum_{n=-\infty}^{+\infty} i^{-n} J_n(k_x r) e^{in\phi} \tag{2.19}$$

Now considering the scattered field E_z^s, we require a representation which can model its outward propagation by utilizing cylindrical travelling wave functions. Therefore, as suggested in [35], using the cylindrical travelling wave form of the Hankel function

(2.16b), we define a solution of the form

$$E_z^s = E_0 \sum_{n=-\infty}^{+\infty} c_n H_n^{(2)}(k_x r) \tag{2.20}$$

where c_n represents the amplitude coefficients.

Having obtained expressions for both the incident and scattered components of the electric wave field, the total field can now be simply expressed by the summation of these terms as

$$E_z = E_z^i + E_z^s = E_0 \sum_{n=-\infty}^{+\infty} [i^{-n} J_n(k_x r) e^{in\phi} + c_n H_n^{(2)}(k_x r)] \tag{2.21}$$

Subsequently, application of the boundary condition for a perfect electrical conductor (PEC) surface, $\boldsymbol{E} \times \boldsymbol{n}|_{\Gamma_{PEC}} = \mathbf{0}$, which for a TM^z polarization reduces to $E_z = 0$, can be used to compute the amplitude coefficients c_n. Therefore, expressing the total electric field at $r = a$ using (2.21), gives

$$E_z|_{r=a} = E_0 \sum_{n=-\infty}^{+\infty} [i^{-n} J_n(k_x a) e^{in\phi} + c_n H_n^{(2)}(k_x a)] = 0$$

and following simple manipulation we obtain

$$c_n = -i^{-n} \frac{J_n(k_x a)}{H_n^{(2)}(k_x a)} e^{in\phi} \tag{2.22}$$

Therefore, upon substitution of (2.22) into the expression for the scattered field, equation (2.20) becomes

$$E_z^s = E_0 \sum_{n=-\infty}^{+\infty} -i^{-n} \frac{J_n(k_x a)}{H_n^{(2)}(k_x a)} H_n^{(2)}(k_x r) e^{in\phi} \tag{2.23}$$

which ultimately, utilising the odd and even symmetries of sine and cosine functions respectively, can be reduced to

$$E_z^s = E_0 \sum_{n=0}^{+\infty} -i^{-n} \varepsilon_n \frac{J_n(k_x a)}{H_n^{(2)}(k_x a)} H_n^{(2)}(k_x r) \cos(n\phi) \tag{2.24}$$

where

$$\varepsilon_n = \begin{cases} 1 & \text{for } n = 0 \\ 2 & \text{for } n \neq 0 \end{cases} \tag{2.25}$$

2.5.4 TE^z Polarization

The derivation procedure for a TE^z polarization follows a similar method to that contained in the previous sub-section. Beginning with the definition of the magnetic field,

$$\boldsymbol{H} = [0\,0\,H_z]^T$$

we can express the non-zero component for an incident plane wave as

$$H_z^i = H_0 e^{-ik_x x} = H_0 e^{-ik_x r cos\phi}$$

and, once again, application of the cylindrical wave transformation enables us to express this as the summation

$$H_z^i = H_0 \sum_{n=-\infty}^{+\infty} i^{-n} J_n(k_x r) e^{in\phi} \tag{2.26}$$

Seeking, as before, a distribution that will facilitate the representation of outward propagating cylindrical waves, we define the scattered field to be

$$H_z^s = H_0 \sum_{n=-\infty}^{+\infty} d_n H_n^{(2)}(k_x r) \tag{2.27}$$

where d_n represents the amplitude coefficients. To evaluate these coefficients, we will once again apply the boundary condition, $\boldsymbol{E} \times \boldsymbol{n}|_{\Gamma_{PEC}} = 0$, of zero tangential electric field on the surface of the scatterer. However, before this is possible, we must first obtain expressions for the corresponding electric fields E_r and E_ϕ for both the incident and scattered fields. Using Maxwell's Ampere equation (2.9d) in harmonic form

$$\boldsymbol{E} = \frac{1}{i\omega\varepsilon} \nabla \times \boldsymbol{H} \tag{2.28}$$

insertion of the incident magnetic field (2.26) gives

$$E_r^i = \frac{1}{i\omega\varepsilon} \frac{1}{r} \frac{\partial H_z^i}{\partial \phi} = \frac{H_0}{i\omega\varepsilon} \frac{1}{r} \sum_{n=-\infty}^{+\infty} n i^{-n+1} J_n(k_x r) e^{in\phi} \tag{2.29a}$$

$$E_\phi^i = -\frac{1}{i\omega\varepsilon} \frac{\partial H_z^i}{\partial r} = \frac{k_x H_0}{i\omega\varepsilon} \sum_{n=-\infty}^{+\infty} i^{-n} J_n'(k_x r) e^{in\phi} \tag{2.29b}$$

whereas insertion of the scattered magnetic field (2.27) leads to

$$E_r^s = \frac{1}{i\omega\varepsilon}\frac{1}{r}\frac{\partial H_z^s}{\partial\phi} = \frac{H_0}{i\omega\varepsilon}\frac{1}{r}\sum_{n=-\infty}^{+\infty} H_n^{(2)}(k_x r)\frac{\partial d_n}{\partial\phi} \tag{2.30a}$$

$$E_\phi^s = -\frac{1}{i\omega\varepsilon}\frac{\partial H_z^s}{\partial r} = \frac{k_x H_0}{i\omega\varepsilon}\sum_{n=-\infty}^{+\infty} d_n H_n^{(2)\prime}(k_x r) \tag{2.30b}$$

Note that the prime $'$ indicates a partial derivative with respect to the entire argument of the Hankel function. Having obtained both incident and scattered distributions, we can now form the total wave field for the tangential electric field, thus enabling the application of the PEC boundary condition, giving

$$E_\phi^t|_{r=a} = -\frac{k_x H_0}{i\omega\varepsilon}\sum_{n=-\infty}^{+\infty}[i^{-n}J_n'(k_x a)e^{in\phi} + d_n H_n^{(2)\prime}(k_x a)] = 0$$

Subsequent manipulation gives

$$d_n = -i^{-n}\frac{J_n'(k_x a)}{H_n^{(2)\prime}(k_x a)}e^{in\phi} \tag{2.31}$$

which upon insertion into (2.27) leads ultimately to

$$H_z^s = -H_0\sum_{n=0}^{+\infty} i^{-n}\varepsilon_n\frac{J_n'(k_x a)}{H_n^{(2)\prime}(k_x a)}H_n^{(2)}(k_x r)\cos(n\phi) \tag{2.32}$$

noting that the odd and even symmetries of sines and cosines have been applied and that ε_n is as defined in (2.25).

2.5.5 Analogous Acoustic Models

The previous derivations of analytical solutions for wave scattering problems were performed following an existing methodology described in [35] for electromagnetic models. Therefore, it is now of importance to demonstrate how these models correspond to problems defined in the field of acoustics. Not only will this be done by comparison of the governing equations, but also by comparison of the appropriate boundary conditions applicable to the scatterer in each case, which will be shown to require some care due to the subtle difference in variable transformation between the models.

Therefore, at this stage, it would be useful if we remind ourselves of the governing equations for each of these models. As derived in Section 2.2.1, the governing equations, in simultaneous equation form, for scalar acoustic waves in two space dimensions (2.5) are

$$\frac{\partial u}{\partial t} = -\frac{\partial p}{\partial x} \tag{2.33a}$$

$$\frac{\partial v}{\partial t} = -\frac{\partial p}{\partial y} \tag{2.33b}$$

$$\frac{\partial p}{\partial t} = -\left(\frac{\partial u}{\partial x} + \frac{\partial v}{\partial y}\right) \tag{2.33c}$$

Note again, that the isentropic flow condition (2.4) has been applied here to express all equations in terms of pressure, that the wave speed c_0 and time-averaged density ρ_0 have been assumed as unit valued for simplicity and that the equations in this system have been reordered to facilitate comparison with the electromagnetic equations. The TM^z polarization (2.10) gives

$$\frac{\partial H_x}{\partial t} = -\frac{\partial E_z}{\partial y} \tag{2.34a}$$

$$\frac{\partial H_y}{\partial t} = \frac{\partial E_z}{\partial x} \tag{2.34b}$$

$$\frac{\partial E_z}{\partial t} = \frac{\partial H_y}{\partial x} - \frac{\partial H_x}{\partial y} \tag{2.34c}$$

and for the TE^z polarization (2.11), we obtain

$$\frac{\partial E_x}{\partial t} = \frac{\partial H_z}{\partial y} \tag{2.35a}$$

$$\frac{\partial E_y}{\partial t} = -\frac{\partial H_z}{\partial x} \tag{2.35b}$$

$$\frac{\partial H_z}{\partial t} = -\left(\frac{\partial E_y}{\partial x} - \frac{\partial E_x}{\partial y}\right) \tag{2.35c}$$

Note also that the boundary conditions for a perfect electrical conductor (PEC) placed in an electromagnetic field are

$$\boldsymbol{E} \times \boldsymbol{n}|_{\Gamma_{PEC}} = 0 \tag{2.36a}$$

$$\boldsymbol{H} \cdot \boldsymbol{n}|_{\Gamma_{PEC}} = 0 \tag{2.36b}$$

As a point of interest, these are not independent conditions, as one can be derived quite simply from the other.

Soft Acoustic Scatterer $\Leftrightarrow$ PEC Scatterer in TM^z Polarization

By comparison of the acoustic equations (2.33) and the TM^z polarization (2.34) we can see that the transformation of variables required to obtain one set of equations from the other is given by

$$u \Leftrightarrow -H_y \quad v \Leftrightarrow H_x \quad p \Leftrightarrow E_z \tag{2.37}$$

The PEC boundary condition (2.36a) on the tangential electric field for the TM^z polarization

$$\boldsymbol{E} \times \boldsymbol{n}|_{\Gamma_{PEC}} = [-E_z n_y \; E_z n_x \; 0] = \mathbf{0}$$

reduces to $E_z|_{\Gamma_{PEC}} = 0$, as it must hold for any surface normal direction n_x, n_y. Reference to the transformations (2.37) shows that this is simply analogous to a zero surface pressure $p|_{\Gamma_{soft}}$, which is the scattering boundary condition for an acoustic model of a soft scatterer.

Considering now the alternative boundary condition on the normal magnetic field intensity, which for a TM^z polarization is

$$\boldsymbol{H} \cdot \boldsymbol{n}|_{\Gamma_{PEC}} = H_x n_x + H_y n_y = 0$$

insertion of the appropriate transformation (2.37) leads, for the acoustic model, to

$$v n_x - u n_y = 0$$

This simplifies to the condition

$$\boldsymbol{v} \times \boldsymbol{n}|_{\Gamma_{soft}} = 0$$

which implies that the tangential component of the velocity must be zero.

Hard Acoustic Scatterer $\Leftrightarrow$ PEC Scatterer in TE^z Polarization

In a similar manner, comparison of the acoustic equations (2.33) with the TE^z polarization (2.35) shows that the necessary transformation is

$$u \Leftrightarrow E_y \quad v \Leftrightarrow -E_x \quad p \Leftrightarrow H_z \tag{2.38}$$

In this case, for the TE^z polarization, the PEC boundary condition on the tangential electric field (2.36a) is given by

$$\boldsymbol{E} \times \boldsymbol{n}|_{\Gamma_{PEC}} = [0\ 0\ E_x n_y - E_y n_x] = \boldsymbol{0} \tag{2.39}$$

Insertion of the transformations (2.38) in the third component of this vector leads to

$$-v n_y - u n_x = 0$$

which can be expressed concisely as

$$\boldsymbol{v} \cdot \boldsymbol{n}|_{\Gamma_{hard}} = 0$$

implying that the normal component of the velocity must be zero, as required on a hard acoustic surface.

The alternative magnetic field boundary condition for the TE^z formulation

$$\boldsymbol{H} \cdot \boldsymbol{n}|_{\Gamma_{PEC}} = [0\ 0\ H_z] \cdot [n_x\ n_y\ 0] = 0$$

is obviously satisfied by any H_z, meaning that no condition exists on the magnetic field intensity on the surface of the PEC scatterer. However, if we take the temporal derivative of the third vector component of (2.39)

$$\frac{\partial}{\partial t}(E_x n_y - E_y n_x) = n_y \frac{\partial E_x}{\partial t} - n_x \frac{\partial E_y}{\partial t}$$

and use the governing equations of the TE^z polarization to express this in terms of the magnetic field, we obtain

$$\frac{\partial}{\partial t}(E_x n_y - E_y n_x) = n_y \frac{\partial H_z}{\partial y} + n_x \frac{\partial H_z}{\partial x} = \frac{\partial H_z}{\partial n}$$

Now, as the PEC boundary condition on the tangential electric field must hold for all time, this gives the condition $(\partial H_z/\partial n)|_{\Gamma_{PEC}} = 0$ so that the normal gradient of the z component of the magnetic field must be zero. In turn, by transformation to the acoustic model, we find that the alternative condition on the hard scatterer is given by $(\partial p/\partial n)|_{\Gamma_{hard}} = 0$, which means the gradient of the pressure in the surface normal direction must be zero, as confirmed in [37].

2.6 Radar Cross Section

For practical applications, particularly in the electromagnetics field, an important measure of scattering is the radar cross section (RCS) [38]. Balanis [35] defines this as the area intercepting the amount of power that, when scattered isotropically, produces at the receiver a density that is equal to the density scattered by the actual target. In strict terms, this quantity refers solely to an output derived from a three dimensional wave scattering analysis. Therefore, for this work, where we concentrate on a two dimensional approximation, the analogous measure is termed the scattering width, which in effect is the radar cross section per unit length.

The method of computation for the scattering width follows that given in [39] and is explained below. Subsequently, expressions for the analytical distributions for a circular scatterer are presented [35].

2.6.1 Derivation

Firstly, the theoretical expressions for the scattering width generated in two dimensional problems can be written as

$$\chi(\phi) = \lim_{r \to \infty} 2\pi r \frac{|H_z^s|^2}{|H_z^i|^2} \tag{2.40}$$

and

$$\chi(\phi) = \lim_{r \to \infty} 2\pi r \frac{|E_z^s|^2}{|E_z^i|^2} \tag{2.41}$$

for a TE^z and TM^z polarization of the EM fields respectively, where (r, ϕ) are cylindrical polar coordinates. As these expressions involve values where the radial distance from the scatterer approaches infinity, a near to far field transformation is required. This is achieved by considering an arbitrary surface *S*, which completely encloses the scatterer, and applying the surface equivalence theorem [35]. The scattered fields, $\boldsymbol{E}^s$ and $\boldsymbol{H}^s$, on this surface *S* are then taken from the approximate solution to compute equivalent surface electric and magnetic currents, $\boldsymbol{J}^s$ and $\boldsymbol{M}^s$, as

$$\boldsymbol{J}^s = \boldsymbol{n} \times \boldsymbol{H}^s \tag{2.42a}$$

$$\boldsymbol{M}^s = -\boldsymbol{n} \times \boldsymbol{E}^s \tag{2.42b}$$

where $\boldsymbol{n}$ is defined as the outward normal to the surface *S*. The vector potentials, $\boldsymbol{A}^s$ and $\boldsymbol{F}^s$, at any point beyond this surface *S* can now be evaluated with the vector expression

$$\begin{bmatrix} \boldsymbol{A}^s \\ \boldsymbol{F}^s \end{bmatrix} = \frac{1}{4\mathrm{i}} \int_S \begin{bmatrix} \boldsymbol{J}^s(x', y') \\ \boldsymbol{M}^s(x', y') \end{bmatrix} H_0^{(2)}(kR)\, dx'dy' \tag{2.43}$$

The Hankel function of the second kind $H_0^{(2)}$ present in this expression can be approximated by the asymptotic relation

$$H_0^{(2)}(\zeta) \approx \sqrt{\frac{2\mathrm{i}}{\pi\zeta}}\, e^{-\mathrm{i}\zeta} \tag{2.44}$$

as $\zeta \longrightarrow \infty$. This gives the required far field values of the vector potentials, $\boldsymbol{A}^s$ and $\boldsymbol{F}^s$. Ultimately, the corresponding scattered field variables, $\boldsymbol{E}^s$ and $\boldsymbol{H}^s$, can then be obtained and upon substitution into (2.40) and (2.41) enable the expressions for the scattering width to be written as

$$\chi(\phi) = \frac{k}{4}\Bigg[\int_S \{n_y H_z^s \sin\phi + n_x H_z^s \cos\phi + n_y E_x^s - n_x E_y^s\} \\ e^{\mathrm{i}k(x'\cos\phi + y'\sin\phi)}\, dx'dy'\Bigg]^2 \tag{2.45}$$

for the TE^z polarization and

$$\chi(\phi) = \frac{k}{4}\left[\int_S \{-n_y E_z^s \sin\phi - n_x E_z^s \cos\phi + n_x H_y^s - n_y H_x^s\} \, e^{ik(x'\cos\phi + y'\sin\phi)}\, dx'dy'\right]^2 \tag{2.46}$$

for the TM^z polarization respectively. Note that the surface S, used to record the near field data and subsequently used in the transformation to the far field, will be taken at the surface of the scatterer in this work, unless otherwise noted.

Finally, in practice, the scattering width is measured in decibels. Therefore, a logarithm of the quantity will be used of the form

$$Scattering\ width = 10\log_{10}\chi(\phi) \tag{2.47}$$

This will be the quantity displayed in the forthcoming analyses.

2.6.2 Analytical Solution

From [35], the exact expression for the scattering width for a PEC cylinder in a TE^z polarized electromagnetic model can be written as

$$\chi(\phi) = \frac{4}{k_x}\left|\sum_{n=0}^{\infty} \varepsilon_i \frac{J_n'(k_x a)}{H_n^{(2)\prime}(k_x a)} \cos n\phi\right|^2 \tag{2.48}$$

Similarly, for a TM^z model of a PEC cylinder, the scattering width is expressed as

$$\chi(\phi) = \frac{4}{k_x}\left|\sum_{n=0}^{\infty} \varepsilon_i \frac{J_n(k_x a)}{H_n^{(2)}(k_x a)} \cos n\phi\right|^2 \tag{2.49}$$

In both of these expressions, ε is defined as in (2.25) and the infinite series can be truncated when the remaining terms become negligible.

With these exact expressions for the example of wave scattering from a circular cylinder, we now have a means by which to compare the approximate scattering widths generated by the proposed computational procedure. Consequently, in conjunction with the analytical wave scattering solution derived in Section 2.5, an appropriate method of validation is available.

2.7 Finite Element Method

As the work in this thesis is based mainly on the application of finite element solution procedures [7], a brief introduction and description of the basic method will be given to complete the chapter.

First encountered in the 1950s in the field of aero-elasticity, the finite element method was soon extended to the more general applications of continuum mechanics and fluid mechanics. Today, finite elements enjoy widespread application with numerous commercial computer codes utilising the technique.

2.7.1 Weak Formulation of the Governing Equations

In general, once the mathematical model of the physical problem has been established, which in the physical and engineering sciences most frequently results in a system of differential equations, this set of governing equations is recast in an alternative weak form. This is achieved by expressing a weighted residual of the strong form, the original differential equations, which is computed as an integral over the specified problem domain Ω.

Limiting our attention to a linear system, which is sufficient for the requirements of this work, the problem can be stated generally as [7]

$$\mathsf{A}(\boldsymbol{U}) = \mathsf{L}\boldsymbol{U} + \boldsymbol{p} = 0 \qquad in\,\Omega \tag{2.50a}$$

$$\mathsf{B}(\boldsymbol{U}) = \mathsf{M}\boldsymbol{U} + \boldsymbol{r} = 0 \qquad on\,\Gamma \tag{2.50b}$$

where L and M are linear differential operators, $\boldsymbol{p}$ and $\boldsymbol{r}$ are independent of the unknown vector $\boldsymbol{U}$, Ω is the domain over which this problem definition holds and this is bounded by the surface Γ. There are two main types of boundary conditions which can be applied through the boundary differential equation (2.50b), namely Dirichlet and Neumann conditions. For Dirichlet conditions, the values of the unknown $\boldsymbol{U}$ are specified on the domain boundary and can be applied as

$$\boldsymbol{U} = \bar{\boldsymbol{U}} \qquad on\,\Gamma_D \tag{2.51}$$

where $\mathsf{M}U = \boldsymbol{U}$, $\boldsymbol{r} = -\bar{\boldsymbol{U}}$ and $\bar{\boldsymbol{U}}$ is known. For Neumann conditions, the flux of the unknown normal to the boundary Γ_N is specified and can be expressed as

$$k\frac{\partial \boldsymbol{U}}{\partial \boldsymbol{n}} = -\bar{\boldsymbol{q}} \qquad on\ \Gamma_N \tag{2.52}$$

where $\mathsf{M}U = -k\partial \boldsymbol{U}/\partial \boldsymbol{n}$, $\boldsymbol{r} = -\bar{q}$ and $\bar{\boldsymbol{q}}$ is a known flux, k is a constant and $\boldsymbol{n}$ is the outward normal to the boundary.

Subsequently, the formulation of a weak statement of the problem is given by the combined weighted residual of (2.50a) and (2.50b), which can be written as

$$\int_\Omega \boldsymbol{W}\mathsf{A}(\boldsymbol{U})\, d\Omega + \int_\Gamma \bar{\boldsymbol{W}}\mathsf{B}(\boldsymbol{U})\, d\Gamma = 0 \tag{2.53}$$

where $\boldsymbol{W}$ and $\bar{\boldsymbol{W}}$ are vectors of arbitrary weighting functions. Here, no strict condition on the approximation, such as the requirement that the approximation must satisfy some, or all, of the problem boundary conditions, has been imposed. Therefore, the formal definition of the appropriate mathematical space from which the solution is sought can be stated quite generally as

$$\boldsymbol{\Phi} = \{\boldsymbol{U} \in H^1(\Omega)\} \tag{2.54}$$

where H represents the Hilbert space.

Various choices can be made regarding the weighting functions to be applied. For the commonly used Bubnov-Galerkin finite element approximation, which will be the form used throughout this thesis, the space of the weighting functions is taken to be equal to that of the unknown variable, giving

$$\boldsymbol{\Psi} = \{\boldsymbol{W} \in H^1(\Omega)\} \tag{2.55}$$

Alternatively, by constraining the approximation to functions which must satisfy the problem boundary conditions, the weighted residual (2.53) reduces to

$$\int_\Omega \boldsymbol{W}\mathsf{A}(\boldsymbol{U})\, d\Omega = 0 \tag{2.56}$$

as the weighted residual on the boundary Γ must be identically zero. However, the solution and weighting function space must be reduced correspondingly to ensure that this constraint is enforced, giving respectively

$$\boldsymbol{\Phi} = \{\boldsymbol{U} \in H^1(\Omega) \; : \; \boldsymbol{U} = \bar{\boldsymbol{U}} \; on \; \Gamma_D \; , \; k\frac{\partial \boldsymbol{U}}{\partial \boldsymbol{n}} = -\bar{\boldsymbol{q}} \; on \; \Gamma_N\} \tag{2.57}$$

$$\boldsymbol{\Psi} = \{\boldsymbol{W} \in H^1(\Omega) \; : \; \boldsymbol{W} = 0 \; on \; \Gamma\} \tag{2.58}$$

Returning to the full weighted residual form (2.53), this, if desired, can be manipulated into another form, which may be beneficial for two reasons. Firstly, the manipulation can reduce the order of the differentiation involved, which may be useful to ease the inter-element continuity requirements imposed on the interpolation functions. Secondly, where appropriate gradient boundary conditions are applied, commonly referred to as natural boundary conditions, it may result in a simplified formulation. Further advantage of this formulation can be achieved by specifying solution and weighting function spaces which fall between those previously defined. In this case, the solution space can be constrained for only the Dirichlet boundary conditions, thus leaving the Neumann conditions as degrees of freedom to be satisfied by the approximation. Therefore, the solution and weighting function spaces can be defined respectively as

$$\boldsymbol{\Phi} = \{\boldsymbol{U} \in H^1(\Omega) \; : \; \boldsymbol{U} = \bar{\boldsymbol{U}} \; on \; \Gamma_D\} \tag{2.59}$$

$$\boldsymbol{\Psi} = \{\boldsymbol{W} \in H^1(\Omega) \; : \; \boldsymbol{W} = 0 \; on \; \Gamma_D\} \tag{2.60}$$

The application of integration-by-parts and Green's lemma to (2.53), leads to the addition of a further surface integral term to the weighted residual statement

$$\int_\Omega \mathsf{C}(\boldsymbol{W})\mathsf{D}(\boldsymbol{U}) \, d\Omega - \int_\Gamma \boldsymbol{W}\mathsf{E}(\boldsymbol{U}) \, d\Gamma + \int_{\Gamma_N} \bar{\boldsymbol{W}}\mathsf{B}(\boldsymbol{U}) \, d\Gamma = 0 \tag{2.61}$$

where C, D and E are all linear differential operators of lower order than the initial operator A. In some cases, the differential terms of the linear operators B and E will be identical. Consequently, by defining a suitable relationship between the weighting functions $\boldsymbol{W}$ and $\bar{\boldsymbol{W}}$ on Γ_N, some of the boundary terms will be negated leading to a simplified form

$$\int_\Omega \mathsf{C}(\boldsymbol{W})\mathsf{D}(\boldsymbol{U}) \, d\Omega + \int_{\Gamma_N} \boldsymbol{W}\boldsymbol{r} \, d\Gamma = 0 \tag{2.62}$$

where the remaining boundary integral can be used to apply the known boundary condition. Note that the component of the additional boundary integral term taken over the Dirichlet boundary Γ_D will be identically zero, as the weighting function $\boldsymbol{W}$ on this boundary must be zero following the definition of the weighting function space (2.60).

2.7.2 Approximation Procedure

The finite element procedure can now be applied to obtain an approximate solution to this alternative formulation of the initial problem. This is achieved by introducing a finite dimensional mathematical space for the approximate solution, and thus the weighting function,

$$\boldsymbol{\Phi}_N = \{\boldsymbol{U}_N \,\epsilon\, H^1_N(\Omega) \;:\; \boldsymbol{U} = \bar{\boldsymbol{U}} \; on \, \Gamma_D\} \tag{2.63a}$$

$$\boldsymbol{\Psi}_N = \{\boldsymbol{W}_N \,\epsilon\, H^1_N(\Omega) \;:\; \boldsymbol{W} = 0 \; on \, \Gamma_D\} \tag{2.63b}$$

Subsequently, the weighted residual can be expressed as

$$\int_\Omega \mathsf{C}(\boldsymbol{W}_N)\mathsf{D}(\boldsymbol{U}_N)\, d\Omega + \int_\Gamma \boldsymbol{W}_N \boldsymbol{r}\, d\Gamma = 0 \tag{2.64}$$

To facilitate the solution of this statement, the computational domain is discretised into smaller non-overlapping elements. Interpolation functions N_I expressing the variation of the unknown $\boldsymbol{U}_N$ over individual elements are constructed, enabling the approximation

$$\boldsymbol{U}_N = \sum_{I=1}^{N} N_I \boldsymbol{U}_I \tag{2.65}$$

where the interpolation functions are defined to be non-zero only within those elements to which the global point I belongs.

For steady problems, this completes the approximation process and all that remains is to solve the resulting system of linear equations. However, for time dependent problems, as considered in this work, this process results in a semi-discrete equation set, where the spatial approximation is complete but the temporal approximation is yet to be applied. Due to their hyperbolic nature, these equations can be advanced using a time-stepping scheme, the choice of which is vast. However, the dangers of instability in the resulting numerical solutions necessitates great care in their selection. Therefore, the following discussion will explain further aspects of the discretisation procedure and specific difficulties which must be overcome, before culminating in the recommendation of a particular temporal scheme.

2.8 Solution Procedures for Convective Problems

To facilitate a discussion of the possible unstable numerical solutions produced by finite element spatial approximations of problems with a convective component, we will limit our consideration, in this section, to simpler scalar equations. Beginning with the general scalar convection diffusion equation

$$\frac{\partial \phi}{\partial t} + \frac{\partial F_i}{\partial x_i} = S_i \tag{2.66}$$

where ϕ is the unknown dependent variable, F_i is the flux and S_i represents any source terms. The flux F_i is given by

$$F_i = \left(u_i \phi - k \frac{\partial \phi}{\partial x_i} \right) \tag{2.67}$$

which shows clearly both the convective, $u_i\phi$, and diffusive, $-k\partial\phi/\partial x_i$, components of the problem.

Focusing on the intended spatial discretisation method, the standard Galerkin finite element procedure is known to give optimal energy norm solutions for symmetric or self-adjoint equations, where a corresponding variational statement can be shown to exist [7]. Hence, for the symmetric problems encountered in the solid mechanics field, for which the initial applications of the finite element method were used, the resulting solutions would be optimal. The same can also be taken to hold for diffusion dominated problems such as those for thermal conductivity and creeping Stokes flow where the convective component of the flow is less significant. In these cases, the numerical solution remains stable and the approximate solution will converge to an exact solution as the level of discretisation is increased.

However, in fields where convective flow becomes more prominent, the differential operators of the governing equations lose their symmetry and hence the standard Galerkin finite element discretisation ceases to be optimal. The resulting solutions display instabilities which become more apparent as the convective component of the flow increases [40]. In the extreme of convection problems, where the diffusive flow component is, or can be assumed, negligible, the governing equation for scalar transport can be seen from (2.66) and (2.67) to reduce to

$$\frac{\partial \phi}{\partial t} + \frac{\partial (u_i \phi)}{\partial x_i} = S_i \tag{2.68}$$

which is simply the scalar convection equation expressed in conservation form. This equation expresses the mechanism by which wave propagation occurs and thus offers a simplified model which can be used in this discussion. Note, for example, that it has already been shown that the governing equation for acoustic wave propagation can be written as a linear system of equations of this type (2.3).

For a flow whose convection velocity u_i is divergence free, implying incompressible flow, the identity

$$\frac{\partial (u_i \phi)}{\partial x_i} = \phi \frac{\partial u_i}{\partial x_i} + u_i \frac{\partial \phi}{\partial x_i} \tag{2.69}$$

can be used to simpilfy (2.68) to the non-conservation scalar convection equation

$$\frac{\partial \phi}{\partial t} + u_i \frac{\partial \phi}{\partial x_i} = 0 \tag{2.70}$$

where a zero source term S_i is also assumed.

Inevitably, the instability of these models leads to the requirement for some form of stabilisation to enable the exact solution to be approximated more appropriately. Consequently, in the following section, an appropriate stabilisation technique will be introduced.

2.9 Taylor Galerkin Schemes

As discussed above, due to the convective nature of wave propagation problems, the standard Galerkin spatial discretisation procedure gives rise to instabilities in the numerical solution. To overcome these undesirable effects, some form of stabilisation must be applied to the scheme.

One such discretisation method, which inherently applies stabilisation to a numerical model through the temporal approximation, is the Taylor Galerkin family of schemes [41]. These follow the basic theory of the well-known Lax-Wendroff schemes for finite difference (FD) approximations [42]. In Section 2.9.1 , the one-step second order Taylor Galerkin (TG2) temporal discretisation will be performed for the scalar convection equation. However, it should be noted that arbitrary orders of accuracy can be achieved by simply increasing the number of terms used in the expansion for the temporal approximation. In this way, third order Taylor Galerkin schemes will also be introduced.

2.9.1 Second Order Taylor Galerkin Scheme (TG2)

For the Taylor Galerkin family of schemes, numerical approximation of time-dependent governing equations begins with the temporal discretisation. A Taylor series expansion for the dependent variable ϕ at time $n+1$ can be expressed exactly in terms of the variables at time n as

$$\phi^{n+1} = \phi^n + \Delta t \left.\frac{\partial \phi}{\partial t}\right|^n + \frac{\Delta t^2}{2!}\left.\frac{\partial^2 \phi}{\partial t^2}\right|^n + \frac{\Delta t^3}{3!}\left.\frac{\partial^3 \phi}{\partial t^3}\right|^n + \frac{\Delta t^4}{4!}\left.\frac{\partial^4 \phi}{\partial t^4}\right|^n + O(\Delta t^5) \quad (2.71)$$

For the second order Taylor Galerkin (TG2) scheme, and as suggested above, we can now define the order of the scheme by truncating this expansion to include only second order derivatives or lower, giving the approximation

$$\Delta\phi = \Delta t \left.\frac{\partial \phi}{\partial t}\right|^n + \frac{\Delta t^2}{2!}\left.\frac{\partial^2 \phi}{\partial t^2}\right|^n + O(\Delta t^3) \quad (2.72)$$

where $\Delta\phi = \phi^{n+1} - \phi^n$. Analogously to the Lax-Wendroff scheme, the governing equations are now used to transform the temporal derivatives to spatial derivatives. Therefore, substituting (2.70) into the truncated Taylor series expansion (2.72) we obtain

$$\frac{\Delta\phi}{\Delta t} = -u_i \left.\frac{\partial \phi}{\partial x_i}\right|^n - \frac{\Delta t}{2}\frac{\partial}{\partial t}\left.\left(u_i \frac{\partial \phi}{\partial x_i}\right)\right|^n + O(\Delta t^2) \quad (2.73)$$

As can be seen, a temporal derivative is still present in the second order term. However, simple rearrangement of the derivatives enables us to rewrite this expression as

$$\frac{\Delta\phi}{\Delta t} = -u_i \left.\frac{\partial\phi}{\partial x_i}\right|^n - \frac{\Delta t}{2!} u_i \frac{\partial}{\partial x_i}\left.\left(\frac{\partial\phi}{\partial t}\right)\right|^n + O(\Delta t^2) \tag{2.74}$$

Thus, repeating the substitution of the governing equation (2.70) leads ultimately to

$$\frac{\Delta\phi}{\Delta t} = -u_i \left.\frac{\partial\phi}{\partial x_i}\right|^n + \frac{\Delta t}{2!} u_i^2 \left.\frac{\partial^2\phi}{\partial x_i^2}\right|^n + O(\Delta t^2) \tag{2.75}$$

which is the semi-discrete equation for the TG2 scheme.

Comparison of (2.75) with the initial governing equation (2.70) whose approximation is sought, shows clearly the mechanism by which the Taylor Galerkin schemes stabilise the numerical solution. The second order term, which was not apparent in (2.70), applies an artificial numerical diffusion to the scheme, thus helping to remove any spurious oscillations which may occur.

2.9.2 Third Order Taylor Galerkin Scheme (TG3)

Higher order temporal accuracy can be achieved by inclusion of a greater number of terms in the initial Taylor series expansion. Therefore, by using the first three derivative terms in equation (2.71)

$$\phi^{n+1} = \phi^n + \Delta t \left.\frac{\partial\phi}{\partial t}\right|^n + \frac{\Delta t^2}{2!} \left.\frac{\partial^2\phi}{\partial t^2}\right|^n + \frac{\Delta t^3}{3!} \left.\frac{\partial^3\phi}{\partial t^3}\right|^n + O(\Delta t^4) \tag{2.76}$$

we can obtain the semi discrete form for the third order Taylor Galerkin scheme, once again, by substituting the governing equation (2.70) to remove the remaining temporal derivatives. This gives the expression

$$\left[1 - \frac{\Delta t^2}{6}(u_i^2 \frac{\partial^2}{\partial x_i^2})\right] \Delta\phi = -\Delta t u_i \left.\frac{\partial\phi}{\partial x_i}\right|^n + \frac{\Delta t^2}{2!} u_i^2 \left.\frac{\partial^2\phi}{\partial x_i^2}\right|^n + O(\Delta t^3) \tag{2.77}$$

for a standard third order Taylor Galerkin approximation [41]. Examination of this expression reveals that, contrary to the TG2 scheme, the TG3 scheme would lead to an implicit solution procedure, regardless of the spatial discretisation method employed, due to the second order term apparent on the *LHS* of the equation.

2.9.3 Two-step Third Order Taylor Galerkin Scheme (TG3-2S)

The semi-discrete equation for the TG3 scheme (2.77) leads to the requirement for an implicit solution procedure. As expressed in Chapter 1, we require an explicit scheme to limit the computational expense of the method. Fortunately, an alternative form of the TG3 scheme exists which overcomes this problem [41]. The two-step third order Taylor Galerkin (TG3-2S) scheme is based on a formulation whereby a TG2-type approximation is repeated in two consecutive steps. Therefore, the temporal expansions for each step of this scheme are written as

$$\Delta\tilde{\phi} = \frac{1}{3}\Delta t\left.\frac{\partial\phi}{\partial t}\right|^n + \alpha\Delta t^2\left.\frac{\partial^2\phi}{\partial t^2}\right|^n \tag{2.78a}$$

$$\Delta\phi = \Delta t\left.\frac{\partial\phi}{\partial t}\right|^n + \frac{\Delta t^2}{2!}\left.\frac{\partial^2\tilde{\phi}}{\partial t^2}\right|^n \tag{2.78b}$$

where $\tilde{\phi}$ represents the approximate solution after the first partial step. Following the procedure explained above for the standard TG2 scheme, the temporal derivatives in these expressions can be removed to obtain the semi-discrete equations

$$\frac{\Delta\tilde{\phi}}{\Delta t} = -u_i\frac{1}{3}\left.\frac{\partial\phi}{\partial x_i}\right|^n + \alpha\Delta t u_i^2\left.\frac{\partial^2\phi}{\partial x_i^2}\right|^n \tag{2.79a}$$

$$\frac{\Delta\phi}{\Delta t} = -u_i\left.\frac{\partial\phi}{\partial x_i}\right|^n + \frac{\Delta t}{2!}u_i^2\left.\frac{\partial^2\tilde{\phi}}{\partial x_i^2}\right|^n \tag{2.79b}$$

where the parameter α can be optimised to reproduce exactly the phase-speed characteristics of the single-step TG3 scheme, using $\alpha = 1/9$ [41].

2.10 Conclusion

The first part of this chapter was dedicated to the presentation of the governing equations for wave propagation and scattering in the fields of acoustics and electromagnetics. Following the simplification of these equations, the correspondence between the equations for both fields was demonstrated. Subsequently, analytical equations for a simple wave scattering problem were derived. Further work in this thesis will involve the discretisation of the governing equations and the validation of the resulting numerical method by comparison with the analytical solutions.

In the second part of this chapter, the finite element discretisation procedure was introduced, including a discussion of the instabilities inherent in the solution of convective problems. Subsequently, the Taylor Galerkin family of stabilisation schemes was presented. However, the reader should be aware that there are many other viable stabilisation techniques which could also be used instead of the Taylor Galerkin schemes to remove instabilities from the finite element numerical solution, including the Petrov-Galerkin, Streamwise Upwind Petrov-Galerkin (SUPG) and Characteristic Galerkin schemes. However, as this work involves the approximation of smooth sinusoidal wave functions and is concerned mainly with the possible advantages of applying higher order elements, an indepth discussion of these various schemes is not included here. For further details, [40, 41] provide a good introduction and detail the advantages and disadvantages of these schemes. Various other schemes of temporal discretisation when applied with the finite element approximations can be found in [43].

Chapter 3

Spectral Element Method

3.1 Introduction

Generally, to improve the accuracy of a particular computational solution procedure, there are two main options: increase the refinement of the mesh by reducing the characteristic nodal spacing or element size, or increase the approximation order of the method, which in finite element terms, relates to the order of the interpolation functions. In this thesis, we intend to investigate the latter and hope to demonstrate that the theoretical computational advantages of such a strategy can be shown to extend to practical wave scattering problems.

In this section, we will discuss the application of a spectral element method (SEM) to the solution of wave propagation and scattering problems. Due to the higher level of computational expense usually inherent in such models, we focus our attention on a diagonal mass matrix solution method, the advantage of such a formulation being made clear in the following discussion.

Looking ahead at the complexity of scattering geometries intended for analysis with this method, the necessity for accurate geometrical representation is also considered. Combined with the previous desire for computational efficiency and the vast areas of open space usually encountered in scattering models, this leads naturally to a hybrid mesh formulation.

Consequently, the ensuing initial development of a computational method for wave scattering will be governed by the factors introduced here, thus offering justification and transparency in the formulation of the scheme.

3.1.1 Hybrid Mesh

As mentioned above, we aim to develop an efficient computational procedure with the capabilities to model complex scattering problems, which usually involve intricate scattering geometries. These are two conflicting requirements. However, considering the two aspects separately will hopefully provide a solution.

To enable accurate geometrical representation in a two-dimensional model, an unstructured mesh of triangular elements is generally accepted to be the most prudent method of discretisation. Due to the ease with which they tesselate, complex geometries can be approximated far more efficiently than with a structured mesh of quadrilateral elements, thus facilitating improved solution accuracy.

On the other hand, wave scattering models normally comprise of vast regions of open space, through which, having struck the scattering object, the waves propagate. Structured grids of quadrilateral elements discretise extensive areas, such as this, in a much more efficient manner than their unstructured counterparts.

This leads naturally to the use of a hybrid mesh. In the vicinity of the scatterer, an unstructured triangular mesh will be used, while beyond this, in more open areas, the domain will consist of a structured quadrilateral mesh.

3.1.2 Diagonalising the Mass Matrix

As will be seen in the derivation of the discretised form of our governing equations, the finite element numerical solution of a temporally varying problem normally introduces a mass matrix M in the formulation of the time-dependent term. This effectively creates a coupled system of equations

$$M\Delta \boldsymbol{U} = \Delta t \boldsymbol{R} \tag{3.1}$$

where $\boldsymbol{U}$ is the unknown vector and $\boldsymbol{R}$ is a typical right hand side vector representing the operators applied to the solution at the previous time-step. Therefore, the solution of an implicit system is required, irrespective of the choice of an explicit or implicit temporal scheme, which involves increased computational work to obtain the solution at each time-step. Here, the increased workload is inherent in the inversion of a global consistent mass matrix.

To decouple the equation system, thus enabling an explicit solution procedure, the mass matrix $\boldsymbol{M}$ must be diagonalised, or lumped, thus requiring only simple division to complete the matrix inversion. For linear elements, this is a trivial procedure, where the summation of each component on the same row of the matrix is placed on the diagonal entry and all other off-diagonal entries are taken as zero. Unfortunately, this lumping method is not directly applicable to higher order elements as negative or zero diagonal entries can result.

However, an alternative procedure exists for the construction of diagonal mass matrices. This method is dependent on the appropriate selection of interpolation functions and integration techniques, further details of which are given in the following section.

3.2 Interpolation Functions and Numerical Integration

The interpolation functions proposed for this method will be higher order polynomial functions defined using Lagrange interpolation through particular sets of points.

3.2.1 Interpolation Functions for Quadrilateral Elements

For quadrilateral elements, the interpolation functions N will be defined as a tensor product of two one-dimensional cardinal basis functions

$$N(x,y) = P(x) \otimes Q(y) \tag{3.2}$$

each constructed using Lagrange interpolation through Gauss-Legendre-Lobatto (GLL) points, a representation of which can be seen in Figure 3.1. This lays the foundation for an efficient time-domain solution method, as suggested in the previous section.

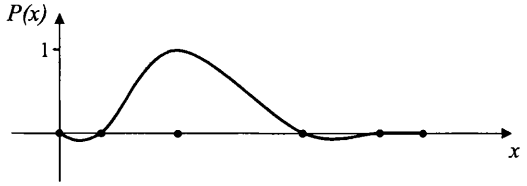

Figure 3.1: Representation of an interpolation function $P(x)$ for an interior node of a one dimenional element defined through GLL points

As will be seen, the standard form of the mass matrix $\boldsymbol{M}$ introduced in (3.1) can be expressed as

$$\boldsymbol{M} = \int_{\Omega} N_I N_J \, d\Omega \tag{3.3}$$

where integration of the interpolation functions can be carried out analytically, if possible, or by a suitable numerical quadrature. There are numerous numerical integration methods available, the most common of which is Gaussian quadrature. This method is optimised by evaluating all degrees of freedom, namely the quadrature points and weights, by enforcing the requirement that the approximation be exact for integration of polynomials of order $2n - 1$, where n is the number of quadrature points.

An alternative numerical integration method is GLL quadrature. In this case, optimisation is performed by evaluating all degrees of freedom except for two quadrature points, which are fixed at either end of the integration interval. This leads to a method which is slightly less accurate than Gaussian quadrature, being able to integrate exactly polynomials of order $2n - 3$. However, the positioning of the bounding quadrature points at the ends of the interval offers advantages in finite element formulations, as they can be positioned at the extents of the individual elements. Furthermore, the use of GLL points to define the interpolation functions means that the nodal points of each element coincide with the quadrature points of the numerical integration method. Consequently, due to the cardinal form of the interpolation functions, the use of GLL quadrature to evaluate the mass matrix $\boldsymbol{M}$ will always result in a diagonal matrix.

Therefore, inversion of the matrix to obtain the unknown increment ΔU in (3.1), can be achieved by trivial division of the equations in the system by the appropriate diagonal entry. Combined with an explicit temporal scheme, to take full advantage of this formulation, significant savings can be made in the computational expense needed to obtain the solution at the next time-step.

At this point, it should be noted from above, that the GLL points are defined for optimisation of the numerical quadrature, thus giving the closest approximation to polynomial integrals for the chosen initial constraint on the location of the boundary points. This will be referred to in the following subsection, when interpolation functions for triangular elements are considered.

3.2.2 Interpolation Functions for Triangular Elements

Unfortunately, standard two-dimensional tensor product formulations, as used for the quadrilateral elements, cannot be applied directly to triangular elements. Furthermore, a precise set of GLL points for a triangle is not known, meaning that an alternative set of points must be used. However, a similar procedure for the formulation of diagonal mass matrices can be applied to triangular elements. For these elements, the interpolation functions N will be defined directly by performing Lagrange interpolation through a two-dimensional set of Fekete points [20]. These points are defined in an attempt to optimise the approximation of a function, over the triangular element, in a similar manner to the points obtained using the lemma of Lebesgue, which can be expressed as

$$\|f - I_N(f)\| \leq (1 + \|I_N\|)\|f - h\| \tag{3.4}$$

In this expression, f is an arbitrary function, h is the best polynomial approximation to f of degree N or less and

$$\|I_N\| = \max_{\|f\|=1} \|I_N(f)\| \tag{3.5}$$

is the Lebesgue constant of degree N, which bounds the interpolation error in the max norm and, hence, is a measure of the accuracy of the interpolation. Sets of points with minimal Lebesgue constants are named Lebesgue points. However, there is very little known about these points in two or three spatial dimensions.

Fortunately, Fekete points provide a possible extension beyond one spatial dimension which have been shown numerically to be close to optimal [44]. The definition of these sets of points for a domain Ω begins with the selection of a polynomial basis $\{g_i, i = 1, N\}$. Subsequently, denoting a set of points within Ω as $\{z_i \in \Omega, i = 1, N\}$, the generalized Vandermonde matrix $\boldsymbol{V}$, of dimension $N \times N$, can be expressed in terms of its elements as $V_{ij} = g_j(z_i)$. Finally, the Fekete points are defined as the set $\{z_i \in \Omega, i = 1, N\}$ which maximise, for a fixed basis, the determinant of $\boldsymbol{V}$

$$\max_{\{z_i\}} |\boldsymbol{V}(z_1, z_2, ..., z_N)| \tag{3.6}$$

The application of a corresponding Fekete quadrature to the numerical approximation of the mass matrix integral $\boldsymbol{M}$ leads, once again, to a diagonal matrix. However, the integration properties of this quadrature method are inferior to those of Gauss or GLL quadrature, being able to integrate exactly only polynomials up to order p, where p is the order of the interpolation function. Hence, the resulting approximation to the consistent mass matrix is degraded. An appreciation of this can be gained by noting now the differing optimisation criteria used in the definition of GLL and Fekete points, in particular the fact that Fekete points are optimised without regard to integration accuracy.

3.2.3 Subparametric Mapping

A common feature of the finite element method, is the introduction of a master element over which integration is performed. In this manner, by ensuring that integration is always executed over the same element of a standard form, then the efficiency of the computational procedure can be increased. The local element matrices, which will be derived in the remainder of this chapter, may then be computed in preprocessing and reused for each physical element in the mesh.

However, to permit this simplification, each physical mesh element must be mapped to the master element in computational space. This mapping introduces into the formulation a transformation known as the Jacobian matrix

$$\boldsymbol{J} = \begin{bmatrix} \dfrac{\partial x}{\partial \xi} & \dfrac{\partial y}{\partial \xi} \\ \dfrac{\partial x}{\partial \eta} & \dfrac{\partial y}{\partial \eta} \end{bmatrix} \tag{3.7}$$

where x,y and ξ,η are the physical and computational independent space variables respectively. The components of this matrix are termed the metrics of the Jacobian transformation. Therefore, the transformation of interpolation function gradients from physical to computational space can be written as

$$\begin{bmatrix} \dfrac{\partial N}{\partial \xi} \\ \dfrac{\partial N}{\partial \eta} \end{bmatrix} = \boldsymbol{J} \begin{bmatrix} \dfrac{\partial N}{\partial x} \\ \dfrac{\partial N}{\partial y} \end{bmatrix} \tag{3.8}$$

However, as will be seen in the discretised equations, it is more common to require the physical gradients to be expressed in terms of the computational gradients. Therefore, we simply invert the expression to

$$\begin{bmatrix} \dfrac{\partial N}{\partial x} \\ \dfrac{\partial N}{\partial y} \end{bmatrix} = \boldsymbol{J}^{-1} \begin{bmatrix} \dfrac{\partial N}{\partial \xi} \\ \dfrac{\partial N}{\partial \eta} \end{bmatrix} \tag{3.9}$$

where the inverse Jacobian is expressed as

$$\boldsymbol{J}^{-1} = \frac{1}{|\boldsymbol{J}|} \begin{bmatrix} \dfrac{\partial y}{\partial \eta} & -\dfrac{\partial y}{\partial \xi} \\ -\dfrac{\partial x}{\partial \eta} & \dfrac{\partial x}{\partial \xi} \end{bmatrix} \tag{3.10}$$

For a linear triangular element, the determinant of the Jacobian $|\boldsymbol{J}|$ is constant over the element and is simply a scaling factor from the computational to the physical domain. Therefore, in addition to the standard method of evaluating the determinant of a 2×2 matrix, the determinant of the Jacobian for a linear triangular element can be written as

$$|\boldsymbol{J}| = \frac{A^e_{xy}}{A^e_{\xi\eta}} \tag{3.11}$$

where $A^e_{xy}, A^e_{\xi\eta}$ are the element areas measured in the physical and computational spaces respectively.

Computation of the Jacobian matrix can be performed by reference to the interpolation functions for the element. At this stage, the mesh will comprise solely of straight-sided elements. Therefore, we can limit consideration, in this case, to linear interpolation functions for the triangular elements and bi-linear interpolation functions for the quadrilateral elements. These will be introduced in the remainder of this subsection, followed by the resulting form of the Jacobian matrix.

Quadrilateral Element Mapping

The general form of bi-linear mapping for a quadrilateral element can be expressed as

$$\boldsymbol{x} = N_1\boldsymbol{x}_1 + N_2\boldsymbol{x}_2 + N_3\boldsymbol{x}_3 + N_4\boldsymbol{x}_4 \tag{3.12}$$

where

$$N_1(\xi,\eta) = \frac{(1-\xi)(1-\eta)}{4} \tag{3.13a}$$

$$N_2(\xi,\eta) = \frac{(1+\xi)(1-\eta)}{4} \tag{3.13b}$$

$$N_3(\xi,\eta) = \frac{(1+\xi)(1+\eta)}{4} \tag{3.13c}$$

$$N_4(\xi,\eta) = \frac{(1-\xi)(1+\eta)}{4} \tag{3.13d}$$

Appropriate partial differentiation of this expression with respect to the computational independent variables gives the required metrics of the Jacobian matrix

$$\frac{\partial x}{\partial \xi} = \frac{1}{4}[(1-\eta)(x_2-x_1) + (1+\eta)(x_3-x_4)] \tag{3.14a}$$

$$\frac{\partial x}{\partial \eta} = \frac{1}{4}[(1-\xi)(x_4-x_1) + (1+\xi)(x_3-x_2)] \tag{3.14b}$$

$$\frac{\partial y}{\partial \xi} = \frac{1}{4}[(1-\eta)(y_2-y_1) + (1+\eta)(y_3-y_4)] \tag{3.14c}$$

$$\frac{\partial y}{\partial \eta} = \frac{1}{4}[(1-\xi)(y_4-y_1) + (1+\xi)(y_3-y_2)] \tag{3.14d}$$

However, due to the use of a structured quadrilateral mesh where each element is rectangular, as represented in Figure 3.2, these metrics can be simplified. Taking the first of these equations (3.14a) as an example, it can be seen that both lengths given by the subtraction of x coordinates are equal to the x dimension of the element h_x. Subsequently, further terms can be cancelled, resulting in an expression which is independent of η, and is merely equal to $h_x/2$. Similar simplifications can be applied to the remaining equations of this set, giving the Jacobian matrix

$$\boldsymbol{J} = \begin{bmatrix} \frac{h_x}{2} & 0 \\ 0 & \frac{h_y}{2} \end{bmatrix} \tag{3.15}$$

where h_x, h_y are the physical element lengths in the x and y directions respectively.

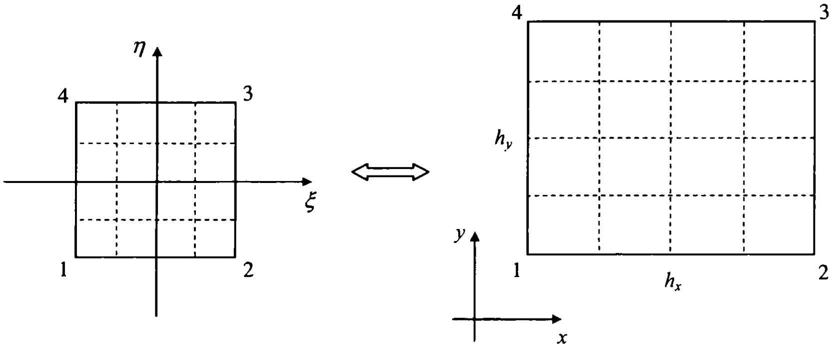

Figure 3.2: Mapping for quadrilateral elements

Triangular Element Mapping

Similarly, the general form of linear mapping for a triangular element, as shown in Figure 3.3, can be expressed as

$$\boldsymbol{x} = N_1\boldsymbol{x}_1 + N_2\boldsymbol{x}_2 + N_3\boldsymbol{x}_3 \tag{3.16}$$

where

$$N_1(\xi,\eta) = -\frac{\xi+\eta}{2} \tag{3.17a}$$

$$N_2(\xi,\eta) = \frac{1+\xi}{2} \tag{3.17b}$$

$$N_3(\xi,\eta) = \frac{1+\eta}{2} \tag{3.17c}$$

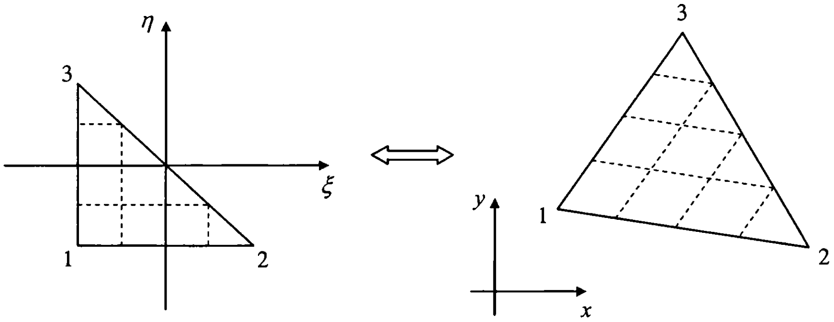

Figure 3.3: Mapping for triangular elements

In this case, application of partial differentiation to this expression with respect to the computational independent variables ξ and η ultimately gives

$$\boldsymbol{J} = \frac{1}{2}\begin{bmatrix} x_2 - x_1 & y_2 - y_1 \\ x_3 - x_1 & y_3 - y_1 \end{bmatrix} \tag{3.18}$$

3.3 Temporal Discretisation

The governing equations under consideration here will be the linearized Euler equations of acoustics. Thus, we express (2.33) in vector form

$$\frac{\partial \boldsymbol{U}}{\partial t} + \frac{\partial \boldsymbol{F}}{\partial x} + \frac{\partial \boldsymbol{G}}{\partial y} = 0 \tag{3.19}$$

where the vector variables are

$$\boldsymbol{U} = \begin{bmatrix} u \\ v \\ p \end{bmatrix} \qquad \boldsymbol{F} = \begin{bmatrix} p \\ 0 \\ u \end{bmatrix} \qquad \boldsymbol{G} = \begin{bmatrix} 0 \\ p \\ v \end{bmatrix}$$

and the scalar components of these vectors are the pressure, p, and the fluid velocities, u and v, in the x and y directions respectively.

We proceed with the temporal discretisation from the recommendation made at the end of Chapter 2: to limit the effects of instability, a Taylor Galerkin scheme will be used. Derivation of the semi-discrete equations for second and third order schemes are included below.

3.3.1 Second Order Taylor Galerkin Scheme (TG2)

As seen previously for the scalar convection equation, the Taylor Galerkin discretisation procedure begins with the temporal discretisation. Therefore, we express a Taylor series expansion for the vector variable

$$\Delta \boldsymbol{U} = \Delta t \left. \frac{\partial \boldsymbol{U}}{\partial t} \right|^n + \frac{\Delta t^2}{2} \left. \frac{\partial^2 \boldsymbol{U}}{\partial t^2} \right|^n + \frac{\Delta t^3}{3!} \left. \frac{\partial^3 \boldsymbol{U}}{\partial t^3} \right|^n + \frac{\Delta t^4}{4!} \left. \frac{\partial^4 \boldsymbol{U}}{\partial t^4} \right|^n + \ldots \tag{3.20}$$

and for the second order Taylor Galerkin (TG2) scheme, we truncate this expansion to include only second and lower order derivatives, giving the approximation

$$\Delta \boldsymbol{U} \approx \Delta t \left. \frac{\partial \boldsymbol{U}}{\partial t} \right|^n + \frac{\Delta t^2}{2} \left. \frac{\partial^2 \boldsymbol{U}}{\partial t^2} \right|^n \tag{3.21}$$

Using the governing equations (3.19) to transform the temporal derivatives to spatial derivatives, we obtain

$$\Delta \boldsymbol{U} = -\Delta t \left\{ \left. \frac{\partial \boldsymbol{F}}{\partial x} \right|^n + \left. \frac{\partial \boldsymbol{G}}{\partial y} \right|^n \right\} - \frac{\Delta t^2}{2} \frac{\partial}{\partial t} \left\{ \left. \frac{\partial \boldsymbol{F}}{\partial x} \right|^n + \left. \frac{\partial \boldsymbol{G}}{\partial y} \right|^n \right\} \tag{3.22}$$

As a temporal derivative is still present in the second order term, we must rearrange these derivatives to facilitate repetition of the substitution

$$\left. \frac{\partial}{\partial t} \left(\frac{\partial \boldsymbol{F}}{\partial x} \right) \right|^n = \left. \frac{\partial}{\partial x} \left(\frac{\partial \boldsymbol{F}}{\partial \boldsymbol{U}} \frac{\partial \boldsymbol{U}}{\partial t} \right) \right|^n = \frac{\partial}{\partial x} \left[\boldsymbol{A} \left(- \left. \frac{\partial \boldsymbol{F}}{\partial x} \right|^n - \left. \frac{\partial \boldsymbol{G}}{\partial y} \right|^n \right) \right] \tag{3.23a}$$

$$\left. \frac{\partial}{\partial t} \left(\frac{\partial \boldsymbol{G}}{\partial y} \right) \right|^n = \left. \frac{\partial}{\partial y} \left(\frac{\partial \boldsymbol{G}}{\partial \boldsymbol{U}} \frac{\partial \boldsymbol{U}}{\partial t} \right) \right|^n = \frac{\partial}{\partial y} \left[\boldsymbol{B} \left(- \left. \frac{\partial \boldsymbol{F}}{\partial x} \right|^n - \left. \frac{\partial \boldsymbol{G}}{\partial y} \right|^n \right) \right] \tag{3.23b}$$

where $\boldsymbol{A} = \partial \boldsymbol{F} / \partial \boldsymbol{U}$ and $\boldsymbol{B} = \partial \boldsymbol{G} / \partial \boldsymbol{U}$ are the Jacobian matrices. Noting also that the spatial derivatives of the fluxes can be expressed as $\partial \boldsymbol{F} / \partial x = \boldsymbol{A}(\partial \boldsymbol{U} / \partial x)$ and $\partial \boldsymbol{G} / \partial y = \boldsymbol{B}(\partial \boldsymbol{U} / \partial y)$, insertion of (3.23) into (3.22) leads to the semi-discrete equation

$$\begin{aligned} \Delta \boldsymbol{U} = & -\Delta t \left[\boldsymbol{A} \left. \frac{\partial \boldsymbol{U}}{\partial x} \right|^n + \boldsymbol{B} \left. \frac{\partial \boldsymbol{U}}{\partial y} \right|^n \right] \\ & + \frac{\Delta t^2}{2} \left[\frac{\partial}{\partial x} \left(\boldsymbol{A}^2 \left. \frac{\partial \boldsymbol{U}}{\partial x} \right|^n + \boldsymbol{A}\boldsymbol{B} \left. \frac{\partial \boldsymbol{U}}{\partial y} \right|^n \right) + \frac{\partial}{\partial y} \left(\boldsymbol{B}\boldsymbol{A} \left. \frac{\partial \boldsymbol{U}}{\partial x} \right|^n + \boldsymbol{B}^2 \left. \frac{\partial \boldsymbol{U}}{\partial y} \right|^n \right) \right] \end{aligned} \tag{3.24}$$

3.3.2 Two-step Third Order Taylor Galerkin Scheme (TG3-2S)

Due to the similarity of the equation forms in both steps of the TG3-2S scheme (2.79) to that of the TG2 scheme (2.75), application of the above procedure, in this case, will result in a scheme with repeated application of very similar semi-discrete equations. As can be seen, the only difference will be in the coefficients of each term and the use of the intermediate solution $\tilde{\boldsymbol{U}}$ in equation (3.25b) for the second step

$$\begin{aligned}\Delta\tilde{\boldsymbol{U}} = &-\frac{1}{3}\Delta t\left[\boldsymbol{A}\frac{\partial \boldsymbol{U}}{\partial x}\bigg|^{n} + \boldsymbol{B}\frac{\partial \boldsymbol{U}}{\partial y}\bigg|^{n}\right] \\ &+\alpha\Delta t^2\left[\frac{\partial}{\partial x}\left(\boldsymbol{A}^2\frac{\partial \boldsymbol{U}}{\partial x}\bigg|^{n} + \boldsymbol{AB}\frac{\partial \boldsymbol{U}}{\partial y}\bigg|^{n}\right) + \frac{\partial}{\partial y}\left(\boldsymbol{BA}\frac{\partial \boldsymbol{U}}{\partial x}\bigg|^{n} + \boldsymbol{B}^2\frac{\partial \boldsymbol{U}}{\partial y}\bigg|^{n}\right)\right] \qquad (3.25a)\end{aligned}$$

$$\begin{aligned}\Delta\boldsymbol{U} = &-\Delta t\left[\boldsymbol{A}\frac{\partial \boldsymbol{U}}{\partial x}\bigg|^{n} + \boldsymbol{B}\frac{\partial \boldsymbol{U}}{\partial y}\bigg|^{n}\right] \\ &+\frac{\Delta t^2}{2}\left[\frac{\partial}{\partial x}\left(\boldsymbol{A}^2\frac{\partial \tilde{\boldsymbol{U}}}{\partial x} + \boldsymbol{AB}\frac{\partial \tilde{\boldsymbol{U}}}{\partial y}\right) + \frac{\partial}{\partial y}\left(\boldsymbol{BA}\frac{\partial \tilde{\boldsymbol{U}}}{\partial x} + \boldsymbol{B}^2\frac{\partial \tilde{\boldsymbol{U}}}{\partial y}\right)\right] \qquad (3.25b)\end{aligned}$$

The definition of the constant $\alpha = 1/9$ ensures that this two-step procedure reproduces the same phase-speed characteristics as the single-step TG3 scheme [41].

3.4 SEM Formulation on Quadrilateral Elements

The initial development of a spectral element solution procedure for wave scattering problems on quadrilateral meshes can be seen in the results of previous research work [34]. This work included the analysis of simple straight-sided wave scattering models.

The fully discretised equation system, using a continuous Galerkin approximation, is derived here from the weighted residual over the domain of the semi-discrete equation (3.24) Ω, for the TG2 scheme

$$\begin{aligned}\int_\Omega N_I \Delta\hat{\boldsymbol{U}}\, d\Omega = &-\Delta t\int_\Omega N_I\left(\boldsymbol{A}\frac{\partial \hat{\boldsymbol{U}}}{\partial x}\bigg|^{n} + \boldsymbol{B}\frac{\partial \hat{\boldsymbol{U}}}{\partial y}\bigg|^{n}\right) d\Omega \\ &+\frac{\Delta t^2}{2}\int_\Omega N_I\left(\boldsymbol{A}^2\frac{\partial^2 \hat{\boldsymbol{U}}}{\partial x^2}\bigg|^{n} + \boldsymbol{AB}\frac{\partial^2 \hat{\boldsymbol{U}}}{\partial x \partial y}\bigg|^{n} + \boldsymbol{BA}\frac{\partial^2 \hat{\boldsymbol{U}}}{\partial x \partial y}\bigg|^{n} + \boldsymbol{B}^2\frac{\partial^2 \hat{\boldsymbol{U}}}{\partial y^2}\bigg|^{n}\right) d\Omega \qquad (3.26)\end{aligned}$$

Following the discussion of natural boundary conditions in Chapter 2, the terms of the full weighted residual statement, over both the domain Ω and domain boundary Γ, will simplify when integration by parts and Green's lemma are applied, giving

$$\begin{aligned}\int_\Omega N_I \Delta\hat{\boldsymbol{U}}\, d\Omega \;=\; & \Delta t \int_\Omega \left(\boldsymbol{A}\hat{\boldsymbol{U}} \frac{\partial N_I}{\partial x}\bigg|^n + \boldsymbol{B}\hat{\boldsymbol{U}} \frac{\partial N_I}{\partial y}\bigg|^n \right) d\Omega \\ & -\frac{\Delta t^2}{2} \int_\Omega \left(\boldsymbol{A}^2 \frac{\partial N_I}{\partial x}\frac{\partial \hat{\boldsymbol{U}}}{\partial x}\bigg|^n + \boldsymbol{AB}\frac{\partial N_I}{\partial x}\frac{\partial \hat{\boldsymbol{U}}}{\partial y}\bigg|^n \right. \\ & \qquad \left. +\boldsymbol{BA}\frac{\partial N_I}{\partial y}\frac{\partial \hat{\boldsymbol{U}}}{\partial x}\bigg|^n + \boldsymbol{B}^2\frac{\partial N_I}{\partial y}\frac{\partial \hat{\boldsymbol{U}}}{\partial y}\bigg|^n \right) d\Omega \\ & -\Delta t \int_\Gamma \left(N_I \boldsymbol{f}^{n+\frac{1}{2}} \cdot \boldsymbol{n} \right) d\Gamma \end{aligned}$$

Expressing the finite element approximation of the unknown distribution as

$$\hat{\boldsymbol{U}} = N_J \boldsymbol{U}_J$$

noting that, for quadrilateral elements the interpolation functions are defined as $N(x,y) = P(x) \otimes Q(x)$, the fully discretised form of the equation becomes

$$M_{IJ}\Delta\boldsymbol{U}_J = \Delta t C_{IJ}\boldsymbol{U}^n_J - \frac{\Delta t^2}{2} K_{IJ}\boldsymbol{U}^n_J + \Delta t f_I \tag{3.27}$$

where

$$\begin{aligned} M_{IJ} &= \int_\Omega P_I Q_I P_J Q_J \, d\Omega \\ C_{IJ} &= \int_\Omega \left(\boldsymbol{A}\frac{dP_I}{dx} Q_I P_J Q_J + \boldsymbol{B} P_I \frac{dQ_I}{dy} P_J Q_J \right) d\Omega \\ K_{IJ} &= \int_\Omega \left(\boldsymbol{A}^2 \frac{dP_I}{dx} Q_I \frac{dP_J}{dx} Q_J + \boldsymbol{AB}\frac{dP_I}{dx} Q_I P_J \frac{dQ_J}{dy} \right. \\ & \qquad \left. +\boldsymbol{BA} P_I \frac{dQ_I}{dy}\frac{dP_J}{dx} Q_J + \boldsymbol{B}^2 P_I \frac{dQ_I}{dy} P_J \frac{dQ_J}{dy} \right) d\Omega \\ f_I &= -\Delta t \int_{\Gamma_{PROP}} N_I \boldsymbol{f}^{n+\frac{1}{2}} \cdot \boldsymbol{n}\, d\Gamma \;-\; \Delta t \int_{\Gamma_{ABC}} N_I \boldsymbol{f}^{n+\frac{1}{2}} \cdot \boldsymbol{n}\, d\Gamma \end{aligned}$$

Note here that the terms within the boundary integrals are represented by the fluxes f for clarity. The actual boundary condition will be applied by an appropriate means, as will be discussed. It should also be noted that these fluxes f must be computed at the half-step $n + 1/2$. Additionally, Γ_{PROP} and Γ_{ABC} denote the sections of the boundaries where the test propagation condition and the absorbing boundary condition, to be discussed in Section 3.7, will be applied.

3.5 SEM Formulation on Triangular Elements

Beginning with the same semi-discrete equation (3.24) for the TG2 scheme, a similar set of equations is produced for the formulation of the spectral element method on the triangular part of the mesh. However, the use of fully two-dimensional interpolation functions results in slightly different forms for the system matrices.

$$M_{IJ}\Delta \boldsymbol{U}_J = \Delta t C_{IJ}\boldsymbol{U}_J^n - \frac{\Delta t^2}{2}K_{IJ}\boldsymbol{U}_J^n + \Delta t f_I \tag{3.28}$$

where

$$\begin{aligned}
M_{IJ} &= \int_\Omega N_I N_J \, d\Omega \\
C_{IJ} &= \int_\Omega \left(\boldsymbol{A}\frac{\partial N_I}{\partial x}N_J + \boldsymbol{B}\frac{\partial N_I}{\partial y}N_J \right) d\Omega \\
K_{IJ} &= \int_\Omega \left(\boldsymbol{A}^2\frac{\partial N_I}{\partial x}\frac{\partial N_J}{\partial x} + \boldsymbol{AB}\frac{\partial N_I}{\partial x}\frac{\partial N_J}{\partial y} \right. \\
&\qquad \left. + \boldsymbol{BA}\frac{\partial N_I}{\partial y}\frac{\partial N_J}{\partial x} + \boldsymbol{B}^2\frac{\partial N_I}{\partial y}\frac{\partial N_J}{\partial y} \right) d\Omega \\
f_I &= -\Delta t \int_{\Gamma_{PROP}} N_I \boldsymbol{f}^{n+\frac{1}{2}} \cdot \boldsymbol{n} \, d\Gamma \; - \; \Delta t \int_{\Gamma_{ABC}} N_I \boldsymbol{f}^{n+\frac{1}{2}} \cdot \boldsymbol{n} \, d\Gamma
\end{aligned}$$

and Γ_{PROP} and Γ_{ABC} denote the partitioning of the boundary as stated above.

As previously mentioned, the use of Fekete quadrature for the computation of the mass matrix $\boldsymbol{M}$ results in a diagonal matrix, thus providing significant computational savings. However, although this approximation is legitimate and provides good solution accuracy when used with quadrilateral elements, the inferiority of Fekete quadrature suggests that the results for the corresponding triangular formulation will be inaccurate by comparison. Therefore, to alleviate this problem, the procedure discussed in the next section is proposed.

3.6 Mass Iteration

For clarity, we return to a general system of equations, which in this instance we write as

$$\boldsymbol{M}\boldsymbol{U}^{n+1} = \boldsymbol{R}^{n} \tag{3.29}$$

where $\boldsymbol{U}$ is the unknown vector at time $n+1$, $\boldsymbol{M}$ is the consistent mass matrix and $\boldsymbol{R}$ is a typical right hand side vector representing the operators applied to the solution at the previous time-step, n. To obtain the updated solution $\boldsymbol{U}^{n+1}$, inversion of the consistent mass matrix is required which, for a continuous Galerkin approximation method, involves a large global system matrix. This is a significantly computationally demanding procedure which increases in relation to the size and refinement of the computational domain. Approximation of the consistent mass matrix, following the diagonalisation technique described above, results in a lumped mass matrix, which reduces this computational expense. However, for triangular elements, this is likely to significantly degrade the accuracy of the solution due to the inaccuracy of the numerical quadrature.

To improve the approximation to the consistent mass form and, thus, regain solution accuracy, an iteration procedure has been used [45]. Choosing to express the consistent mass matrix $\boldsymbol{M}$ as

$$\boldsymbol{M} = \boldsymbol{M}_L + (\boldsymbol{M} - \boldsymbol{M}_L) \tag{3.30}$$

where $\boldsymbol{M}_L$ represents the lumped mass matrix, and inserting this equation (3.30) into (3.29), leads to the iterative equation

$$\boldsymbol{U}^{n+1(r+1)} = \boldsymbol{M}_L^{-1}\boldsymbol{R}^{n} - \boldsymbol{M}_L^{-1}(\boldsymbol{M} - \boldsymbol{M}_L)\boldsymbol{U}^{n+1(r)} \tag{3.31}$$

with r representing the number of iterations. In this way, the approximation to the consistent mass matrix can be improved over successive iterations, while maintaining the requirement for inversion of the lumped form of the mass matrix only.

Closer examination of this iterative equation reveals that, with initial values of

$\boldsymbol{U}^{n+1(0)} = \mathbf{0}$, the first iteration is simply the former lumped mass approximation

$$\boldsymbol{U}^{n+1(1)} = \boldsymbol{M}_L^{-1}\boldsymbol{R}^n \tag{3.32}$$

Therefore, it is clear that as the iterations proceed, the approximation should improve. An in-depth explanation of the motivation for this procedure and an analysis of the potential improvements in accuracy available for linear elements can be found in [46].

However, it should be noted, that the improvement in solution accuracy is achieved at the expense of the efficiency of the method. Naturally, as the number of iterations is increased the computational work will increase. Therefore, a compromise is required which facilitates an appropriate solution at an acceptable computational cost.

3.7 Absorbing Boundary Condition

Physical wave propagation and scattering problems are typically modelled within open regions where the incident wave field is assumed to originate in the far field. Consequently, true representation of these models would necessitate a physical domain of infinite extent. Due to the constraints of computational capability, the generation of a corresponding infinite computational domain is obviously impossible. Therefore, the preparation of an appropriate numerical model will require some form of approximation to this property of the domain.

For wave scattering models, the wave field can be assumed to propagate outwards from the scattering object. Therefore, as most interest in this type of analysis is focused on the solution around the surface, an artificial boundary can be formed to truncate the open region and form a closed space. Now, the only condition that must be satisfied on this boundary is that the outgoing component of the wave field is completely transmitted. If this condition is not satisfied, then spurious reflected waves will result, which subsequently propagate back towards the scattering object and pollute the solution.

For the initial development of the model and to facilitate a preliminary validation of the method, a first order upwind Roe flux is deemed sufficient as a simple absorbing boundary condition (ABC). This approximates a transparent interface by dictating that the information that defines the solution at the boundary comes solely from within the domain.

A general expression for a Roe flux, resolved normally to the boundary, can be expressed as

$$\boldsymbol{f}_n^{Roe} = \frac{1}{2}\left\{\boldsymbol{f}_n^L + \boldsymbol{f}_n^R - |\boldsymbol{A}_n|(\boldsymbol{U}^R - \boldsymbol{U}^L)\right\} \tag{3.33}$$

where $\boldsymbol{f}_n^L$ and $\boldsymbol{f}_n^R$ represent the normal flux vectors and $\boldsymbol{U}^L$ and $\boldsymbol{U}^R$ represent the unknown solution vectors to the left and right of the boundary respectively. $\boldsymbol{A}_n$ is the normal Jacobian matrix of the governing equation system

$$\boldsymbol{A}_n = n_x\boldsymbol{A} + n_y\boldsymbol{B} = \begin{bmatrix} 0 & 0 & n_x \\ 0 & 0 & n_y \\ n_x & n_y & 0 \end{bmatrix} \tag{3.34}$$

where $\boldsymbol{A}$ and $\boldsymbol{B}$ are the x and y components of the Jacobian matrix, as defined in (3.23). Following the evaluation of the eigenvalues and corresponding eigenvectors of $\boldsymbol{A}_n$, the eigen decomposition theorem, written as

$$|\boldsymbol{A}_n| = \boldsymbol{P}|\Lambda|\boldsymbol{P}^{-1} \tag{3.35}$$

where Λ is the diagonal matrix of eigenvalues and $\boldsymbol{P}$ is the matrix of eigenvectors, can be used to obtain its magnitude

$$|\boldsymbol{A}_n| = \begin{bmatrix} n_x^2 & n_xn_y & 0 \\ n_xn_y & n_y^2 & 0 \\ 0 & 0 & 1 \end{bmatrix} \tag{3.36}$$

Noting that the unknown and flux fields are assumed to be zero outside the domain, thus expressing $\boldsymbol{U}^R = 0$ and $\boldsymbol{f}_n^R = 0$, insertion of (3.36) into the expression for the Roe flux (3.33) gives

$$\boldsymbol{f}_n^{Roe} = \frac{1}{2}\left(n_x\begin{Bmatrix} p^L \\ 0 \\ u^L \end{Bmatrix} + n_y\begin{Bmatrix} 0 \\ p^L \\ v^L \end{Bmatrix} + \begin{bmatrix} n_x^2 & n_xn_y & 0 \\ n_xn_y & n_y^2 & 0 \\ 0 & 0 & 1 \end{bmatrix}\begin{Bmatrix} u^L \\ v^L \\ p^L \end{Bmatrix}\right) \tag{3.37}$$

where the normal flux is computed from its x and y components as

$$\boldsymbol{f}_n = n_x\boldsymbol{F} + n_y\boldsymbol{G} \tag{3.38}$$

and the vector components are those from (3.19).

3.8 Validation

At this stage of the development, validation is required to assess the method's stability and accuracy, thus enabling a conclusion to be drawn on the suitability of the method before proceeding further. This will be performed using a simple propagation test, in which a sinusoidal wave is propagated through a domain. The results of this test will facilitate the comparison of the accuracy of the method on both the quadrilateral and triangular elements, with and without the application of the proposed mass iteration procedure.

3.8.1 Computational Model

Tests are performed on two-dimensional meshes of structured quadrilateral and triangular elements. To replicate the requirements of practical wave scattering problems, an extended propagation time will be used. Consequently, the wave will be propagated for 100 cycles and we will focus on the fidelity of the waveform in the vicinity of the 95^{th} wavelength. To reduce the computational workload, propagation is defined to occur solely in the x-direction of a long, narrow domain (500×2 unit dimension), the main extent of which lying along the x-axis. This is accomplished by imposing a propagation boundary condition on the left boundary of the domain, at $x = 0$. Representations of the quadrilateral and triangular meshes can be seen in Figure 3.4.

The waveform will be a simple sinusoidal function, which can be expressed as

$$p = p_0 \sin(k_x x - \omega t) \tag{3.39}$$

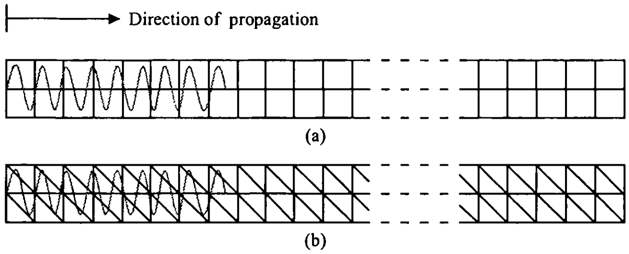

Figure 3.4: Representations of (a) the quadrilateral mesh and (b) the triangular mesh for the wave propagation test

where a unit value will be taken for the reference pressure p_0 and the x-component of the wavenumber k_x is $2\pi/5$, which means that the wavelength is $\lambda = 5$.

At the downstream boundary, the first order upstream ABC will be imposed to limit reflection of the wave back into the domain.

3.8.2 Results

To establish the accuracy of the higher order method, we focus on third order elements, thus enabling a comparison of the effect of mass iteration on both quadrilateral and triangular elements. Note that an analysis with second order triangular elements is not possible, as the lumping technique using the corresponding set of Fekete points generates zero entries on the mass matrix diagonal, thus precluding matrix inversion.

Results are presented for a location near to the downstream boundary of the domain, between the 93^{rd} and 97^{th} wavelengths, on the longitudinal centre-line. For the cubic quadrilateral elements, the results shown in Figures 3.5(a) and 3.5(b) display little improvement in the solution when iteration is applied. The reason for this is the initial quality of the lumped mass matrix approximation, due to the accuracy of the GLL quadrature method. However, when considering the triangular elements, the inaccuracy of the initial lumped approximation can be seen in Figure 3.5(c). This results from the use of an inferior Fekete quadrature for the matrix integral evaluation. Consequently, the use of the proposed mass iteration procedure offers a significant improvement in accuracy evident in both the amplitude and phase of the computa-

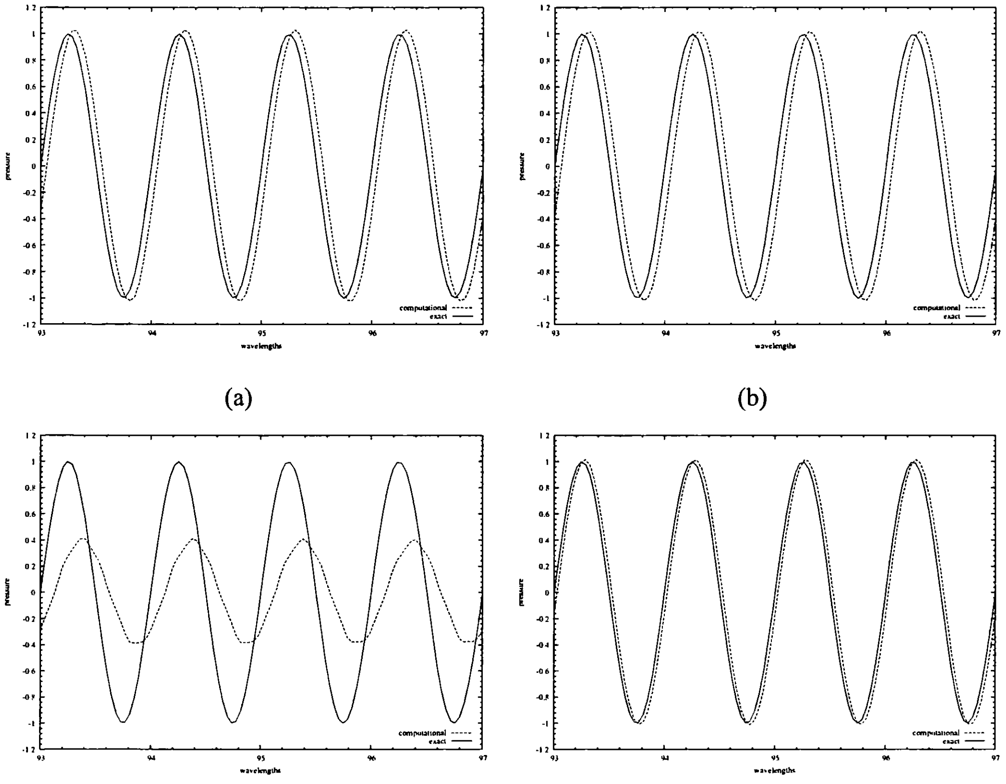

(a) (b)

(c) (d)

Figure 3.5: Propagation test results: (a) Quadrilateral elements with no iterations (b) Quadrilateral elements with 5 iterations (c) Triangular elements with no iterations (d) Triangular elements with 5 iterations

tional results presented in Figure 3.5(d).

These initial results were very promising, suggesting that an iteration procedure, applied to the triangular part of the domain, could offer an alternative to simply increasing the order of the elements. A compromise could have been sought which optimised the number of iterations and order of the elements to give the most efficient solution method. However, when attempting to apply the same procedure to elements of fourth order or higher, unforeseen difficulties were encountered [47].

When the iteration procedure is applied to fourth order triangular elements, the method fails to converge, giving unstable solutions. A similar outcome is found with higher order triangular elements. The cause of this divergence was determined by close inspection of the iterative equation (3.31) and, in particular, the iterative matrix

$$\boldsymbol{B} = \boldsymbol{M}_L^{-1}(\boldsymbol{M} - \boldsymbol{M}_L) \tag{3.40}$$

Convergence of an iterative scheme is dependent on its spectral radius, which when expressed in matrix form, is equal to the maximum absolute value of the eigenvalues [48]. If this value is less than unity, then convergence will occur; if the value is greater than this threshold, the solution will diverge. When the matrix $\boldsymbol{B}$, for these higher order elements, is examined, some of its eigenvalues are seen to be greater than unity. Therefore, divergence of the iterative procedure is fundamentally inevitable. A more detailed explanation of this concept and analysis of the iterative matrices for different element order can be found in Appendix A.

As a final remark, it should be noted that there are more complex methods, such as the conjugate gradient method, with which convergence of the solution can be obtained. However, due to the increased computational work required with these methods, their consideration is not included here.

Consequently, as it is desired that an efficient computational procedure be available for a larger range of element order, thus facilitating a broader analysis, the application of this simple iterative procedure is deemed inappropriate during further development of the method. This means that an alternative method of improving the solution accuracy on the higher order triangular elements is needed. Further discussion of this aspect of the method will be conducted in the next chapter.

3.9 Convergence Analysis

To conclude the investigation of the spectral element method applied to quadrilateral elements, a convergence analysis is conducted. This is performed to provide further validation and to assess the potential improvement in solution accuracy as element order is increased.

3.9.1 Computational Model

For this analysis, the computational model will involve the propagation of a single Gaussian pulse

$$p = p_0 e^{-(x-x_0-v_0 t)^2} \tag{3.41}$$

across a domain, where v_0 is the propagation speed and x_0 the initial position of the centre of the pulse. The domain, a representation of which can be seen in Figure 3.6, will be 50×50 units in dimension and the pulse will propagate in the x-direction, with a unit propagation speed, for 10 time units from $x_0 = 20$ to $x = 30$. This arrangement is used in an attempt to limit boundary effects.

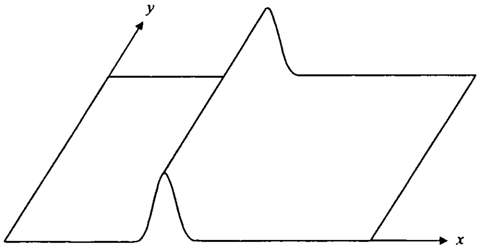

Figure 3.6: Representation of the computational domain for the convergence analysis

Various mesh refinements (h-refinement) will be used, upon which p-refinement will be performed by increasing the order of the elements. Solution accuracy is measured along the centre-line of the domain using an L^2-error norm of the pressure p.

$$L^2\ norm = \sqrt{\int_\Gamma (p_{exact} - p_{approx})^2\, d\Gamma} \tag{3.42}$$

3.9.2 Results

To strengthen the reliability of the results, the analysis was repeated on meshes of various refinement, the coarsest of which is shown in Figure 3.7. As can be seen in Figure 3.8, where the TG2 time-stepping scheme was used, p-convergence is evident on each mesh used in the analysis.

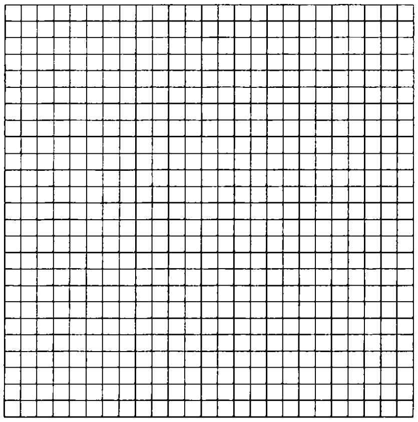

Figure 3.7: Coarse mesh (25x25) for convergence analysis

The reduction in convergence rate for the most refined mesh can be attributed to the limit of temporal accuracy associated with the TG2 scheme. A higher order temporal scheme, such as the TG3-2S scheme, permits convergence to continue beyond this point. Therefore, the analysis was repeated with this scheme to demonstrate this continuation in convergence, seen in Figure 3.9.

Furthermore, an alternative family of schemes known as the Runge-Kutta time-stepping schemes were tested as further validation. A derivation of the governing discretised equations for the fourth order Runge-Kutta (RK4) scheme is included in Appendix B. The results for the convergence analysis are presented in Figure 3.10. Once again, it is evident that the higher temporal accuracy achieved by this scheme permits exponential convergence to continue beyond that possible with the TG2 scheme.

Comparison of the convergence analysis results using these various temporal schemes demonstrates little difference in the accuracy of the models for all but the most refined meshes. For these extremes, higher order temporal schemes, such as TG3-2S and RK4, are needed to facilitate convergence for the higher element orders. Therefore, while reasonable levels of mesh refinement are used, the TG2 scheme offers a sufficient level of accuracy to assess the advantages of higher order spatial discretisation. Consequently, it is this scheme that will be used mainly in the remainder

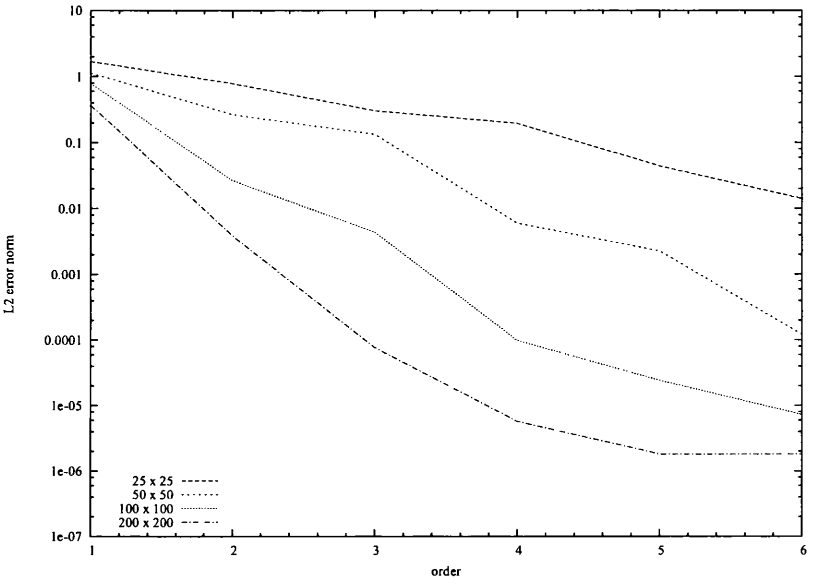

Figure 3.8: p-Convergence results for the SEM with varying mesh refinement using a TG2 scheme

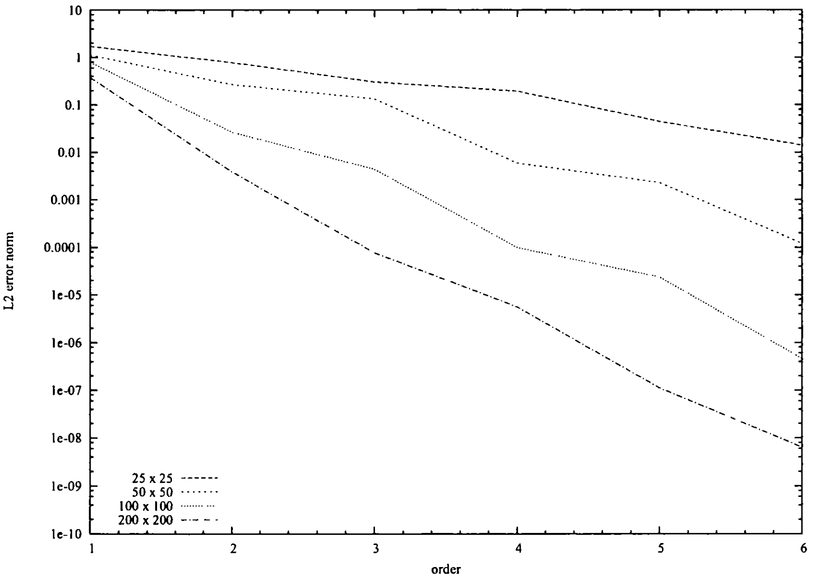

Figure 3.9: p-Convergence results for the SEM with varying mesh refinement using a TG3-2S scheme

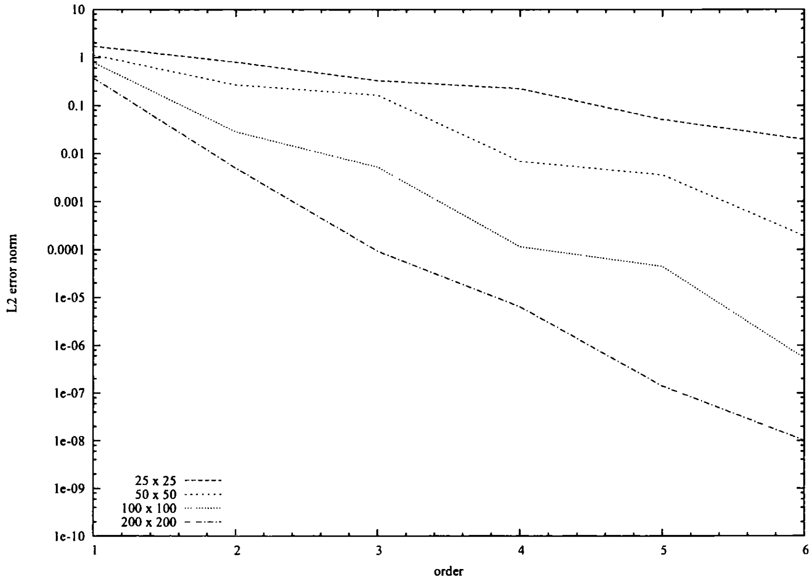

Figure 3.10: p-Convergence results for the SEM with varying mesh refinement using a RK4 scheme

of this work. However, it will be prudent if recourse is made to the higher order time-stepping methods when performing the convergence analyses for the alternative solution procedures, as will be subsequently introduced.

We can now be satisfied that the spectral element component of the method, applied to the quadrilateral part of the computational domain, is working and has the potential to achieve p-convergence for wave propagation problems.

3.10 Conclusion

Development and analysis of the spectral element formulation on both quadrilateral and triangular elements has been presented. The inaccuracies inherent in the diagonal formulation of the SEM on triangular elements were discussed and a mass iteration procedure was proposed to improve the solution accuracy. This was shown to offer significant improvements to the solution using third order elements. However, extension of the method to higher order elements was proven to be flawed due to an ill-conditioned iterative matrix. Consequently, further development of the method is not recommended and an alternative solution method is required. This discussion continues in the following chapter.

On the other hand, application of the standard diagonal formulation of the SEM on quadrilateral elements demonstrated the potential to generate accurate solutions efficiently when compared to lower order schemes. Therefore, the intended use of the method on the open regions of wave scattering models, is deemed appropriate.

Chapter 4

Spectral Discontinuous Galerkin Method

4.1 Introduction

Following the recommendations of the previous chapter, an alternative solution method is required for the triangular part of the mesh. Due to the intended location of this unstructured triangular mesh, adjacent to the scattering object, the solution method must be capable of providing high solution accuracy, although once again, in an efficient manner.

A promising option is the spectral discontinuous Galerkin (DG) method. Not only does the higher order capabilities of this method suggest the potential for exponential convergence, but also, it is expected that the discontinuous nature of this procedure provides a mechanism through which any singularities in the solution can be appropriately handled.

As will be seen, the formulation of the variational statement for the discontinuous Galerkin method, permits the use of a consistent mass matrix without the necessity for computationally expensive matrix inversion of a global matrix. Consequently, a certain level of efficiency is also ensured.

Therefore, in this chapter, a higher order discontinuous Galerkin method will be presented, followed by validation and analysis of convergence rates.

4.1.1 Background

The main difference between continuous and discontinuous finite element methods is the presence of additional degrees of freedom at the element boundaries. These effectively take the form of additional boundary nodes, as the neighbouring elements do not share any nodes. Representations of the meshes used in continuous and discontinuous finite element methods are displayed in Figure 4.1. It is this feature of the DG method that enables discontinuous solutions to be approximated accurately over the domain, as steps in the solution can occur at element interfaces [49].

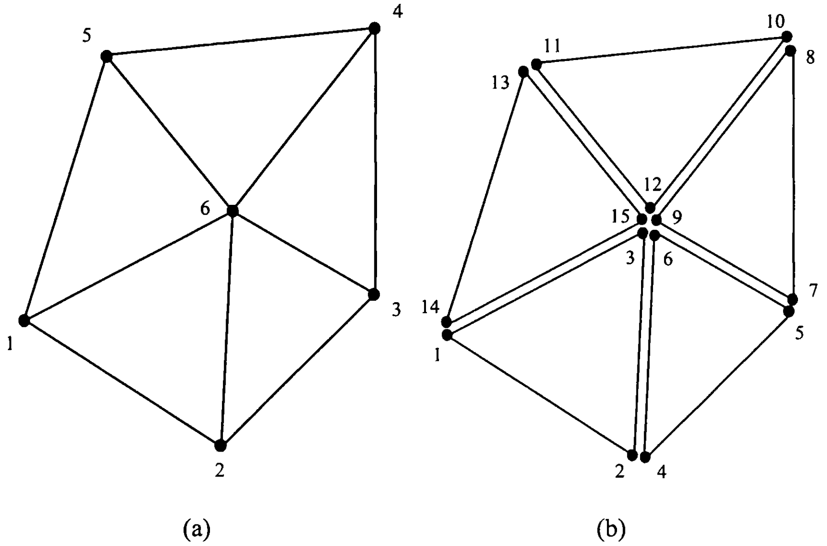

Figure 4.1: Example mesh elements and numbering (a) Continuous finite element (b) Discontinuous finite element

Due to the discontinuous nature of the discretisation, the solution within each element is independent from that contained within each of its neighbours. Therefore, coupling of the solution is achieved by approximate numerical fluxes evaluated over each element boundary. An obvious advantage of this fact is that local conservation is ensured as the flux outflow from one element must equal the flux inflow into its neighbour over the shared boundary.

Another advantage of the DG method, again due to the schemes discontinuous formulation, is that it offers an efficient solution method for time dependent or hyperbolic problems. As the mass matrices are formed locally over each element, the inversion of a global mass matrix, as discussed in the previous chapter for the continuous spectral element method, is avoided. Therefore, this explicit, block-diagonal form reduces the computational cost needed to temporally update the solution.

4.2 Interpolation Functions and Numerical Integration

As for the previous spectral element formulation on triangular elements, the interpolation functions will be defined using Lagrange interpolation directly through a two-dimensional set of Fekete points. These points offer high interpolation properties, which accounts for their use in this finite element method. They are also coincident with Gauss-Legendre-Lobatto (GLL) points along the boundaries of the quadrilateral elements, thus providing a simplified coupling procedure for a hybrid solution method.

However, contrary to the previous diagonal SEM formulation, the spectral DG method will utilise a Gaussian quadrature for integration of all matrix integrals. Consequently, full consistent element mass matrices will be formed, thus improving the accuracy of the solution on triangular elements. Note also, whereas the previous diagonal SEM formulation prohibited the use of second order triangular elements due to the presence of zero values on the diagonal of the mass matrix, this condition does not occur here. The alternative numerical integration method removes this restriction, enabling a broader range of element orders to be used.

4.3 Temporal Discretisation

The temporal discretisation will be performed using the same Taylor Galerkin methods as introduced for the spectral element method in Section 3.3. Therefore, for the linearized Euler equations (3.19), the semi-discrete equation using the second order Taylor Galerkin scheme (TG2) can be written as equation (3.24)

$$\begin{aligned}\Delta \boldsymbol{U} = -\Delta t\left[\boldsymbol{A}\frac{\partial \boldsymbol{U}}{\partial x}\bigg|^{n} + \boldsymbol{B}\frac{\partial \boldsymbol{U}}{\partial y}\bigg|^{n}\right] \\ +\frac{\Delta t^2}{2}\left[\frac{\partial}{\partial x}\left(\boldsymbol{A}^2\frac{\partial \boldsymbol{U}}{\partial x}\bigg|^{n} + \boldsymbol{AB}\frac{\partial \boldsymbol{U}}{\partial y}\bigg|^{n}\right) + \frac{\partial}{\partial y}\left(\boldsymbol{AB}\frac{\partial \boldsymbol{U}}{\partial x}\bigg|^{n} + \boldsymbol{B}^2\frac{\partial \boldsymbol{U}}{\partial y}\bigg|^{n}\right)\right] \quad (4.1)\end{aligned}$$

Due to the similarity of the equations in each step of the TG3-2S scheme to the TG2 form, as noted in the previous chapter, unnecessary repetition is avoided and the TG3-2S form of the discretised equations is not derived here.

4.4 Spectral DG Formulation on Triangular Elements

4.4.1 Discretised Equations

Contrary to the continuous Gakerkin procedure encountered in standard finite element formulations, and also in the spectral element method introduced in Chapter 3, where the variational statement is taken over the entire domain, the DG method formulates an expression over individual elements. The resulting discretised equations are similar to those presented in Section 3.5, the difference being that the integrals are computed locally, over single elements. Therefore, we can express the weighted residual of (4.1) for an arbitrary element e as

$$\begin{aligned}\int_{\Omega^e} N_I \Delta\hat{\boldsymbol{U}}\, d\Omega = -\Delta t \int_{\Omega^e} N_I\left(\boldsymbol{A}\frac{\partial \hat{\boldsymbol{U}}}{\partial x}\bigg|^{n} + \boldsymbol{B}\frac{\partial \hat{\boldsymbol{U}}}{\partial y}\bigg|^{n}\right) d\Omega \\ +\frac{\Delta t^2}{2}\int_{\Omega^e} N_I\left(\boldsymbol{A}^2\frac{\partial^2 \hat{\boldsymbol{U}}}{\partial x^2}\bigg|^{n} + \boldsymbol{AB}\frac{\partial^2 \hat{\boldsymbol{U}}}{\partial x\partial y}\bigg|^{n} + \boldsymbol{BA}\frac{\partial^2 \hat{\boldsymbol{U}}}{\partial x\partial y}\bigg|^{n} + \boldsymbol{B}^2\frac{\partial^2 \hat{\boldsymbol{U}}}{\partial y^2}\bigg|^{n}\right) d\Omega \quad (4.2)\end{aligned}$$

As before, the terms of the full weighted residual statement, over both the domain Ω and domain boundary Γ, will simplify when integration by parts and Green's lemma are applied, giving

$$\begin{aligned}
\int_{\Omega^e} N_I \Delta \hat{\boldsymbol{U}}\, d\Omega \;=\; & \Delta t \int_{\Omega^e} \left(\boldsymbol{A} \hat{\boldsymbol{U}} \frac{\partial N_I}{\partial x}\bigg|^n + \boldsymbol{B} \hat{\boldsymbol{U}} \frac{\partial N_I}{\partial y}\bigg|^n \right) d\Omega \\
& - \frac{\Delta t^2}{2} \int_{\Omega^e} \left(\boldsymbol{A}^2 \frac{\partial N_I}{\partial x} \frac{\partial \hat{\boldsymbol{U}}}{\partial x}\bigg|^n + \boldsymbol{A}\boldsymbol{B} \frac{\partial N_I}{\partial x} \frac{\partial \hat{\boldsymbol{U}}}{\partial y}\bigg|^n \right. \\
& \left. + \boldsymbol{B}\boldsymbol{A} \frac{\partial N_I}{\partial y} \frac{\partial \hat{\boldsymbol{U}}}{\partial x}\bigg|^n + \boldsymbol{B}^2 \frac{\partial N_I}{\partial y} \frac{\partial \hat{\boldsymbol{U}}}{\partial y}\bigg|^n \right) d\Omega \\
& - \Delta t \int_{\Gamma^e} \left(N_I \boldsymbol{f}^{n+\frac{1}{2}} \cdot \boldsymbol{n} \right) d\Gamma
\end{aligned}$$

Subsequently, inserting the finite element approximation of the unknown distribution

$$\hat{\boldsymbol{U}} = N_J \boldsymbol{U}_J$$

we obtain the fully discretised form of the equations

$$M_{IJ} \Delta \boldsymbol{U}_J = \Delta t C_{IJ} \boldsymbol{U}_J^n - \frac{\Delta t^2}{2} K_{IJ} \boldsymbol{U}_J^n + \Delta t f_I \tag{4.3}$$

where

$$\begin{aligned}
M_{IJ} &= \int_{\Omega^e} N_I N_J \, d\Omega \\
C_{IJ} &= \int_{\Omega^e} \left(\boldsymbol{A} \frac{\partial N_I}{\partial x} N_J + \boldsymbol{B} \frac{\partial N_I}{\partial y} N_J \right) d\Omega \\
K_{IJ} &= \int_{\Omega^e} \left(\boldsymbol{A}^2 \frac{\partial N_I}{\partial x} \frac{\partial N_J}{\partial x} + \boldsymbol{A}\boldsymbol{B} \frac{\partial N_I}{\partial x} \frac{\partial N_J}{\partial y} \right. \\
& \qquad \left. + \boldsymbol{B}\boldsymbol{A} \frac{\partial N_I}{\partial y} \frac{\partial N_J}{\partial x} + \boldsymbol{B}^2 \frac{\partial N_I}{\partial y} \frac{\partial N_J}{\partial y} \right) d\Omega \\
f_I &= -\Delta t \int_{\Gamma^e} N_I \hat{\boldsymbol{f}}^{n+\frac{1}{2}} \boldsymbol{n} \, d\Gamma - \Delta t \int_{\Gamma^e_{PROP}} N_I \boldsymbol{f}^{n+\frac{1}{2}} \boldsymbol{n} \, d\Gamma \\
& \qquad - \Delta t \int_{\Gamma^e_{ABC}} N_I \boldsymbol{f}^{n+\frac{1}{2}} \boldsymbol{n} \, d\Gamma
\end{aligned}$$

Note, as before, the boundary integrals have been simplified and expressed as fluxes f computed at the half-step $n + 1/2$, and that Γ_{PROP} and Γ_{ABC} denote the sections of the boundaries where the test propagation condition and the absorbing boundary condition will be applied.

4.4.2 Numerical Flux

Due to the local element nature of the discontinuous Galerkin schemes, communication between neighbouring elements occurs by means of consistent numerical fluxes. Various types of numerical fluxes exist. In this work, the Roe flux is used [50]. As introduced in Chapter 3 with regard to the formulation of a first order upwind absorbing boundary condition (ABC), a Roe flux resolved normally to the boundary can be written as

$$\boldsymbol{f}_{Roe} = \frac{1}{2}\left\{\boldsymbol{f}_n^L + \boldsymbol{f}_n^R - |\boldsymbol{A}_n|(\boldsymbol{U}^R - \boldsymbol{U}^L)\right\} \tag{4.4}$$

In this expression, $\boldsymbol{f}_n^L$ and $\boldsymbol{f}_n^R$ represent the normal flux vectors, $\boldsymbol{U}^L$ and $\boldsymbol{U}^R$ represent the unknown solution vectors, with superscripts L and R indicating values from the left and right of the boundary respectively, and $\boldsymbol{A}_n$ is the normal Jacobian matrix of the governing equation system as introduced in Section 3.7. Evaluation of the magnitude of the normal Jacobian matrix $|\boldsymbol{A}_n|$ proceeds as shown in this previous section. Subsequently, the complete form of the Roe flux required for the DG discretisation of the governing acoustic equations is expressed as

$$\boldsymbol{f}_{Roe} = \frac{1}{2}\left(n_x \begin{Bmatrix} p^L + p^R \\ 0 \\ u^L + u^R \end{Bmatrix} + n_y \begin{Bmatrix} 0 \\ p^L + p^R \\ v^L + v^R \end{Bmatrix} - \begin{bmatrix} n_x^2 & n_x n_y & 0 \\ n_x n_y & n_y^2 & 0 \\ 0 & 0 & 1 \end{bmatrix} \begin{Bmatrix} u^R - u^L \\ v^R - v^L \\ p^R - p^L \end{Bmatrix} \right)$$

This numerical flux can now be substituted into the discretised equations (4.3), giving

$$M_{IJ}\Delta \boldsymbol{U}_J = \Delta t C_{IJ} \boldsymbol{U}_J - \frac{\Delta t^2}{2} K_{IJ} \boldsymbol{U}_J + \Delta t f_I \tag{4.5}$$

where

$$\begin{aligned}
M_{IJ} &= \int_{\Omega^e} N_I N_J \, d\Omega \\
C_{IJ} &= \int_{\Omega^e} (\boldsymbol{A}\frac{\partial N_I}{\partial x} N_J + \boldsymbol{B}\frac{\partial N_I}{\partial y} N_J) \, d\Omega \\
K_{IJ} &= \int_{\Omega^e} \left(\boldsymbol{A}^2 \frac{\partial N_I}{\partial x}\frac{\partial N_J}{\partial x} + \boldsymbol{A}\boldsymbol{B}\frac{\partial N_I}{\partial x}\frac{\partial N_J}{\partial y} \right. \\
& \qquad \left. + \boldsymbol{B}\boldsymbol{A}\frac{\partial N_I}{\partial y}\frac{\partial N_J}{\partial x} + \boldsymbol{B}^2 \frac{\partial N_I}{\partial y}\frac{\partial N_J}{\partial y} \right) d\Omega \\
f_I &= -\Delta t \int_{\Gamma^e} \boldsymbol{f}_{Roe}^{n+\frac{1}{2}} \boldsymbol{n} \, d\Gamma - \Delta t \int_{\Gamma^e_{PROP}} \boldsymbol{f}^{n+\frac{1}{2}} \boldsymbol{n} \, d\Gamma - \Delta t \int_{\Gamma^e_{ABC}} \boldsymbol{f}^{n+\frac{1}{2}} \boldsymbol{n} \, d\Gamma
\end{aligned}$$

Note that the numerical fluxes must be computed at the midpoint of the time-step to ensure the correct application of the TG2 scheme. This is due to the application of intergration-by-parts to both the first and second order spatial derivative terms of (4.2). In practice, these half-step values are computed from the current known values of the variables at time-step n using the truncated Taylor series expansion

$$\boldsymbol{U}^{n+\frac{1}{2}} = \boldsymbol{U}^n + \frac{\Delta t}{2}\frac{\partial \boldsymbol{U}}{\partial t}\bigg|^n \tag{4.6}$$

which, upon substitution of the governing equation (3.19), becomes

$$\boldsymbol{U}^{n+\frac{1}{2}} = \boldsymbol{U}^n - \frac{\Delta t}{2}\left(\frac{\partial \boldsymbol{F}}{\partial x} + \frac{\partial \boldsymbol{G}}{\partial y}\right)\bigg|^n \tag{4.7}$$

4.5 Convergence Analysis

A convergence analysis will be performed with the DG method, similar to the previous chapter for the quadrilateral implementation of the SEM, using corresponding meshes of structured triangular elements, generated by dividing each quadrilateral element into two triangular elements.

4.5.1 Computational Model

Details of the computational model used for this convergence analysis can be found in Section 3.9. The meshes were obtained by simply dividing each element of the previously used quadrilateral meshes diagonally into two triangular elements. The corresponding structured triangular mesh to that presented in Figure 3.7 can be seen in Figure 4.2 Note the single column of quadrilateral elements on the downstream boundary of the domain to which the first order ABC is applied.

A L^2-error norm (3.42), taken along the horizontal centre-line of the mesh, will be used to assess the accuracy of the approximation.

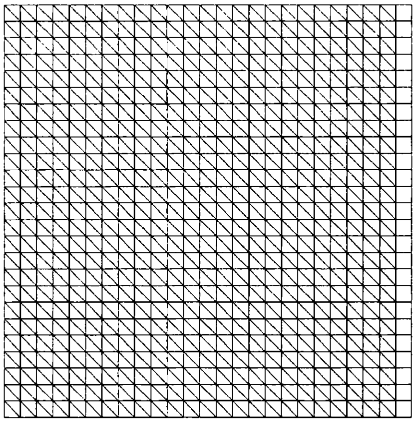

Figure 4.2: Coarse mesh (25x25) for convergence analysis

4.5.2 Results

As seen previously for the SEM applied to quadrilateral elements, p-convergence is evident in the results obtained using the TG2 time-stepping scheme displayed in Figure 4.3. However, the convergence limit due to the lower temporal accuracy of the TG2 scheme is even more defined in this case.

Application of the TG3-2S scheme reduces the effect of this limit , as can be seen in Figure 4.4. However, contrary to the SEM method of the previous chapter, although now sufficiently accurate to permit convergence for the 100×100 mesh, continuation of p-convergence for the most refined mesh is still disabled.

Ultimately, turning to the fourth order accurate RK4 scheme, we see from Figure 4.5 that by application of this method the limit is completely removed and p-convergence is clear for every mesh.

4.6 Conclusion

An alternative solution method for application to triangular elements has been implemented and tested. This DG formulation demonstrated the potential for exponential p-convergence when applied to the simple example of Gaussian pulse propagation

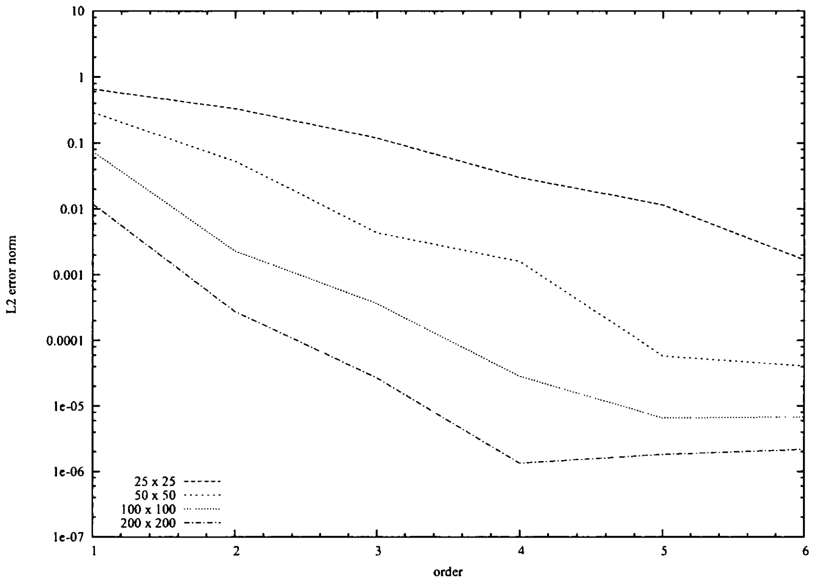

Figure 4.3: p-Convergence results for the DG method with varying mesh refinement using a TG2 scheme

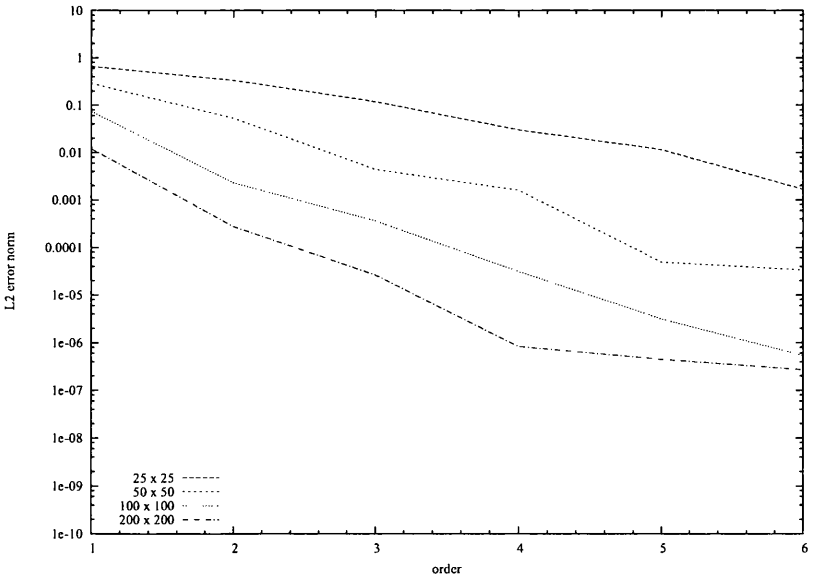

Figure 4.4: p-Convergence results for the DG method with varying mesh refinement using a TG3-2S scheme

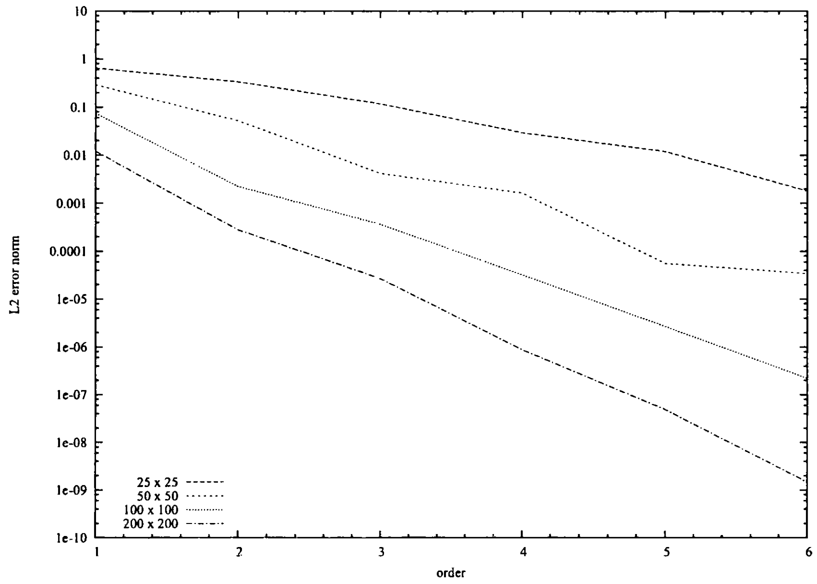

Figure 4.5: p-Convergence results for the DG method with varying mesh refinement using a RK4 scheme

through an open domain.

Therefore, suitable solution methods have now been obtained for both the quadrilateral and triangular parts of the proposed hybrid mesh. We may now proceed to amalgamate these procedures in an attempt to obtain a suitable method to model practical wave scattering problems.

Chapter 5

Hybrid SEM/DG Method

5.1 Introduction

The requirements of practical wave scattering problems can be separated into two sets of conflicting statements. On one hand, the models require the ability to resolve intricate scattering geometries and to permit the accurate approximation of wave forms over several cycles. However, due to the complexity of the problems and finite computational resources, these models must be sufficiently efficient to obtain the required results within a reasonable timescale.

Consequently, following the reasoning of Section 3.1.1, the use of a hybrid mesh of both quadrilateral and triangular elements was proposed. The motivation for this was the inherent nature of the wave scattering problems considered in this work. In these problems the main area of complexity within the computational domain is located in the vicinity of the scattering object. Beyond this is a vast area of open space.

Within the last two chapters, alternative computational procedures for the respective parts of the mesh have been introduced and analysed. Separately, these procedures were shown to permit exponential p-convergence for a simple propagation problem. To achieve our objective of a hybrid solution procedure, we must now attempt to couple these solution techniques.

As a matter of consistency, the description of the formulation for this hybrid method will be followed by the Gaussian pulse convergence analysis employed in Chapters 3 and 4. This is the first step in the development of the procedure: ensuring that exponential convergence is still attainable on a simple hybrid mesh. Only when this has been verified can we turn our attention to matters more pertinent to wave scattering problems.

Verification of the hybrid solution procedure for wave scattering problems will be performed by comparison of the computational approximation to an exact analytical solution. However, before we can perform this test, some limitations of the current computational model must be addressed. These include the approximation of an infinite domain at the outer artificial boundary and the ability of the model to resolve curved scattering geometries.

Once complete, we will be well placed to begin analysing various other scattering models for which exact analytical solutions are unavailable. Obviously, it is the scattered wave fields and associated quantities that can be extracted from the data for these scatterers which is of most interest to practising scientists and engineers.

5.2 Hybrid SEM/DG Formulation

The use of the procedures discussed in the previous chapters has been explained and justified by reasoning and preliminary analysis. As separate methods, they have been shown to work effectively and demonstrate the potential for exponential convergence.

Application of these procedures to the appropriate parts of a hybrid mesh is now required to further the development of the proposed solution method.

5.2.1 Hybrid Mesh

The nature of typical wave scattering model domains lend themselves towards refinement by means of a hybrid mesh. Usually, the scattering object of interest is located within the centre of the domain, surrounded by vast open space. Therefore, assuming that the scattering geometry is sufficiently complex to warrant discretisation by an unstructured triangular mesh, it would be considered highly inefficient to employ such a technique to discretise the entire domain. The outer open regions would be discretised much more efficiently with a structured Cartesian grid of quadrilateral elements.

Consequently, at some distance from the scattering surface, an interface could be placed between the inner unstructured triangular mesh and the outer structured quadrilateral mesh. In practice, to ease the computational burden, this interface would also preferably be placed as close as possible to the scattering surface. An illustration of a general hybrid mesh for wave scattering problems is shown in Figure 5.1.

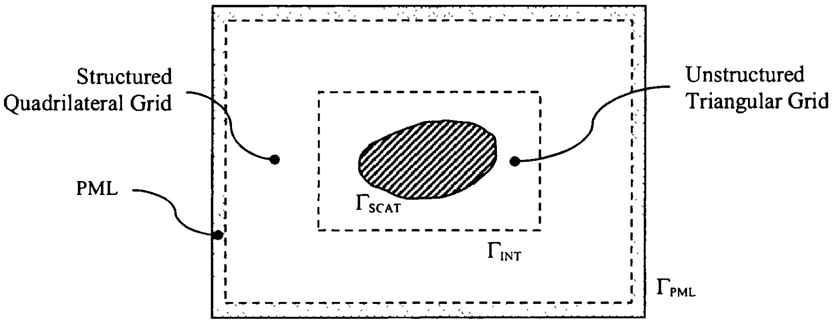

Figure 5.1: General hybrid mesh for wave scattering models

5.2.2 Mesh Generation

The mesh is generated in two phases. Firstly, a simple structured quadrilateral grid is generated, the size of which must be sufficient to accommodate the proposed scattering object. Once complete, this mesh is compared with the points constituting the surface of the scatterer. The area of the structured mesh to which these points extend is then enlarged, the degree of which can be controlled by the user, and it is the outer boundary of this area that will become the quadrilateral-triangular interface Γ_{Int} of the hybrid mesh shown in Figure 5.1. Beyond this interface, the remainder of the structured quadrilateral grid is saved to file.

Secondly, within the interface, between it and the surface of the scattering object, an unstructured triangular mesh is generated between the two boundaries. A Delaunay advancing front unstructured mesh generator is used [51]. Subsequently, following some renumbering of points, elements, sides and boundaries to ensure correspondence, both parts of the hybrid mesh can be coupled within the same file.

5.2.3 Discretised Equations

Different numerical schemes will be applied to the separate parts of the mesh: a spectral element method (SEM) on the quadrilateral part and a spectral discontinuous Galerkin method (DGM) on the triangular part of the mesh. The discretised equations for these schemes will be identical to those introduced in the previous chapters but for ease of reference are rewritten below. Subsequently, the choice of a simple coupling method, used to enable communication between these respective parts of the domain, will be presented and explained.

SEM Component of the Hybrid Method

For the SEM, the fully discretised equations (3.27), written here for the second order Taylor Galerkin (TG2) temporal scheme, can be expressed as

$$M_{IJ}\Delta\boldsymbol{U}_J = \Delta t C_{IJ}\boldsymbol{U}_J^n - \frac{\Delta t^2}{2}K_{IJ}\boldsymbol{U}_J^n + \Delta t f_I \tag{5.1}$$

where

$$\begin{aligned}
M_{IJ} &= \int_{\Omega_{SEM}} P_I Q_I P_J Q_J \, d\Omega \\
C_{IJ} &= \int_{\Omega_{SEM}} (\boldsymbol{A}\frac{dP_I}{dx}Q_I P_J Q_J + \boldsymbol{B}P_I\frac{dQ_I}{dy}P_J Q_J)\, d\Omega \\
K_{IJ} &= \int_{\Omega_{SEM}} \left(\boldsymbol{A}^2\frac{dP_I}{dx}Q_I\frac{dP_J}{dx}Q_J + \boldsymbol{AB}\frac{dP_I}{dx}Q_I P_J\frac{dQ_J}{dy}\right. \\
&\qquad \left. + \boldsymbol{BA}P_I\frac{dQ_I}{dy}\frac{dP_J}{dx}Q_J + \boldsymbol{B}^2 P_I\frac{dQ_I}{dy}P_J\frac{dQ_J}{dy}\right) d\Omega \\
f_I &= -\Delta t \int_{\Gamma^e_{INT}} N_I \boldsymbol{f}^{n+\frac{1}{2}}\boldsymbol{n}\, d\Gamma \; - \; \Delta t \int_{\Gamma^e_{PML}} N_I \boldsymbol{f}^{n+\frac{1}{2}}\boldsymbol{n}\, d\Gamma
\end{aligned}$$

and Γ_{INT} and Γ_{PML} denote the boundaries of the structured quadrilateral part of the domain, namely the mesh interface and outer boundary beyond the PML respectively.

It is worth noting at this stage, once again, that the global mass matrix $\boldsymbol{M}$ formed on the quadrilateral part of the mesh will be diagonal, thus simplifying the inversion process and facilitating significant computational savings.

Spectral DGM Component of the Hybrid Method

The discretised equations for the spectral DGM, again written for the TG2 scheme, are expressed as (4.3)

$$M_{IJ}\Delta\boldsymbol{U}_J = \Delta t C_{IJ}\boldsymbol{U}_J^n - \frac{\Delta t^2}{2}K_{IJ}\boldsymbol{U}_J^n + \Delta t f_I \tag{5.2}$$

where

$$\begin{aligned}
M_{IJ} &= \int_{\Omega_{DG}^e} N_I N_J \, d\Omega \\
C_{IJ} &= \int_{\Omega_{DG}^e} (\boldsymbol{A}\frac{\partial N_I}{\partial x}N_J + \boldsymbol{B}\frac{\partial N_I}{\partial y}N_J)\, d\Omega \\
K_{IJ} &= \int_{\Omega_{DG}^e} \Bigg(\boldsymbol{A}^2\frac{\partial N_I}{\partial x}\frac{\partial N_J}{\partial x} + \boldsymbol{AB}\frac{\partial N_I}{\partial x}\frac{\partial N_J}{\partial y} \\
&\qquad + \boldsymbol{BA}\frac{\partial N_I}{\partial y}\frac{\partial N_J}{\partial x} + \boldsymbol{B}^2\frac{\partial N_I}{\partial y}\frac{\partial N_J}{\partial y}\Bigg) d\Omega \\
f_I &= -\Delta t\int_{\Gamma^e} N_I \boldsymbol{f}_{Roe}^{n+\frac{1}{2}}\boldsymbol{n}\, d\Gamma - \Delta t\int_{\Gamma_{SCAT}^e} N_I \boldsymbol{f}^{n+\frac{1}{2}}\boldsymbol{n}\, d\Gamma \\
&\qquad - \Delta t\int_{\Gamma_{INT}^e} N_I \boldsymbol{f}^{n+\frac{1}{2}}\boldsymbol{n}\, d\Gamma
\end{aligned}$$

and Γ_{SCAT} and Γ_{INT} denote the boundaries of the unstructured triangular part of the domain, namely the scattering surface and mesh interface respectively.

In this case, the mass matrix $\boldsymbol{M}$ will not be diagonal. However, due to the nature of the DGM, its formation will be local, over each discrete element e, meaning inversion of a large global mass matrix is again avoided.

5.2.4 Interface Coupling Method

A method to enable communication between the separate parts of the mesh is now required. To maintain as simplified a formulation as possible, the Roe flux (4.4) introduced for the numerical flux calculation in the DGM will be used.

$$\boldsymbol{f}_n^{Roe} = \frac{1}{2}\left\{\boldsymbol{f}_n^L + \boldsymbol{f}_n^R - |\boldsymbol{A}_n|(\boldsymbol{U}^R - \boldsymbol{U}^L)\right\} \tag{5.3}$$

This will impose a Neumann flux type boundary condition to the quadrilateral part of the mesh.

5.2.5 Scattering Boundary Condition

Hard Acoustic Scatterer

The scattering boundary condition for a hard acoustic scatterer is that the normal gradient of the pressure at the scattering surface be zero

$$\left.\frac{\partial p^t}{\partial n}\right|_{\Gamma_{hard}} = 0 \tag{5.4}$$

and that the normal velocity be zero

$$\boldsymbol{v}^t \cdot \boldsymbol{n}|_{\Gamma_{hard}} = 0 \tag{5.5}$$

where the superscript t emphasises the fact that here we consider total values.

As discussed in Section 2.4, the linearity of the equations enable the solution to be separated into its incident and scattered component. Consequently, as we solve the discretised equations for the scattered component only, the boundary conditions must also be defined in terms of the scattered field. Therefore, using expression (2.12), we can express condition (5.5) for the total field in terms of the scattered and incident wave components as

$$\boldsymbol{v}^s \cdot \boldsymbol{n}|_{\Gamma_{hard}} = -\boldsymbol{v}^i \cdot \boldsymbol{n}|_{\Gamma_{hard}} \tag{5.6}$$

where the superscripts i and s denote the incident and scattered components respectively. For a two dimensional problem where the incident wave field is assumed to be a plane sinusoidal pressure wave of the form

$$p^i(x, y, t) = p_0 \cos(k_x x + k_y y - \omega t) \tag{5.7}$$

then the incident velocity $\boldsymbol{v}^i$ can be evaluated from the governing acoustic equations (3.19) to be

$$u^i = \frac{k_x p_0}{\omega} \sin(k_x x + k_y y - \omega t) \tag{5.8a}$$

$$v^i = \frac{k_y p_0}{\omega} \sin(k_x x + k_y y - \omega t) \tag{5.8b}$$

where $\boldsymbol{k} = (k_x, k_y)$ is the wavenumber and ω is the angular frequency of the wave.

Note that for electromagnetic applications, the boundary condition for the analogous transverse electric (TE^z) polarization, as discussed in Section 2.5.5, can be obtained in a similar manner.

Soft Acoustic Scatterer

The scattering boundary condition for a soft acoustic scatterer is that the pressure be zero at the scattering surface

$$p^t|_{\Gamma_{soft}} = 0 \tag{5.9}$$

and that the tangential component of the velocity be zero

$$\boldsymbol{v}^t \times \boldsymbol{n}|_{\Gamma_{soft}} = 0 \tag{5.10}$$

where the superscript t emphasises the fact that here we consider total values.

Again, the linearity of the equations can be used to express condition (5.10) using the scattered and incident components as

$$\boldsymbol{v}^s \times \boldsymbol{n}|_{\Gamma_{soft}} = -\boldsymbol{v}^i \times \boldsymbol{n}|_{\Gamma_{soft}} \tag{5.11}$$

Equations (5.8a) and (5.8b) can now be used to apply the required form of the boundary condition for the specified incident wave field.

Once more, note that the boundary conditions for the analogous electromagnetic model of a transverse magnetic (TM^z) polarized problem would be applied similarly.

5.3 Convergence Analysis

As a final assessment before attempting to apply the method to the solution of wave scattering problems, p-convergence of this hybrid method will be validated in the same manner as seen previously in Chapters 3 and 4.

5.3.1 Computational Model

The reader is referred to Section 3.9 for details of the simple Gaussian pulse model used in this analysis. The hybrid meshes are formed simply by combining the meshes of corresponding levels of refinement used in the previous tests. The quadrilateral-triangular interface is located halfway along the x-dimension of the domain. A typical example can be seen in Figure 5.2.

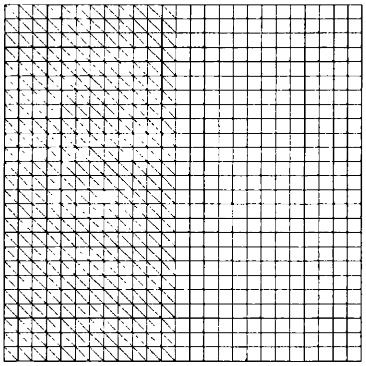

Figure 5.2: Coarse mesh (25x25) for convergence analysis

With this arrangement, the Gaussian pulse is set to propagate through the interface from the triangular to the quadrilateral part of the mesh. Therefore, this provides an adequate means by which to assess the efficacy of the chosen coupling technique.

As before, a L^2-error norm (3.42), taken along the horizontal centre-line of the mesh, will be used to assess the accuracy of the approximation.

5.3.2 Results

A similar trend is evident as witnessed in the previous convergence analyses. With the TG2 scheme, the results shown in Figure 5.3 demonstrate p-convergence for the coarser meshes. However, with further h-refinement of the mesh, a limit of convergence is seen and the accuracy of the approximate solutions fails to improve at the desired rate beyond this point.

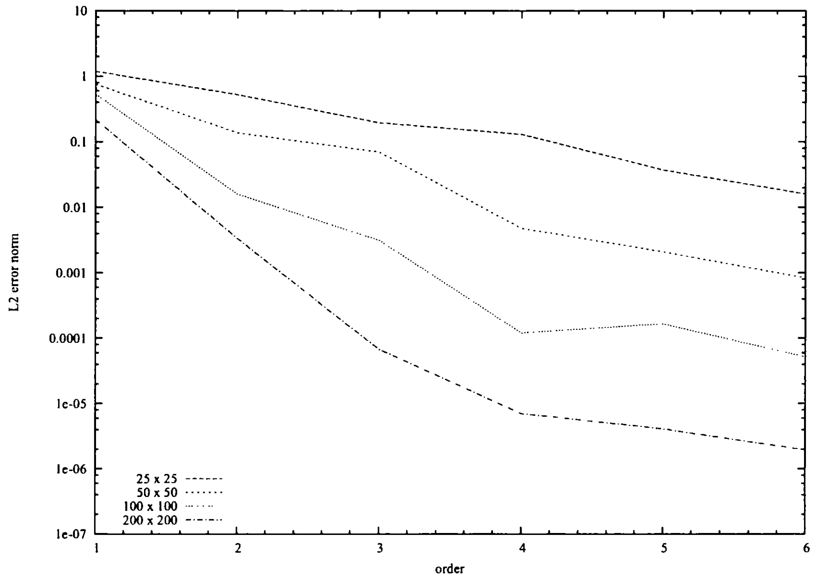

Figure 5.3: p-Convergence results for the hybrid method with varying mesh refinement using a TG2 scheme

We see that the application of the higher order TG3-2S scheme extends the convergence trend, shown in Figure 5.4. However, as seen in Chapter 4, the results presented in Figure 5.5 confirm that the fourth order RK4 scheme is needed to permit convergence of the solution on all of the meshes of various refinement used for this particular model.

With these results, the hybrid method has demonstrated the potential for p-convergence. Therefore, the method's development for the solution of wave scattering problems can commence.

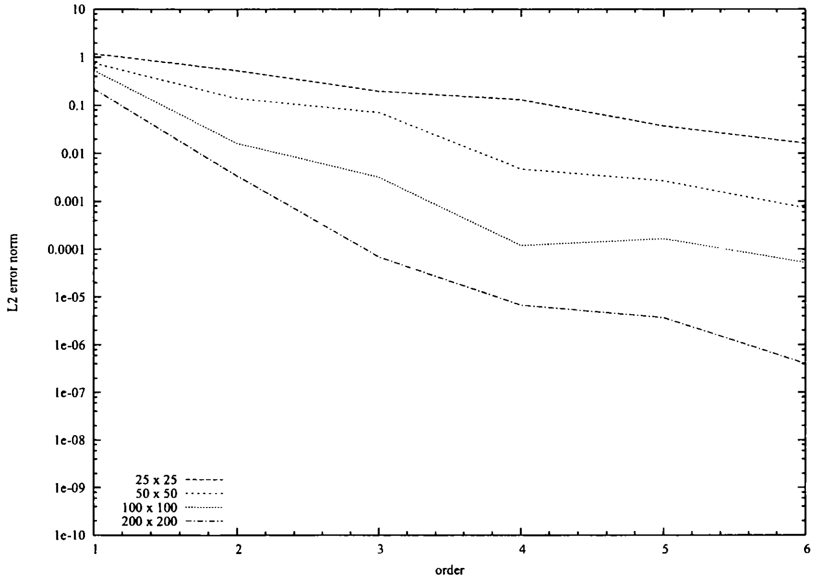

Figure 5.4: p-Convergence results for the hybrid method with varying mesh refinement using a TG3-2S scheme

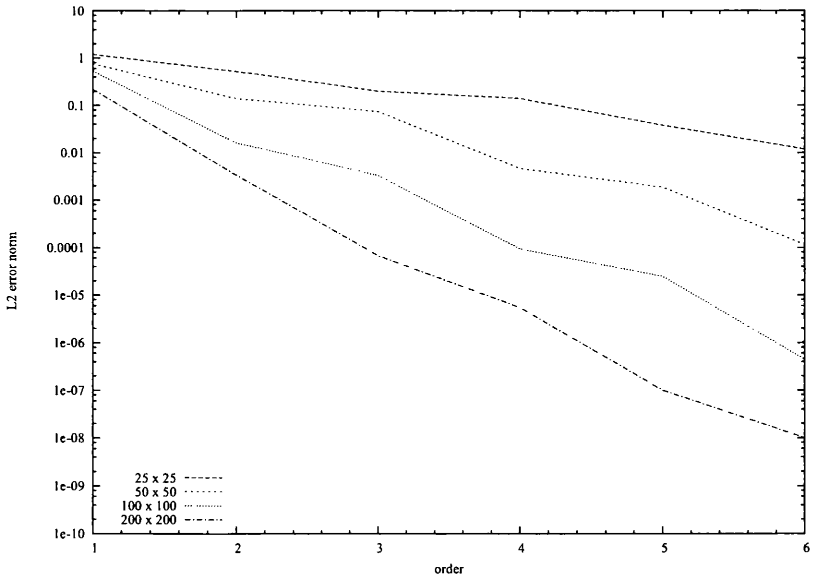

Figure 5.5: p-Convergence results for the hybrid method with varying mesh refinement using a RK4 scheme

5.4 Perfectly Matched Layers

5.4.1 Introduction

An important feature that may limit the accuracy of any open space scattering simulation is the method used to truncate the physical domain. Previous work involving the initial development of a scattering solution procedure necessitated only a simple first order absorbing boundary condition. However, at this stage, as we attempt to refine our hybrid method, we must ensure that any possible sources of error are minimised.

Therefore, we turn our attention to a popular domain truncation method, first devised by Berenger [26], which incorporates sections of the domain referred to as perfectly matched layers (PML).

5.4.2 Governing Equations

The governing equations for the PML region of the domain are an augmented form of the standard acoustic equations (3.19) with an additional source term vector [27]

$$\frac{\partial \boldsymbol{U}}{\partial t} + \frac{\partial \boldsymbol{F}}{\partial x} + \frac{\partial \boldsymbol{G}}{\partial y} + \boldsymbol{S} = 0 \tag{5.12}$$

where

$$\boldsymbol{U} = \begin{bmatrix} u \\ v \\ p \\ q \end{bmatrix} \qquad \boldsymbol{F} = \begin{bmatrix} p \\ 0 \\ u \\ 0 \end{bmatrix} \qquad \boldsymbol{G} = \begin{bmatrix} 0 \\ p \\ v \\ v \end{bmatrix} \qquad \boldsymbol{S} = \begin{bmatrix} \sigma_x u \\ \sigma_y v \\ \sigma_x p + (\sigma_y - \sigma_x) q \\ \sigma_y q \end{bmatrix}$$

Here q is an auxiliary variable and σ_x and σ_y are the PML damping parameters in the x and y directions respectively.

5.4.3 Temporal Discretisation

Beginning with a truncated Taylor series expansion to second order

$$\Delta \boldsymbol{U} = \Delta t \frac{\partial \boldsymbol{U}}{\partial t}\bigg|^{n} + \frac{\Delta t^2}{2}\frac{\partial^2 \boldsymbol{U}}{\partial t^2}\bigg|^{n} \tag{5.13}$$

we can now substitute the governing equation for the PML (5.12) for the temporal derivatives, giving

$$\Delta \boldsymbol{U} = -\Delta t \left\{ \frac{\partial \boldsymbol{F}}{\partial x}\bigg|^{n} + \frac{\partial \boldsymbol{G}}{\partial y}\bigg|^{n} + \boldsymbol{S}^n \right\} - \frac{\Delta t^2}{2}\frac{\partial}{\partial t}\left\{ \frac{\partial \boldsymbol{F}}{\partial x}\bigg|^{n} + \frac{\partial \boldsymbol{G}}{\partial y}\bigg|^{n} + \boldsymbol{S}^n \right\} \tag{5.14}$$

As a temporal derivative is still present in the second order term, we must rearrange these derivatives to facilitate repetition of the substitution

$$\frac{\partial}{\partial t}\left(\frac{\partial \boldsymbol{F}}{\partial x}\right) = \frac{\partial}{\partial x}\left(\frac{\partial \boldsymbol{F}}{\partial \boldsymbol{U}}\frac{\partial \boldsymbol{U}}{\partial t}\right) = \frac{\partial}{\partial x}\left[-\boldsymbol{A}\left(\frac{\partial \boldsymbol{F}}{\partial x}\bigg|^{n} + \frac{\partial \boldsymbol{G}}{\partial y}\bigg|^{n} + \boldsymbol{S}^n\right)\right] \tag{5.15a}$$

$$\frac{\partial}{\partial t}\left(\frac{\partial \boldsymbol{G}}{\partial y}\right) = \frac{\partial}{\partial y}\left(\frac{\partial \boldsymbol{G}}{\partial \boldsymbol{U}}\frac{\partial \boldsymbol{U}}{\partial t}\right) = \frac{\partial}{\partial y}\left[-\boldsymbol{B}\left(\frac{\partial \boldsymbol{F}}{\partial x}\bigg|^{n} + \frac{\partial \boldsymbol{G}}{\partial y}\bigg|^{n} + \boldsymbol{S}^n\right)\right] \tag{5.15b}$$

$$\frac{\partial \boldsymbol{S}}{\partial t} = \frac{\partial \boldsymbol{S}}{\partial \boldsymbol{U}}\frac{\partial \boldsymbol{U}}{\partial t} = \boldsymbol{\sigma}\left[-\left(\frac{\partial \boldsymbol{F}}{\partial x}\bigg|^{n} + \frac{\partial \boldsymbol{G}}{\partial y}\bigg|^{n} + \boldsymbol{S}^n\right)\right] \tag{5.15c}$$

where $\boldsymbol{A} = \partial \boldsymbol{F}/\partial \boldsymbol{U}$, $\boldsymbol{B} = \partial \boldsymbol{G}/\partial \boldsymbol{U}$ and $\boldsymbol{\sigma} = \partial \boldsymbol{S}/\partial \boldsymbol{U}$ are the Jacobian matrices. Note also that the spatial derivatives of the fluxes can be expressed as $\partial \boldsymbol{F}/\partial x = \boldsymbol{A}\ (\partial \boldsymbol{U}/\partial x)$ and $\partial \boldsymbol{G}/\partial y = \boldsymbol{B}\ (\partial \boldsymbol{U}/\partial y)$ and the source term expressed as $\boldsymbol{S} = \boldsymbol{\sigma U}$. Following substitution of these expressions into (5.14), the resulting semi-discrete equations can be rearranged to clarify the standard acoustic part and the additional source terms responsible for the damping effect, written as

$$\begin{aligned}\Delta \boldsymbol{U} = &-\Delta t\left[\boldsymbol{A}\frac{\partial \boldsymbol{U}}{\partial x}\bigg|^{n} + \boldsymbol{B}\frac{\partial \boldsymbol{U}}{\partial y}\bigg|^{n}\right] \\ &+\frac{\Delta t^2}{2}\left[\frac{\partial}{\partial x}\left(\boldsymbol{A}^2\frac{\partial \boldsymbol{U}}{\partial x}\bigg|^{n} + \boldsymbol{AB}\frac{\partial \boldsymbol{U}}{\partial y}\bigg|^{n}\right) + \frac{\partial}{\partial y}\left(\boldsymbol{AB}\frac{\partial \boldsymbol{U}}{\partial x}\bigg|^{n} + \boldsymbol{B}^2\frac{\partial \boldsymbol{U}}{\partial y}\bigg|^{n}\right)\right] \\ &-\Delta t\boldsymbol{\sigma U}^n + \frac{\Delta t^2}{2}\boldsymbol{\sigma}\left[\boldsymbol{A}\frac{\partial \boldsymbol{U}}{\partial x}\bigg|^{n} + \boldsymbol{B}\frac{\partial \boldsymbol{U}}{\partial y}\bigg|^{n} + \boldsymbol{\sigma U}^n\right]\end{aligned} \tag{5.16}$$

5.4.4 SEM Formulation on Quadrilateral Elements

As the PML region will be situated at the outer boundary of the domain, we need only to obtain the SEM formulation of the equations for the quadrilateral elements. We can express the weighted residual of the governing equations for the PML region as

$$\begin{aligned}\int_\Omega N_I \Delta\hat{\boldsymbol{U}} = &-\Delta t \int_\Omega N_I \left(\boldsymbol{A}\frac{\partial \hat{\boldsymbol{U}}}{\partial x}\bigg|^n + \boldsymbol{B}\frac{\partial \hat{\boldsymbol{U}}}{\partial y}\bigg|^n \right) d\Omega \\ &+\frac{\Delta t^2}{2}\int_\Omega N_I \left(\boldsymbol{A}^2\frac{\partial^2 \hat{\boldsymbol{U}}}{\partial x^2}\bigg|^n + \boldsymbol{AB}\frac{\partial^2 \hat{\boldsymbol{U}}}{\partial x \partial y}\bigg|^n + \boldsymbol{BA}\frac{\partial^2 \hat{\boldsymbol{U}}}{\partial x \partial y}\bigg|^n + \boldsymbol{B}^2\frac{\partial^2 \hat{\boldsymbol{U}}}{\partial y^2}\bigg|^n \right) d\Omega \\ &-\Delta t \int_\Omega N_I \boldsymbol{\sigma} \hat{\boldsymbol{U}}^n + \frac{\Delta t^2}{2}\int_\Omega N_I \boldsymbol{\sigma} \left(\boldsymbol{A}\frac{\partial \hat{\boldsymbol{U}}}{\partial x}\bigg|^n + \boldsymbol{B}\frac{\partial \hat{\boldsymbol{U}}}{\partial y}\bigg|^n + \boldsymbol{\sigma}\boldsymbol{U}^n \right) d\Omega \end{aligned} \tag{5.17}$$

As conducted in the standard SEM formulation performed in Chapter 3, integration-by-parts is applied to the standard acoustic terms. However the additional source terms are not modified, giving

$$\begin{aligned}\int_\Omega N_I \Delta\hat{\boldsymbol{U}} \quad = \quad & \Delta t \int_\Omega \left(\boldsymbol{A}\hat{\boldsymbol{U}}\frac{\partial N_I}{\partial x}\bigg|^n + \boldsymbol{B}\hat{\boldsymbol{U}}\frac{\partial N_I}{\partial y}\bigg|^n \right) d\Omega \\ & -\frac{\Delta t^2}{2}\int_\Omega \left(\boldsymbol{A}^2\frac{\partial N_I}{\partial x}\frac{\partial \hat{\boldsymbol{U}}}{\partial x}\bigg|^n + \boldsymbol{AB}\frac{\partial N_I}{\partial x}\frac{\partial \hat{\boldsymbol{U}}}{\partial y}\bigg|^n \right. \\ & \qquad\qquad \left. +\boldsymbol{BA}\frac{\partial N_I}{\partial y}\frac{\partial \hat{\boldsymbol{U}}}{\partial x}\bigg|^n + \boldsymbol{B}^2\frac{\partial N_I}{\partial y}\frac{\partial \hat{\boldsymbol{U}}}{\partial y}\bigg|^n \right) d\Omega \\ & -\Delta t \int_\Omega N_I \boldsymbol{\sigma} \hat{\boldsymbol{U}}^n d\Omega + \frac{\Delta t^2}{2}\int_\Omega N_I \boldsymbol{\sigma} \left(\boldsymbol{A}\frac{\partial \hat{\boldsymbol{U}}}{\partial x}\bigg|^n + \boldsymbol{B}\frac{\partial \hat{\boldsymbol{U}}}{\partial y}\bigg|^n + \boldsymbol{\sigma}\boldsymbol{U}^n \right) d\Omega \\ & -\Delta t \int_\Gamma \left(N_I \boldsymbol{f}^{n+\frac{1}{2}} \cdot \boldsymbol{n} \right) d\Gamma \end{aligned} \tag{5.18}$$

Using a FE approximation of the unknowns, we express $\hat{\boldsymbol{U}}$ with a set of interpolation functions

$$\hat{\boldsymbol{U}} = N_J \boldsymbol{U}_J$$

and the fully discrete form of the equations can be written as

$$M_{IJ}\Delta\boldsymbol{U}_J = \Delta t C_{IJ}\boldsymbol{U}_J^n - \frac{\Delta t^2}{2}K_{IJ}\boldsymbol{U}_J^n + \Delta t D_{IJ}\boldsymbol{U}_J^n + \Delta t f_I \tag{5.19}$$

where

$$\begin{aligned}
M_{IJ} &= \int_\Omega P_I Q_I P_J Q_J \, d\Omega \\
C_{IJ} &= \int_\Omega (\boldsymbol{A} \frac{dP_I}{dx} Q_I P_J Q_J + \boldsymbol{B} P_I \frac{dQ_I}{dy} P_J Q_J) \, d\Omega \\
K_{IJ} &= \int_\Omega \left(\boldsymbol{A}^2 \frac{dP_I}{dx} Q_I \frac{dP_J}{dx} Q_J + \boldsymbol{AB} \frac{dP_I}{dx} Q_I P_J \frac{dQ_J}{dy} \right. \\
&\qquad \left. + \boldsymbol{BA} P_I \frac{dQ_I}{dy} \frac{dP_J}{dx} Q_J + \boldsymbol{B}^2 P_I \frac{dQ_I}{dy} P_J \frac{dQ_J}{dy} \right) d\Omega \\
D_{IJ} &= \int_\Omega \sigma P_I Q_I P_J Q_J \, d\Omega \\
&\qquad + \frac{\Delta t}{2} \int_\Omega \left(\sigma \boldsymbol{A} P_I Q_I \frac{dP_J}{dx} Q_J + \sigma \boldsymbol{B} P_I Q_I P_J \frac{dQ_J}{dy} + \sigma^2 P_I Q_I P_J Q_J \right) d\Omega \\
f_I &= -\Delta t \int_{\Gamma^e_{INT}} \boldsymbol{f}^{n+\frac{1}{2}} \boldsymbol{n} \, d\Gamma \; - \Delta t \int_{\Gamma^e_{PML}} \boldsymbol{f}^{n+\frac{1}{2}} \boldsymbol{n} \, d\Gamma
\end{aligned}$$

Note, again, that the boundary integral terms have been simplified and are represented by the boundary flux f.

The PML formulation was tested to assess the effect on its performance of varying some of the PML parameters, e.g. thickness, maximum damping coefficient. The results of this analysis can be seen in Appendix C.

5.5 Simple Circular Wave Scattering Model

Having reached a stage in the development where an initial scattering model can be attempted, an appropriately simple scattering object is required. The most obvious choice is a circular scatterer, which is both geometrically simple and, as discussed in Section 2.5, permits comparison with an analytical solution. Therefore, in this section, an initial scattering model will be introduced followed by the results obtained by our present higher order hybrid method applied to a straight-sided mesh.

5.5.1 Initial Scattering Model

This will be an acoustic wave model with linearised Euler governing equations as expressed in (3.19). In this example, a circular scatterer of 3 unit diameter will be placed at the centre of a square 10×10 unit domain. The mesh used to discretise this space comprises 76 triangular elements surrounding the scatterer and 68 quadrilateral elements beyond, as presented in Figure 5.6. The scatterer is illuminated by a plane incident sinusoidal pressure wave travelling along the x-axis, which can be expressed as

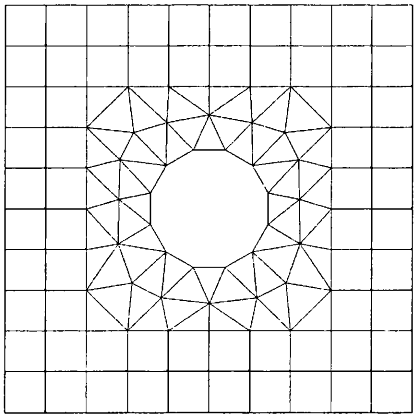

Figure 5.6: Simple circular scatterer mesh

$$p(\boldsymbol{x}, t) = p_0 \cos(k_x x - \omega t) \tag{5.20}$$

where $\boldsymbol{k} = (k_x, k_y)$ is the wavenumber and ω is the angular frequency of the wave. The wavenumber $\boldsymbol{k}$ relates to the wavelength λ as

$$\lambda = \frac{2\pi}{|\boldsymbol{k}|} \tag{5.21}$$

noting that, due to the null value given to k_y in this case, the denominator of this expression simplifies to merely k_x.

Returning briefly to the discussion of Section 2.5.5, concerning the analogy between the acoustic and electromagnetic (EM) equations in two dimensions, we note that this model, looking at both hard and soft acoustic scatterers, can be used to approximate transverse electric (TE^z) and transverse magnetic (TM^z) EM models of perfect electrically conducting (PEC) scatterers respectively, where interest is limited to the real parts of the wavefields. Therefore, in search of a simple initial problem, the wavelength is defined as $\lambda = 1.5$ units, thus giving an electrical length of 2λ for the scatterer when considering the problem in this context.

The model will be run for 6 cycles of the wave to ensure that the scattered wavefield has reached a fully developed steady harmonic state.

5.5.2 Results

The scattered wavefields produced for this model for the example of a hard acoustic scatterer using various element order are presented in Figure 5.7. Note that these figures also represent the scattered magnetic H^z field from a PEC in a TE^z polarizaed EM model. This provides an initial qualitative estimation of the improvement in solution accuracy as the order is increased, and suggests that the method is converging as desired.

However, the results displayed in Table 5.1 suggest otherwise. This table gives the L^2-error norm (3.42) of the pressure taken about the surface of the scatterer for this hard acoustic model, which provides a more quantitative measurement to assess the accuracy of the solution.

Order	TG2	RK4
1	0.65614525	0.53429377
2	0.34523503	0.36215839
3	0.12863426	0.12943203
4	0.14869759	0.14864206
5	0.15228255	0.15270437
6	0.14683943	0.14956536

Table 5.1: L^2-error norm of pressure taken around the scattering surface

We see here, that for both the TG2 and RK4 temporal schemes, that the convergence

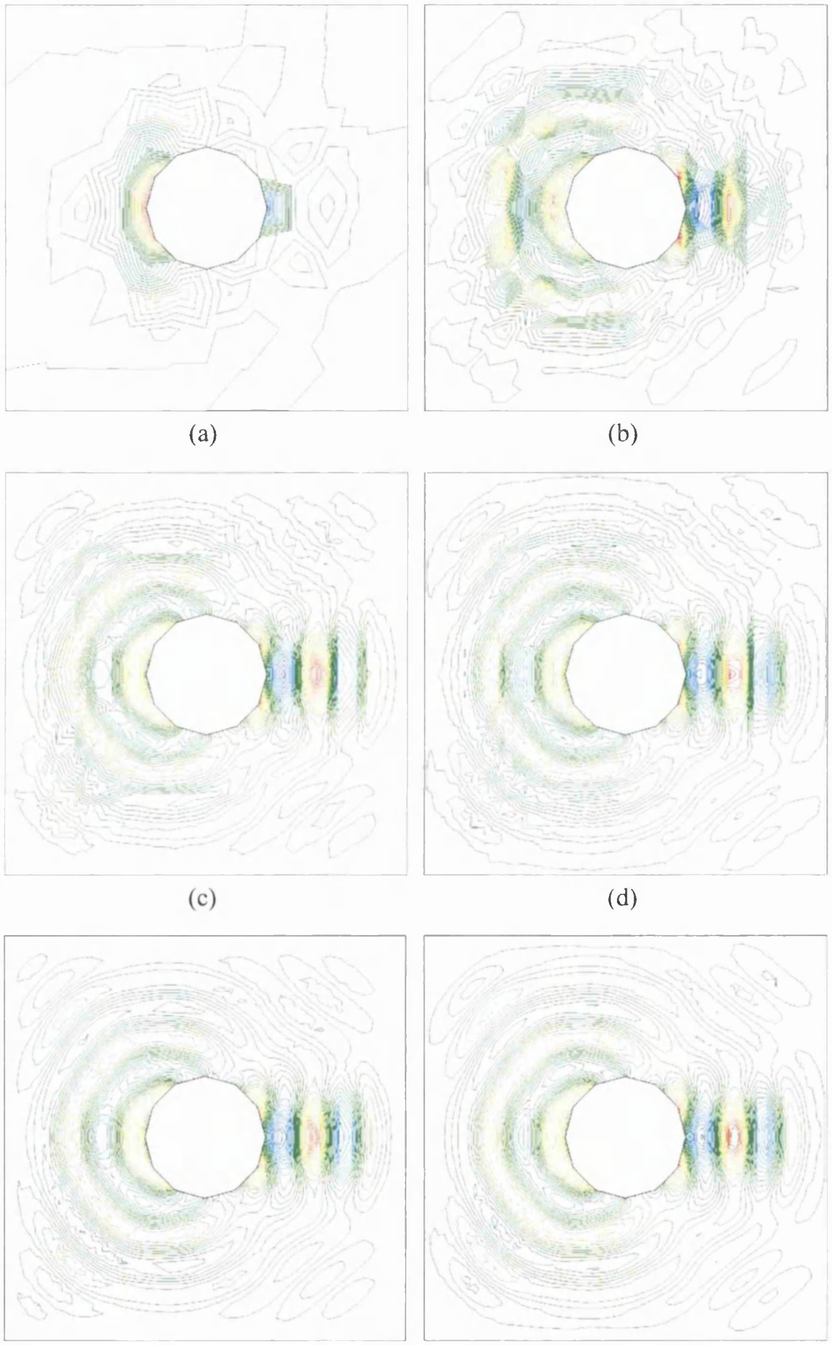

(a) (b) (c) (d) (e) (f)

Figure 5.7: Scattered field for various element order: (a) 1^{st} order (b) 2^{nd} order (c) 3^{rd} order (d) 4^{th} order (e) 5^{th} order (f) 6^{th} order

of the approximate solution is limited. In fact the accuracy fails to improve beyond that achieved with third order elements. As the limit is observed with even the higher order RK4 scheme, this indicates that there is some other source of error dominating the solution.

The most likely cause of this overriding error is the representation of the scattering geometry. With this initial example, it was attempted to model the boundary curve of the circular scatterer with a piecewise linear approximation. DG methods are known to be very sensitive to errors arising at curved boundaries [52]. Furthermore, it has been shown by Bassi and Rebay [32], that to maintain the order of accuracy of DG methods accurate representation of the boundary is needed. In [32], it is shown that even the accuracy of a DG scheme using linear interpolation functions for the approximation of the unknown can be improved significantly by the use of a quadratic representation of a boundary curve, which means that this is not only an important consideration for higher order solution schemes.

Examination of the scattering width distributions produced by this model, again for various element order as shown in Figure 5.8, provides further evidence supporting this fact. This is also evident for the case of a soft acoustic scatterer (or PEC scatterer in a TM^z polarized EM field) as shown in Figure 5.9. It is obvious that the approximations generated with increasing order fail to converge towards the exact analytical solution. In effect, they are converging towards the exact solution for a *dodecagon* or 12-sided polygon. Obviously, this example highlights this problem due to the use of a very coarse mesh. However, methods are available which can improve the approximation of curved boundaries, and hence the resulting solution, without resorting to an increase in h-refinement.

One method of improving the fidelity of boundary representation is to use higher order geometrical approximation. However, this is achieved by means of non-linear mapping which is inherently computationally expensive. Therefore, before turning to this method, we will attempt to implement a recent formulation developed by Krivodonova and Berger [33].

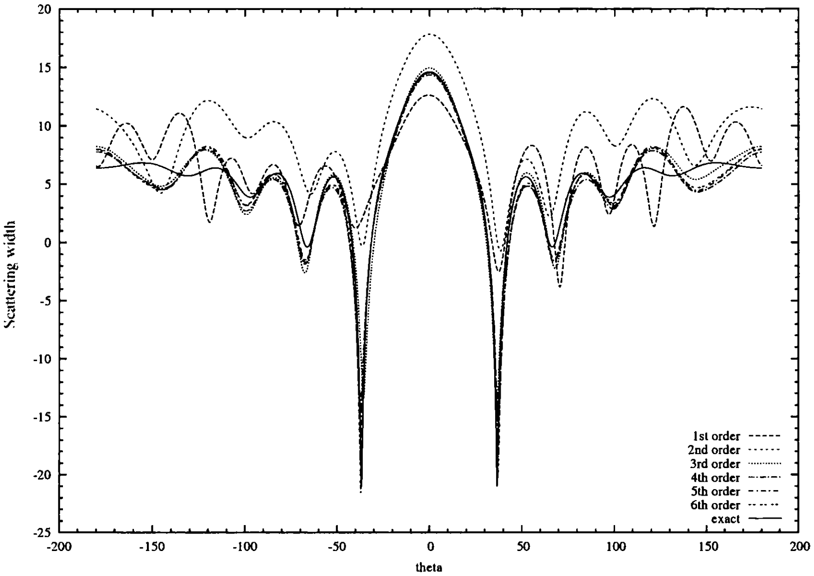

Figure 5.8: Computed scattering width distributions for a 2λ hard acoustic circular scatterer with various element order and straight mesh sides

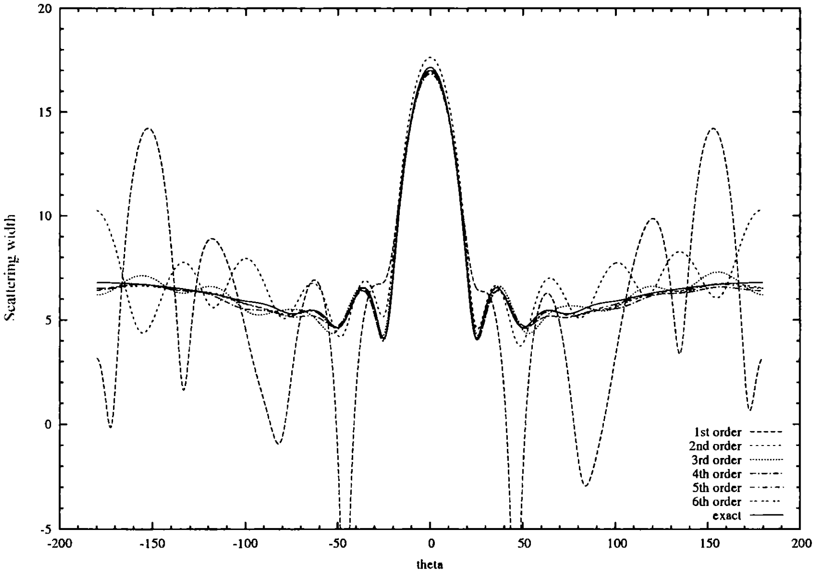

Figure 5.9: Computed scattering width distributions for a 2λ soft acoustic circular scatterer with various element order and straight mesh sides

5.6 Curvature Boundary Condition

This approach avoids the complexity of defining elements with curved geometrical boundaries, but succeeds in improving the resulting solution accuracy. Physically curved boundaries are discretised with standard straight-sided elements. However, calculations performed during the solution procedure involving these boundaries utilise the physical boundary normals and not only those associated with the straight-sided discretisation. This constitutes the improvement in geometrical boundary representation necessary for DG schemes.

5.6.1 Formulation

The technique presented in [33] describes a method by which the solid wall boundary conditions, used in the steady two-dimensional Eulerian model of fluid flow, can be improved when applied to a curved physical boundary. The standard reflecting boundary condition (RBC)

$$\boldsymbol{v} \cdot \boldsymbol{n} = 0 \tag{5.22}$$

where the normal component of the flow velocity is set to zero, states that no flow can penetrate a solid wall. In this statement, the normal $\boldsymbol{n} = (n_x, n_y)$ is taken from the computational boundary, which in a standard mesh comprises piecewise linear segments. Therefore, for a straight-sided physical geometry, where these piecewise linear segments permit a suitably accurate representation of the boundary, this condition works well.

However, when applied directly to more complex curved boundaries, the accuracy of the solution is significantly inferior. Furthermore, contrary to providing an improvement in accuracy, the application of p-refinement to these straight-sided meshes can cause the solution to deteriorate [32]. In this case, application of (5.22) no longer provides an accurate physical interpretation of the flow at this boundary. In fact, due to the disparity between the computational and physical boundaries, we require this condition to be broken, as some of the flow must be able to leave and re-enter the computational domain to enable a better approximation to the condition of no flow through the physical boundary. The benefits of such a technique are believed to outweigh the obvious loss of conservation, a loss which is shown to be negligible in [33].

The algorithm used to obtain this curvature boundary condition (CBC) makes use of the physical geometry to obtain so called ghost values at each integration point located on the curved surface. Subsequently, these values are used in the Roe flux calculation to obtain a boundary flux. Therefore, in this case, the true solid wall boundary condition of no flow through the physical boundary is used

$$\boldsymbol{v} \cdot \boldsymbol{N} = 0 \tag{5.23}$$

where $\boldsymbol{N} = (N_x, N_y)$ is the physical boundary normal.

The procedure to impose this condition numerically proceeds as follows [33]. A ghost state $\boldsymbol{U}^g$ is generated at each integration point $\boldsymbol{x}_i$ on the boundary. The velocity at the boundary is reflected to the ghost state with respect to the physical boundary tangent vector $\boldsymbol{T}$, as shown in Figure 5.10 [33]. Therefore, the normal and tangential velocity components relative to the physical boundary at the ghost state are given by

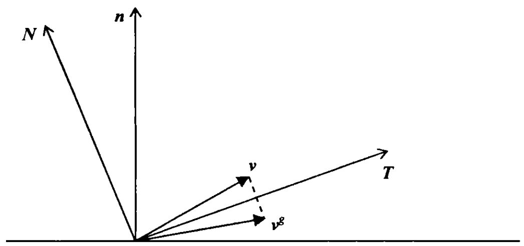

Figure 5.10: Velocity vector reflection

$$\boldsymbol{v}^g(\boldsymbol{x}_i) \cdot \boldsymbol{N}(\boldsymbol{x}_i) = -\boldsymbol{v}(\boldsymbol{x}_i) \cdot \boldsymbol{N}(\boldsymbol{x}_i) \tag{5.24a}$$

$$\boldsymbol{v}^g(\boldsymbol{x}_i) \cdot \boldsymbol{T}(\boldsymbol{x}_i) = \boldsymbol{v}(\boldsymbol{x}_i) \cdot \boldsymbol{T}(\boldsymbol{x}_i) \tag{5.24b}$$

and effectively result in a zero normal velocity to the surface. The pressure p is taken equal to the interior solution value at that point. Subsequently rotating the velocity vectors back into x and y components, the ghost state vector can be expressed as

$$\boldsymbol{U}^g = \begin{Bmatrix} u[(N_y)^2 - (N_x)^2] - 2N_xN_yv \\ v[(N_x)^2 - (N_y)^2] - 2N_xN_yu \\ p \end{Bmatrix}$$

Finally, these values, along with the interior solution values at the corresponding points, are used in the Roe flux calculation to compute the appropriate boundary flux.

5.6.2 Results

We now repeat the scattering model described in Section 5.5.1 with application of the CBC to the straight sides of the mesh used to represent the circular scatterer. The scattering width distributions displayed in Figure 5.11 demonstrate a marked improvement in the convergence of the solution. It is evident in this case that the approximate solutions obtained with application of the CBC are significantly more accurate than the straight sided results of the previous section, where only the standard reflecting boundary condition (RBC) was used.

Unfortunately, although repeating the measurement of the L^2-error norm of the pressure around the surface of the scatterer also shows an improvement in the results, as can be seen in Table 5.2, there is still a limit to the convergence.

Order	TG2	RK4
1	0.65067961	0.54578564
2	0.32505825	0.33937012
3	0.06723746	0.07710083
4	0.08616869	0.08463972
5	0.08855492	0.08838131
6	0.08863865	0.08616391

Table 5.2: L^2-error norm of pressure taken around the scattering surface with application of the CBC

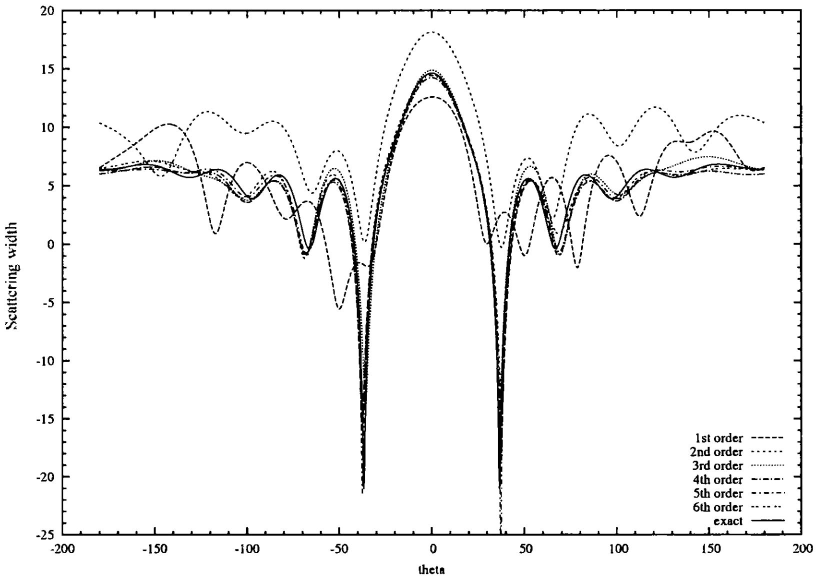

Figure 5.11: Computed scattering width distributions for a 2λ circular scatterer with various element order and a CBC applied to the straight scattering sides

Furthermore, due to the nature of the CBC, direct application of the procedure to the examples of a soft acoustic scatterer or a PEC scatterer in a TM^z field is not possible. Therefore, further improvement of solution accuracy will now be pursued by incorporation of a true higher order geometrical representation. With this, it is hoped that convergence of both the scattering width distributions and surface pressure distribution will be improved.

5.7 Actual Curved Boundary

One of the most obvious methods of improving the fidelity of the boundary representation is to use a higher order geometrical representation. However, due to the resulting non-linear nature of the transformation needed to map an element from physical to computational space, this is achieved as a compromise with increased computational expense.

Fortunately, in this case, we can limit this additional work by noting two things:

firstly, only those elements with boundaries forming part of the curved surface require a higher order representation, and secondly, for each of these elements, only the side that forms the boundary need be curved. Therefore, only a small fraction of the elements and sides which constitute the mesh will be affected by this modification, thus minimising the work per time step associated with this aspect of the model.

5.7.1 Formulation

For the straight-sided physical elements considered previously, the metrics of the Jacobian matrix

$$J = \begin{bmatrix} \frac{\partial x}{\partial \xi} & \frac{\partial y}{\partial \xi} \\ \frac{\partial x}{\partial \eta} & \frac{\partial y}{\partial \eta} \end{bmatrix} \qquad (5.25)$$

required for the transformation of any variational integral statements, were constant throughout the element. However, for elements with curved sides, these gradients can vary over the element, which means that any integral must be performed with these metrics forming part of the integrand. This necessitates the formation of bespoke element matrices for each curved element and, thus, is the reason for the increased computational work.

A typical example of the required transformation is shown diagrammatically in Figure 5.12. It can be seen that only one of the sides of the curved physical element need be represented with a higher order approximation.

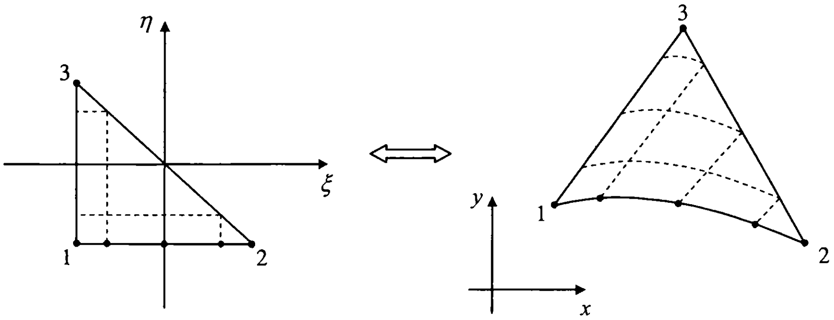

Figure 5.12: Mapping for triangular elements with one curved side

In this case, the mapping can be expressed as

$$\boldsymbol{x} = \sum_{i=1}^{n+2} N_i \boldsymbol{x}_i \tag{5.26}$$

where n is the order of the element and the $n+2$ nodes used in the transformation are the points at each vertex of the element and the remaining GLL points which constitute the curved side. These points are displayed in Figure 5.12 for the example of a fourth order element. Selection of these points enables a higher order representation to be used along the computational ξ direction, which maps the curved side, and a simple linear representation in the η direction. Therefore, the interpolation function for this mapping would then be a product of two polynomials

$$N_i = [a_1 + a_2\xi_0 + a_3\xi_0^2 + \ldots + a_{n+1}\xi_0^n]\frac{1-\eta}{2} \tag{5.27}$$

where

$$\xi_0 = \frac{\xi+1}{1-\eta} \tag{5.28}$$

The metrics of the Jacobian can now be computed as

$$\frac{\partial \boldsymbol{x}}{\partial \xi} = \sum_{i=1}^{n+2} \frac{\partial N_i}{\partial \xi} \boldsymbol{x}_i \tag{5.29}$$

Note that in this case, contrary to the straight-sided elements, the metrics vary over the element. Therefore, the Jacobian component values, including the determinant, must be computed at each quadrature point.

5.7.2 Results

Again, we can now repeat the simple scattering model introduced in Section 5.5.1 with a higher order geometrical approximation of the curved boundary. A further improvement in convergence is evident from the scattering width distributions for the hard acoustic model, displayed in Figure 5.13, as compared with the previous results for the straight sided mesh with and without application of the CBC. From visual inspection, it is seen that the sixth order computational solution is almost identical to the analytical solution.

Furthermore, the measurement of the L^2-error norm of the pressure around the surface of the scatterer, presented in Table 5.3, demonstrates continued convergence, in the case of the higher order RK4 scheme, over the range of element orders used in this analysis.

Order	TG2	RK4
1	0.65614525	0.53429377
2	0.22891995	0.25457812
3	0.04420730	0.06172161
4	0.01532267	0.01487880
5	0.00389915	0.00486275
6	0.00402383	0.00190026

Table 5.3: L^2-error norm of pressure taken around the scattering surface with higher order geometrical representation

A similar improvement in convergence is evident also for the soft acoustic model, the scattering width distributions for which can be seen in Figure 5.14. Although the lower order solutions can be seen to be less accurate in this case compared to the hard acoustic model, the sixth order approximation is, once again, almost identical to the exact solution.

5.8 Complex Circular Wave Scattering Model

As further validation of the hybrid solution method, a more complex circular scattering model, again enabling comparison with an analytical solution, will be approximated. Quite simply, this increase in complexity will be achieved by use of a shorter incident wavelength, thus giving, in an EM context, an increased electrical length. The resulting scattering distribution surrounding the object will then be more intricate, raising the difficulty of accurate approximation.

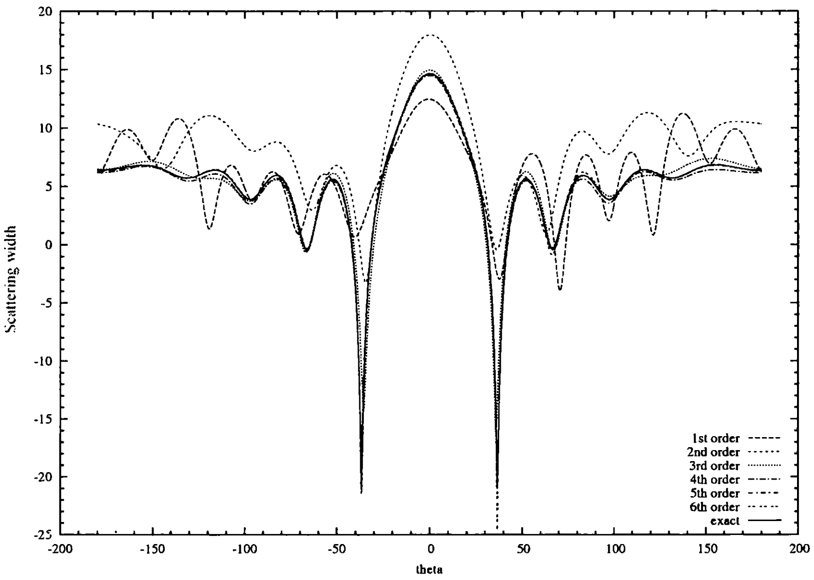

Figure 5.13: Computed scattering width distributions for an acoustically hard 2λ circular scatterer with various element order with higher order geometrical representation

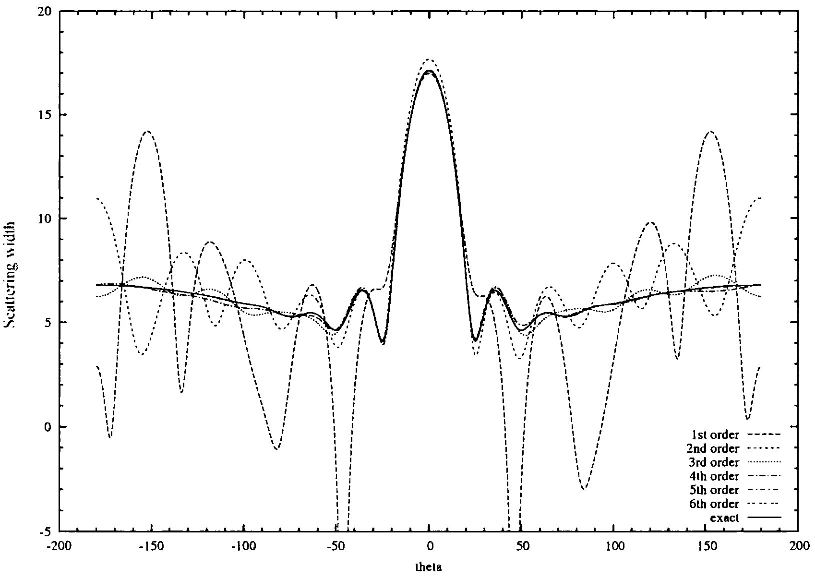

Figure 5.14: Computed scattering width distributions for an acoustically soft 2λ circular scatterer with various element order with higher order geometrical representation

5.8.1 Computational Model

The scatterer in this model will once again have a 3 unit diameter. As a much more refined mesh will be required in this case, it will be placed at the centre of a smaller 6 $\times$ 6 unit domain to minimise computational time. The mesh, as shown in Figure 5.15, comprises of 1062 triangular elements and 2296 quadrilateral elements.

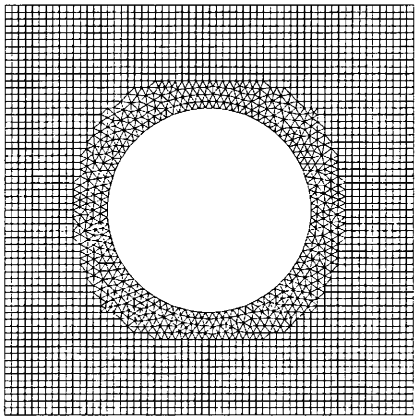

Figure 5.15: Complex circular scatterer mesh

The scatterer will be illuminated by the same form of plane incident sinusoidal wave as described in (5.20). However, to increase the complexity of the model, a wavelength $\lambda = 0.2$ units is chosen, giving an electrical length of 15λ. The model is progressed for 40 wave cycles.

5.8.2 Results

Convergence can be seen in the scattering width distributions displayed in Figure 5.16 and 5.17 for acoustically hard (or PEC scatterer in a TE^z field) and soft (or PEC scatterer in a TM^z field) scatterers respectively. By visual inspection, the distributions obtained with the highest element orders employed in this analysis, are identical to the analytical solution.

For clarity, the scattering width distributions generated by the use of sixth order elements are presented in Figure 5.18 and 5.19. As noted above these computational

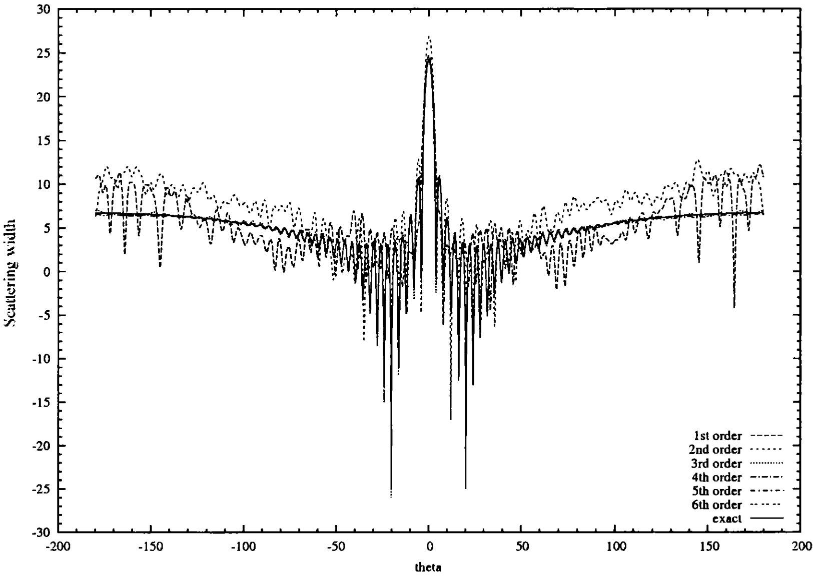

Figure 5.16: Computed scattering width distributions for a 15λ hard acoustic circular scatterer with various element order

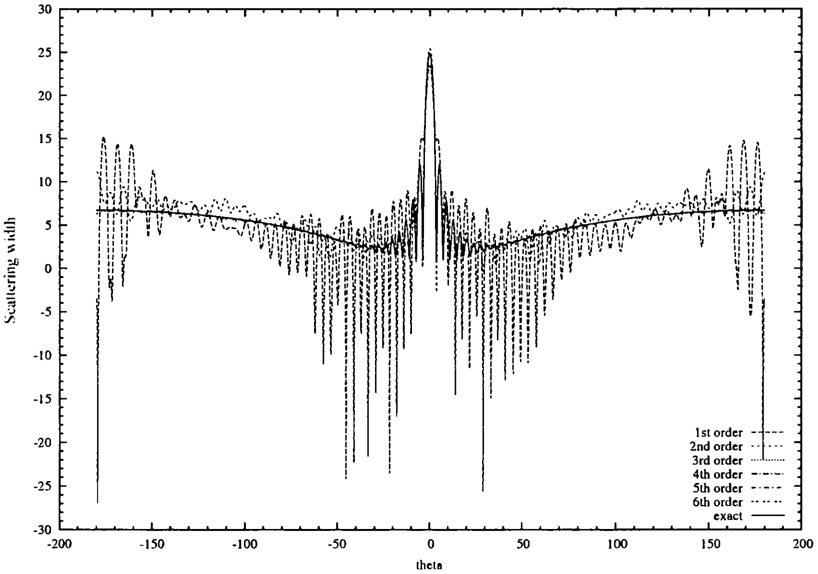

Figure 5.17: Computed scattering width distributions for a 15λ soft acoustic circular scatterer with various element order

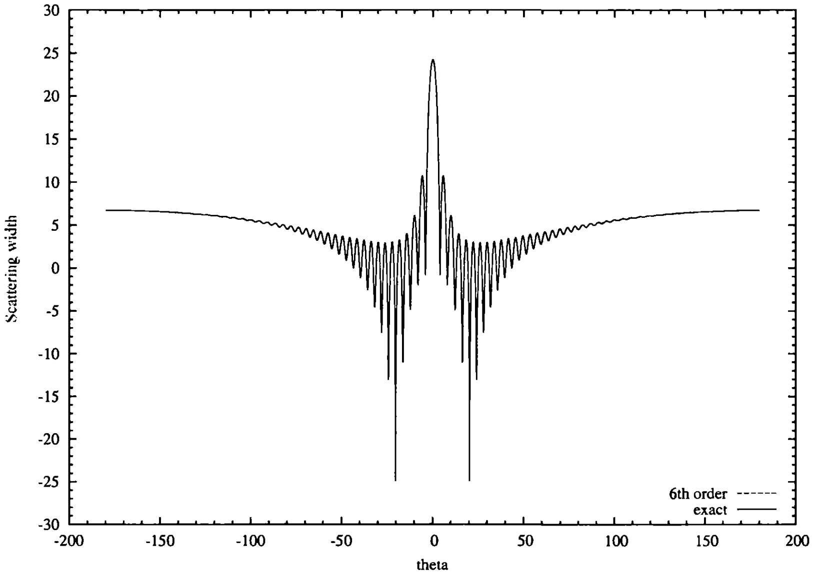

Figure 5.18: Computed scattering width distributions for a 15λ hard acoustic circular scatterer with sixth order elements

solution plots overlie the exact analytical distributions.

The L^2-error norm of the pressure taken around the scattering surface and the computational time are presented in Table 5.4. These will be of greater interest in the discussion of computational efficiency found in the following section.

Order	TG2		RK4	
	L^2-error norm	CPU time (s)	L^2-error norm	CPU time (s)
1	0.47568926	3.93	0.40053259	5.22
2	0.17494481	25.26	0.18506910	34.30
3	0.02512157	59.51	0.03300454	89.29
4	0.01039352	389.88	0.00595719	232.39
5	0.00199468	572.95	0.00113594	617.34
6	0.00038926	12554.50	0.00023372	1507.13

Table 5.4: L^2-error norm of pressure taken around the scattering surface and computational time taken with various element order

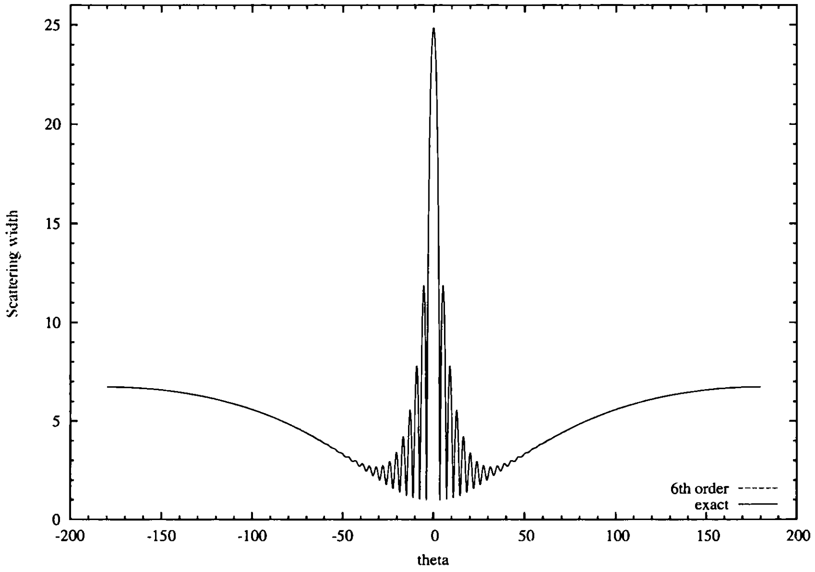

Figure 5.19: Computed scattering width distributions for a 15λ soft acoustic circular scatterer with sixth order elements

5.9 Computational Efficiency

We have now seen that the proposed higher order hybrid solution procedure converges towards the exact solution as desired. However, at this stage, we are yet to discuss any of the potential computational advantages of the use of such higher order spatial approximation. Therefore, in this section, we will attempt to give an indication of the computational savings that may be achieved.

5.9.1 Computational Model

This analysis will utilise the hard acoustic or PEC TE^z polarized EM scattering model, as introduced in Section 5.8 for the complex circular wave scattering example. Therefore, the incident wavelength will be $\lambda = 0.2$ and the diameter of the scatterer will be 15λ.

Having previously applied increasing element order to the mesh shown in Figure 5.15, we will now perform low order linear models on meshes of equivalent increasing refinement. This will be achieved in two ways: firstly, using directly the meshes formed by addition of the spectral Gauss-Legendre-Lobatto (GLL) and Fekete points to the original mesh noted above, and secondly by generating new meshes with approximately the same number of points and elements. The benefits of the first method are that the meshes exist and that the number and positions of the nodes are precisely those employed in each higher order analysis. However, due to the specific grouping of the GLL and Fekete points, the resulting non-uniformity of the mesh may impair the accuracy of the linear model. Therefore, in the second method, the uniformity is restored by generating entirely new meshes to ensure that the accuracy of the linear model is measured fairly. For clarity, an index for the various meshes, including the number of points in each mesh, is given in Table 5.5. For the example of linear meshes with the equivalent number of points as used in the previous fourth order model, Figures 5.20(a) and 5.20(b) display the upper left sections of meshes 4a and 4b respectively.

Non-uniform mesh		Uniform mesh	
Mesh	Number of points	Mesh	Number of points
1a	2994	1b	2994
2a	11642	2b	11684
3a	25944	3b	25722
4a	45900	4b	46011
5a	71510	5b	71611
6a	102774	6b	101684

Table 5.5: Index of linear meshes for circular scatterer

The computational time required to obtain the hybrid solution will be recorded as an indication of the resources required. A single Pentium IV 2.1GHz processor will be used to run the program.

Both TG2 and RK4 temporal discretisation were applied. As the results produced in each case were similar, only the scattering width output generated by the TG2 model need and will be discussed to avoid repetition. However, computational time data will be provided for both schemes.

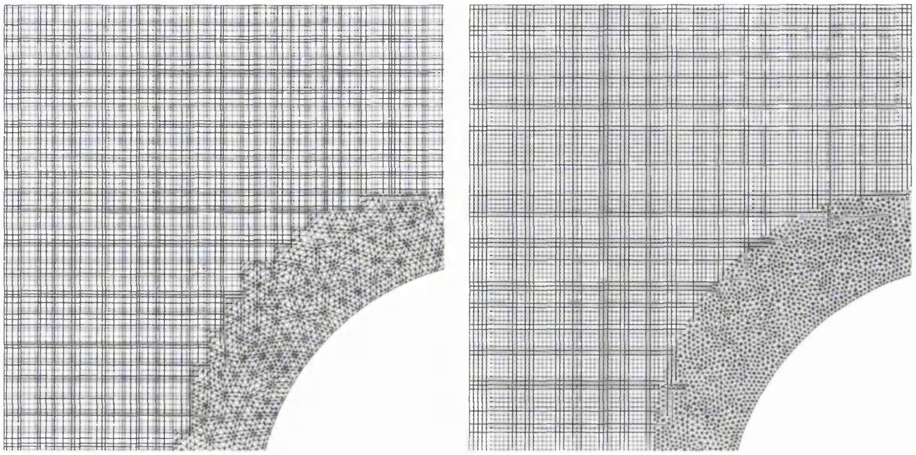

(a) (b)

Figure 5.20: Upper left sections of the equivalent linear meshes to the 4^{th} order mesh: (a) Direct insertion of GLL/Fekete points to original mesh, mesh 4a (b) Creation of new uniformly spaced mesh, mesh 4b

5.9.2 Results

Firstly, we will consider the results of the linear models performed on the non-uniform linear meshes produced directly by addition of the GLL/Fekete points to the original mesh. Table 5.6 presents the L^2-error norm of the pressure taken around the scattering surface and the time taken to obtain the computational solution. The scattering width distributions can be seen in Figure 5.21.

Mesh	TG2		RK4	
	L^2-error norm	CPU time (s)	L^2-error norm	CPU time (s)
1a	0.47568926	3.93	0.40053259	5.22
2a	0.13607195	42.00	0.16632739	50.76
3a	0.06525156	178.09	0.11102243	199.86
4a	0.02976370	449.85	0.04206943	642.04
5a	0.02655390	1080.04	0.04036957	1734.69
6a	0.01957246	2113.57	0.01828267	2721.32

Table 5.6: L^2-error norm of pressure taken around the scattering surface and computational time taken with various non-uniform linear meshes

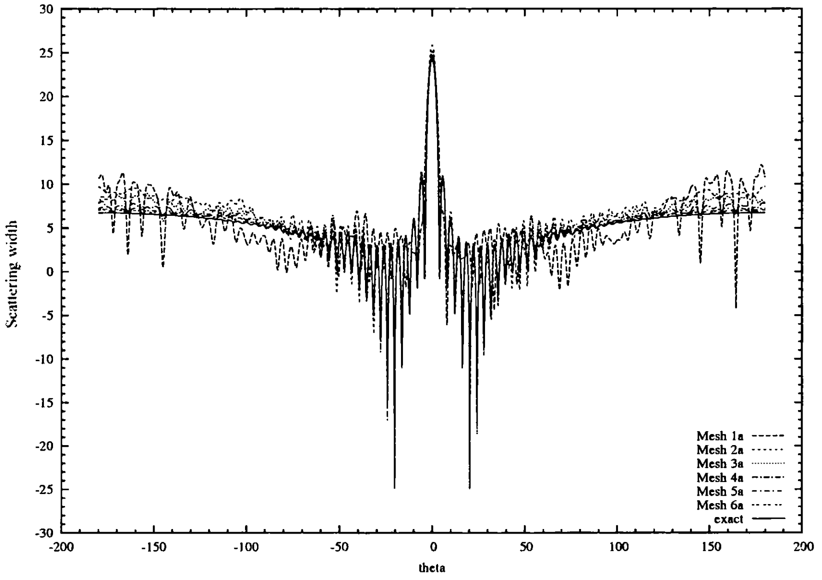

Figure 5.21: Computed scattering width distributions for a 15λ hard acoustic circular scatterer with various non-uniform linear meshes

It is clear that convergence towards the exact solution is occurring at a slower rate with h-refinement than witnessed in the previous section with p-refinement. Focussing on the highest level of refinement (Mesh 6a), where 102774 points were used to generate the mesh which is an equivalent number to the previous sixth order model, Figure 5.22 shows clearly the difference between the approximate and exact scattering width distributions.

Turning now to the results for the linear models performed on the group of more uniform meshes 1b-6b, a significant improvement is evident. Once again, the surface pressure L^2-error norm and computational time are shown in Table 5.7, while Figure 5.23 presents the scattering width distributions in this case. A greater level of convergence for the highest refinement is clear to see in Figure 5.24.

Note also, that in this hybrid solution procedure, time-steps are global and are governed by the minimum element characteristic dimension. Therefore, in general, the models run on the non-uniform meshes 1a-6a have a smaller minimum element dimension and thus take more computational time.

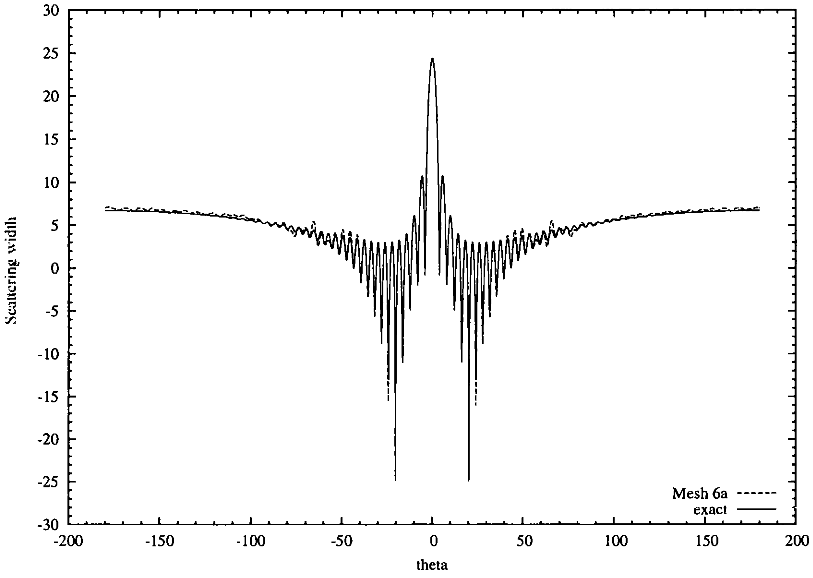

Figure 5.22: Computed scattering width distribution for a 15λ hard acoustic circular scatterer with a non-uniform linear mesh of 102774 points (Mesh 6a)

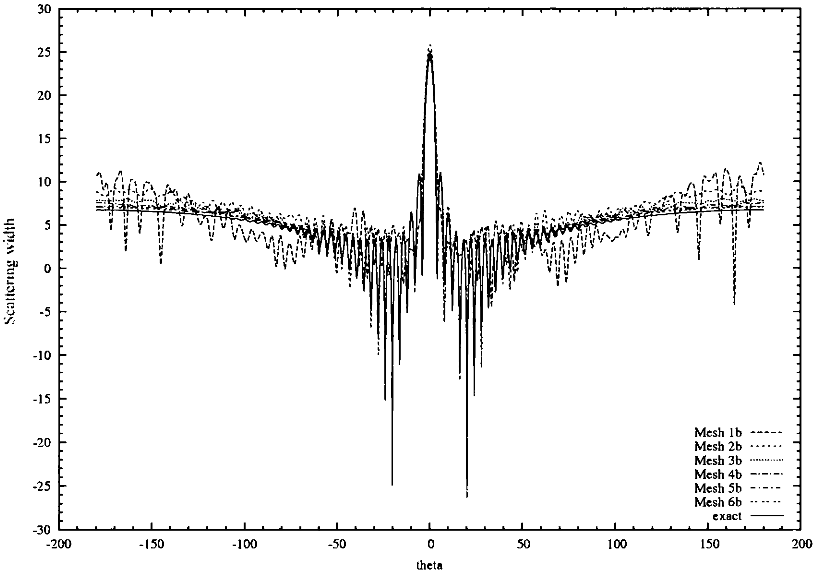

Figure 5.23: Computed scattering width distributions for a 15λ hard acoustic circular scatterer with various uniform linear meshes

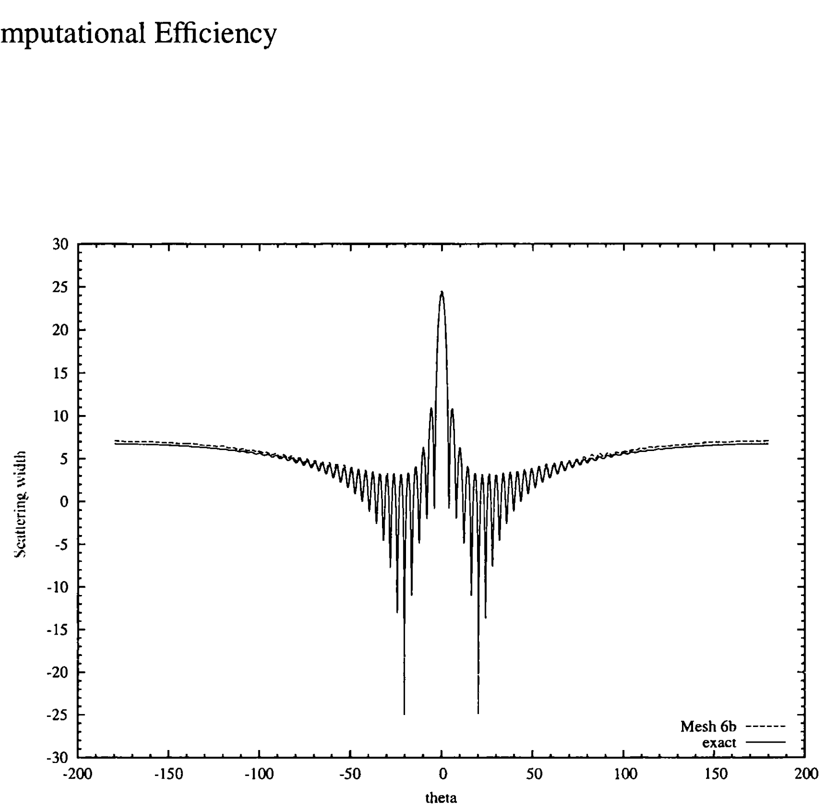

Figure 5.24: Computed scattering width distribution for a 15λ hard acoustic circular scatterer with a uniform linear mesh of 102774 points (Mesh 6b)

Mesh	TG2		RK4	
	L^2-error norm	CPU time (s)	L^2-error norm	CPU time (s)
1b	0.47568926	3.93	0.40053259	5.22
2b	0.12642516	46.25	0.15339789	55.42
3b	0.05603743	149.15	0.06954133	200.66
4b	0.03041981	384.96	0.03603510	516.36
5b	0.01876451	969.68	0.02200313	1387.62
6b	0.01334953	1613.38	0.01571360	1833.23

Table 5.7: L^2-error norm of pressure taken around the scattering surface and computational time taken with various uniform linear meshes

Now by comparison with the results of the higher order method, presented in Table 5.4, we can begin to assess the computational advantages of the higher order spatial approximation. For example, considering the results from the most refined uniform mesh (Mesh 6b), which with application of the TG2 temporal scheme gave an error norm of $L^2_{\Gamma_{scat}} = 0.01334953$, this is of the same order as the error given by the previous fourth order model. Subsequent comparison of the computational time taken in each case shows that the duration of the linear model was a factor of 4 greater than that of the fourth order approximation. This is only one example, giving an indication of the general trend. However, it is quite clear that the remaining data would permit further favourable comparisons to be made highlighting the reduced computational work needed by the higher order methods for this problem.

To conclude the analysis, we generated one further uniform linear mesh of increased refinement in an attempt to reach the accuracy of the higher order solutions. This final mesh comprised 182075 points and 215566 elements and resulted in solutions with error norms and computational times of $L^2_{\Gamma_{scat}} = 0.00740602$ in 4163.69s and $L^2_{\Gamma_{scat}} = 0.00858994$ in 5406.27s for the TG2 and RK4 schemes respectively. For the output with the RK4 scheme, this also approaches the error norm obtained with the previous fourth order model obtained with the RK4 scheme ($L^2_{\Gamma_{scat}} = 0.00595719$). However, here the computational time taken by the linear model was over a factor of 20 greater.

Therefore, the potential for p-convergence observed in each of the initial stages of development, as discussed in Chapters 3 and 4, has thus been successfully translated to these initial hybrid wave scattering models. As a result, significant computational savings have been achieved. It now remains to see whether similar results can be attained for more complex scattering problems.

5.10 Extended Time Integration Stability

One final aspect of higher order approximation methods which must be considered is their stability after prolonged time integration periods. In terms of wave propagation analysis this of concern for problems which require the propagation of a significant number of wave cycles.

5.10.1 Model

We will employ the simple 2λ circular wave scattering model of Section 5.5 to analyse the stability of the procedure as the number of wave cycles is increased. All we require is that the approximation be shown to be stable within a reasonable range of long term integration times. Therefore, we will obtain numerical solutions to this model following 12, 100, 1000, 10000 and 100000 cycles of the incident plane sinusoidal wave, as defined in expression 5.20, repeating the analysis with first, third and fifth order approximations.

5.10.2 Results

The output of this long term stability analysis is presented in Tables 5.8, 5.9 and 5.10 for the first, third and fifth order approximation respectively. The L^2 error norm is taken around the surface of the scatterer.

Solution time	Number of wave cycles	L^2 error norm	CPU time (s)
18.0	12	0.65614525	0.11
150.0	100	0.65703590	0.36
1500.0	1000	0.65706626	2.92
15000.0	10000	0.65665306	28.94
150000.0	100000	0.65223623	292.56

Table 5.8: Long term stability analysis performed with a first order approximation, displaying the L^2 error norm taken around the surface of the scatterer after various solution times

Solution time	Number of wave cycles	L^2 error norm	CPU time (s)
18.0	12	0.04420725	1.08
150.0	100	0.04418392	6.22
1500.0	1000	0.04421799	58.45
15000.0	10000	0.04461829	582.19
150000.0	100000	0.04908678	5735.06

Table 5.9: Long term stability analysis performed with a third order approximation, displaying the L^2 error norm taken around the surface of the scatterer after various solution times

Solution time	Number of wave cycles	L^2 error norm	CPU time (s)
18.0	12	0.00389925	18.41
150.0	100	0.00389431	61.52
1500.0	1000	0.00383522	497.08
15000.0	10000	0.00328885	4858.56
150000.0	100000	0.00621470	50537.69

Table 5.10: Long term stability analysis performed with a fifth order approximation, displaying the L^2 error norm taken around the surface of the scatterer after various solution times

As can be seen, the numerical procedure remains stable as the solution time is increased in all cases, with only a small increase in error for the third and fifth order approximations after 100000 wave cycles. Therefore, we can be satisfied that this higher order hybrid approximation method for wave scattering problems will be stable for long term problems.

5.11 Conclusion

Firstly, the hybrid solution procedure was validated with the simple Gaussian pulse propagation test. As with the separate SEM and spectral DGM, this demonstrated that p-convergence was still possible with the hybrid formulation.

Having established this, further ground work was conducted prior to the initiation of wave scattering modelling. The requirement for an accurate truncation method to approximate the infinite physical domains encountered in such models was discussed and the concept of perfectly matched layers was introduced. Subsequently, the chosen formulation used to incorporate such a layer within the solution method was presented and the resulting governing equations were derived.

In due course, a simple model of scattering from a 2λ circular object was attempted. This highlighted the importance of accurate geometrical representation of curved boundaries, leading to the incorporation of a recently proposed curvature boundary condition [33] and, ultimately, to a higher order boundary approximation. Results with both of these methods exhibited improvements in the solution accuracy, although the higher order geometrical approximation was the most successful. A further, more complicated model of a 15λ circular scatterer was also approximated, which showed clearly the computational solution converging towards the exact solution.

This lead to an investigation of the possible computational savings attainable with higher order spatial approximation. Comparison with low order linear models performed on meshes of increasing refinement demonstrated the efficiency of the proposed hybrid high order method.

Therefore, it is believed that the efficacy of this hybrid solution procedure has been suitably confirmed. Analyses of various other scattering geometries can now commence, the discussion of which can be found in the following chapter.

Chapter 6

Further Scattering Models

6.1 Introduction

There is an unbounded number of possible configurations for practical scatterers. In cutting edge technological fields such as the aerospace industry, advances in design can bring forth increasingly complicated and intricate geometries. This rise in complexity, in turn, promotes the need for more accurate and efficient solution methods which enable an in-depth numerical analysis to be conducted.

Having completed the validation of the proposed higher order hybrid finite element method, work can proceed to the analysis of more complicated scattering geometries. We will not, at this stage, approach the complexity suggested above, but the properties of the chosen models should hopefully provide an adequate indication of the potential of the method, in addition to any possible limitations.

Due to the form of these geometries, analytical solutions for comparison with the computed approximations will be unavailable. Therefore, validation of the generated scattered fields and associated quantities will be performed, where possible, by reference to previously computed numerical solutions obtained by various research groups. Ultimately, we will endeavour to show that the accuracy and efficiency of this method can surpass that offered by lower order spatial approximation.

6.2 Dihedral Scatterer

The first model that will be considered is a dihedral scatterer. Formed only by two legs lying perpendicular to each other, the simplicity of this geometry may belie its usefulness. However, it should be noted, that the thickness of the legs in relation to their length and the sharp geometrical features will provide an interesting insight into the resolution properties of the method. The singularities present in the physical solution will serve as an adequate initial test for the convergence of the solution.

6.2.1 Scattering Model

The problem considered is a PEC scatterer placed in a TE^z polarized electromagnetic field, which is analogous to acoustic scattering from a hard surface. The geometry of the dihedral scatterer used in this example can be seen in Figure 6.1. A unit wavelength will be used, giving the scatterer an approximate electrical length of 10λ, and the model will be progressed for 50 cycles.

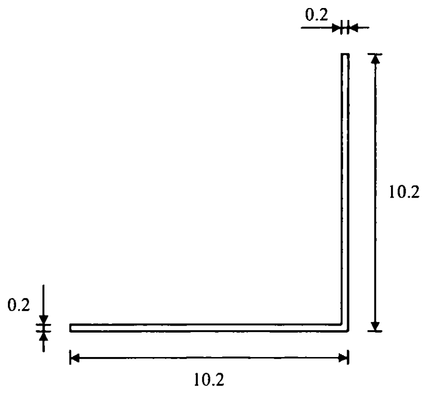

Figure 6.1: Dihedral scatterer geometry

Contrary to the previous example of wave scattering from a circular object, the orientation of the geometry within the incident wave field will affect the resulting scattered wave distribution. Therefore, various incident wave directions will be modelled to obtain the scattered field and scattering width distribution associated with each. The selected range of directions will be $\theta = 120°, 135°, 150°, 180°$, where, for example, an angle of $\theta = 180°$ defines an incident wave travelling horizontally along the positive x-axis. The initial mesh used in this analysis is displayed in Figure 6.2. Note that, due to their relatively small dimension, the thickness of each dihedral leg is discretised by only one element.

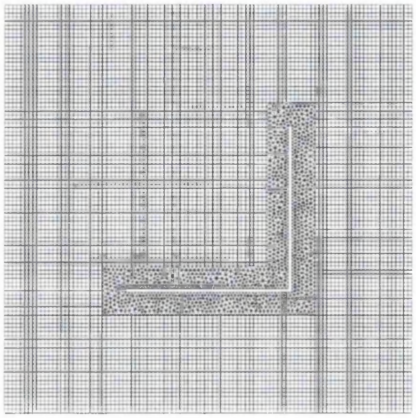

Figure 6.2: Initial dihedral mesh

6.2.2 Results

As an example of the output for this dihedral scattering model, the H^z wave fields generated for an incident direction of $\theta = 180°$, using a third order spatial approximation, are shown in Figure 6.3. An expected plane wave reflection is seen from the vertical internal face, while a shadow region lies behind it when viewing the total field.

However, looking now at the convergence of the scattering width distributions, Figure 6.4 highlights the limitations of p-refinement in high field variation regions. It is evident that the convergence of the solution is unstable as the fourth order model differs significantly from the third and fifth order approximations, which almost overlie each other.

When approximating smooth functions, such as a sinusoidal wave, p-refinement works very well and has been shown to be more computationally efficient than using h-refinement with linear elements. However, if high gradients or singularities exist

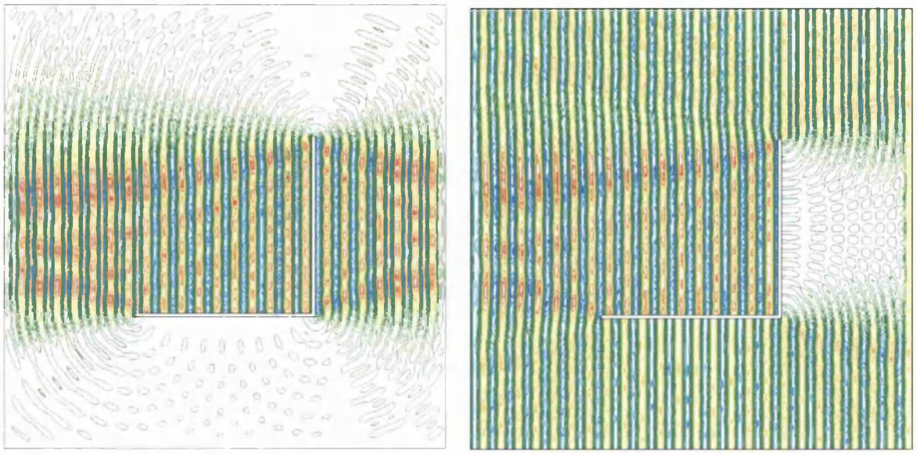

(a) (b)

Figure 6.3: H^z wave fields generated by a third order model of PEC dihedral scatterer in a TE^z polarized EM field (a) Scattered field (b) Total field

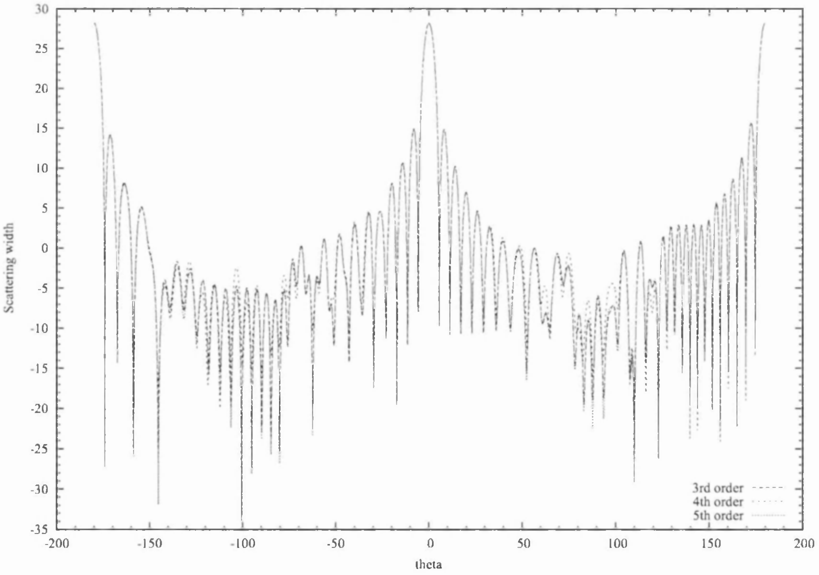

Figure 6.4: Scattering width distributions for a PEC dihedral scatterer in a TE^z polarized EM field using element orders 3 to 5

in the solution, then p-refinement alone may not be sufficient. In these cases, some h-refinement, localised to the region of high-gradient, may be needed to permit p-convergence to occur [53].

For this dihedral model, as there are sharp corners in the geometry, the exact solution will contain singularities. Consequently, the approximation must be able to resolve these and other high gradient regions appropriately. In this initial attempt, the mesh employed to discretise the domain used only one element to approximate the thickness of the dihedral legs. Therefore, with this example, it has been demonstrated that this is insufficient and we will increase the refinement of the mesh which directly surrounds the scatterer. The leg thickness will now be approximated by two elements. The resulting scattering width distributions are presented in Figure 6.5. Here, it can be seen that the approximations approach the converged solution without oscillation.

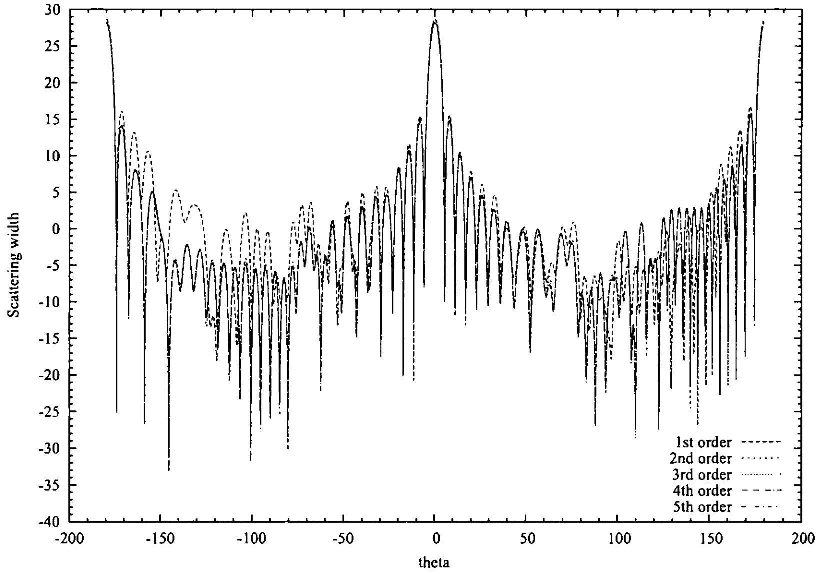

Figure 6.5: Scattering width distributions for a PEC dihedral scatterer in a TE^z polarized EM field using various element order on a mesh of increased refinement

Having removed the instability in the convergence by increasing the mesh refinement, various other incident directions can be modelled. Figures 6.6 to 6.8 display the scattered wave fields and scattering width distributions for incident directions $\theta = 150°, 135°, 120°$ respectively. Mesh convergence can be seen in each case.

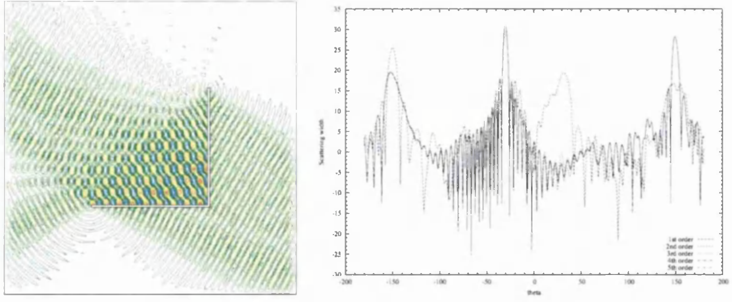

(a) (b)

Figure 6.6: Dihedral scatterer. Incident wave direction $\theta = 150°$ (a) H^z scattered field with third order elements (b) Scattering width with various element order

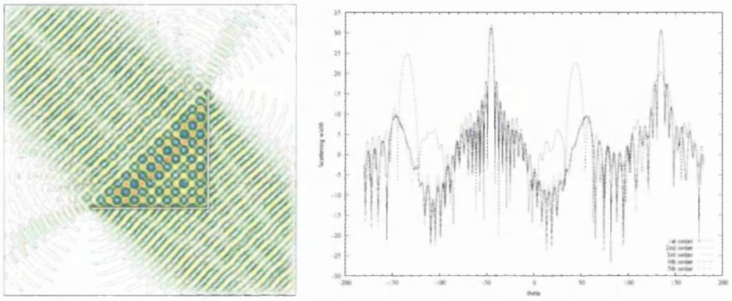

(a) (b)

Figure 6.7: Dihedral scatterer. Incident wave direction $\theta = 135°$ (a) H^z scattered field with third order elements (b) Scattering width with various element order

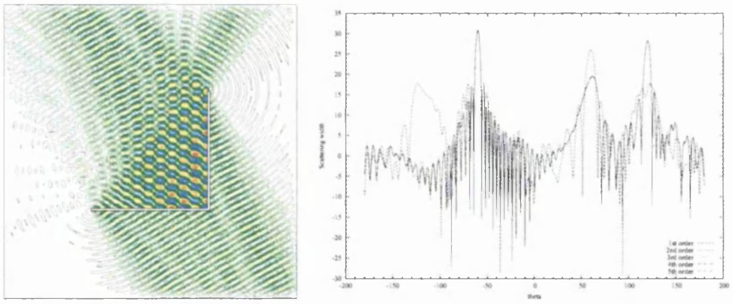

(a) (b)

Figure 6.8: Dihedral scatterer. Incident wave direction $\theta = 120°$ (a) H^z scattered field with third order elements (b) Scattering width with various element order

6.2.3 Computational Efficiency

From examination of the scattering widths in Figure 6.5, we see that convergence has occurred to a reasonable degree by third order. This spatial approximation comprised 151860 points and 19163 elements and the computational time taken to reach the numerical solution was 2119 seconds. We will now attempt to reach convergence by employing a reduction in element size only (h-refinement) with a linear approximation and subsequently compare the computational work required in each case. An index displaying the number of points and elements contained within each mesh can be seen in Table 6.1. It should be noted that the number of points in each mesh, numbered 1 to 6, is approximately equivalent to the number of points contained in a n^{th} order approximation applied to the original mesh 1. For example, the third order approximation presented in Section 6.2.2 contained 151860 points, which is comparable to the number contained in linear mesh 3.

Mesh	Number of points	Number of elements
1	17176	19163
2	67796	76652
3	147730	163467
4	269368	306608
5	408217	452405
6	585363	647034

Table 6.1: Index of linear meshes for dihedral scatterer

Figure 6.9 presents the scattering width distributions obtained with meshes 1 to 6 with a linear approximation. As was seen in Section 5.9, convergence is occurring at a slower rate than with the equivalent higher order approximations. To clarify the accuracy of the solution on the more refined linear meshes, Figure 6.10 facilitates a comparison of the scattering width distributions produced on meshes 4-6 with the fully converged fifth order approximation of the previous section. Even with the most refined mesh (mesh 6), the distribution is far from convergence for certain viewing angles. Nonetheless, on mesh 6, the computational time taken to obtain the solution

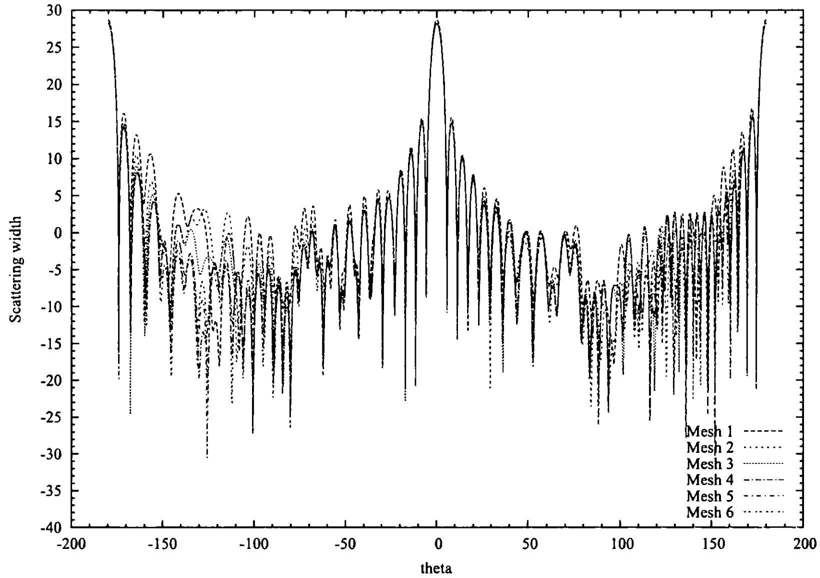

Figure 6.9: Scattering width distributions for a PEC dihedral scatterer in a TE^z polarized EM field using various mesh refinements (meshes 1-6) with a linear approximation

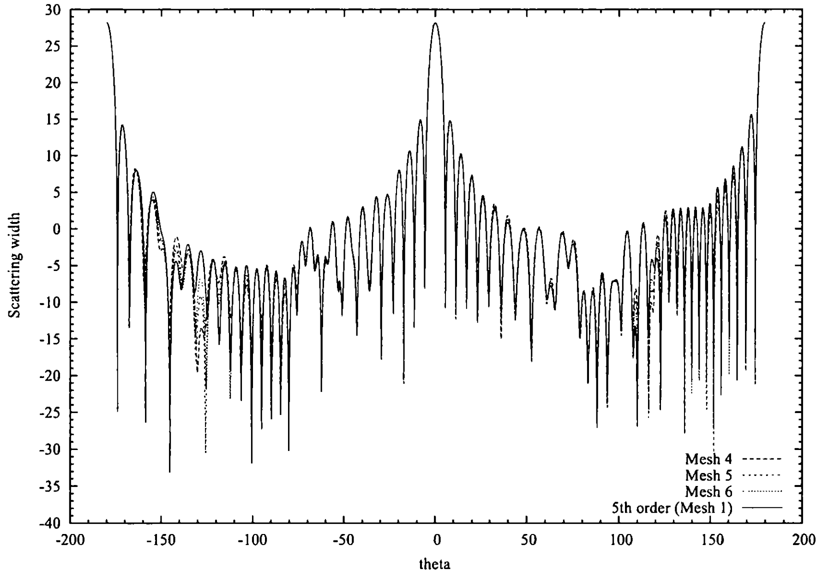

Figure 6.10: Scattering width distributions for a PEC dihedral scatterer in a TE^z polarized EM field using various mesh refinements (meshes 4-6) with a linear approximation, compared with a fifth order approximation on the original mesh (mesh 1)

was 46415 seconds, almost 22 times greater than for the third order approximation quoted above.

In an attempt to achieve convergence, a further mesh was generated with 1073840 points and 1226432 elements (mesh 7). The scattering width distribution for this discretisation is shown in Figure 6.11. It is evident that the accuracy of this linear approximation is still inferior to the previous third order model.

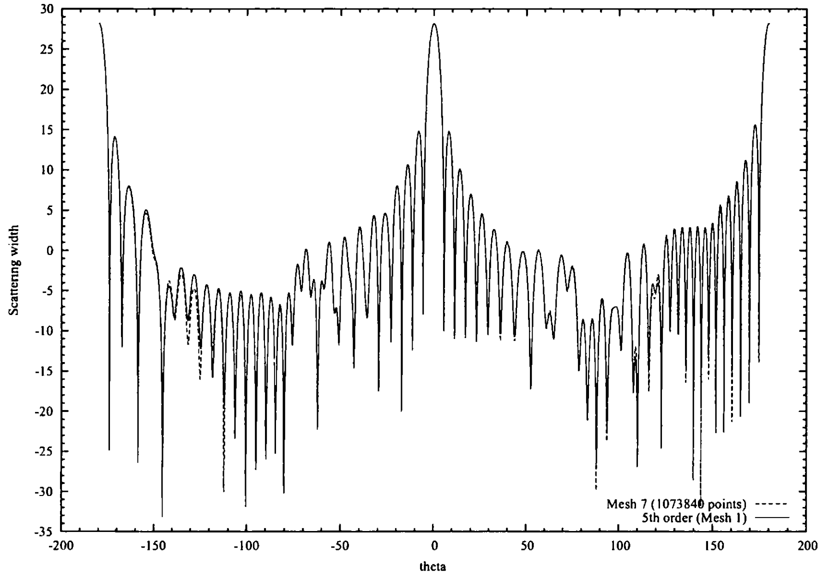

Figure 6.11: Scattering width distribution for PEC dihedral scatterer in a TE^z polarized EM field using a linear mesh of 1073840 points (mesh 7)

6.3 Open Cavity Scatterer

As an extension to the previous scattering problem, we will now consider the example of a straight-walled open cavity. At the outset of this thesis, in the discussion of model requirements found in Chapter 1, the intricate geometries of practical scatterers was discussed and the resulting requirement for extended integration times was stated. Therefore, the purpose of this model will be to assess how the method will cope with the increased scattering field interaction within the cavity of this relatively simple example.

6.3.1 Scattering Model

As previously, the problem considered is a PEC scatterer within an incident plane sinusoidal TE^z polarized electromagnetic field of unit wavelength. Figure 6.12 displays the geometry of the straight-walled open cavity. The mesh used to discretise this geometry can be seen in Figure 6.13 and consists of 5594 triangular elements and 1924 quadrilateral elements.

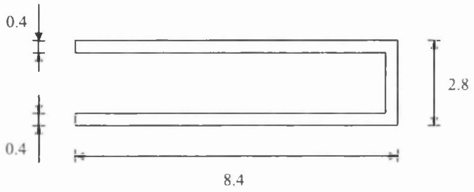

Figure 6.12: Straight-walled open cavity scatterer geometry

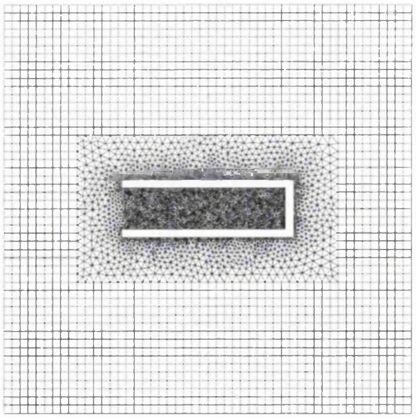

Figure 6.13: Straight-walled open cavity mesh

Due to the level of wave interaction that will occur within the cavity, it is likely that the computational time, required for the approximate solution to reach a steady harmonic state, will be increased. To establish at what time this occurs, we will first utilise a third order spatial approximation and obtain solutions for various computational times.

Once this has been completed, we will proceed with the p-convergence analysis for this model and present results for two incident wave directions: $\theta = 180°, -120°$. Finally, to assess the efficiency of the higher order approximations, we will attempt to obtain solutions for the $\theta = 180°$ incident direction model with linear approximation applied to meshes of increased h-refinement.

6.3.2 Results

We begin with the results of the preliminary analysis concerning the time taken to reach a steady harmonic state. The scattering width distributions generated by the third order approximation for various solution times are presented in Figure 6.14.

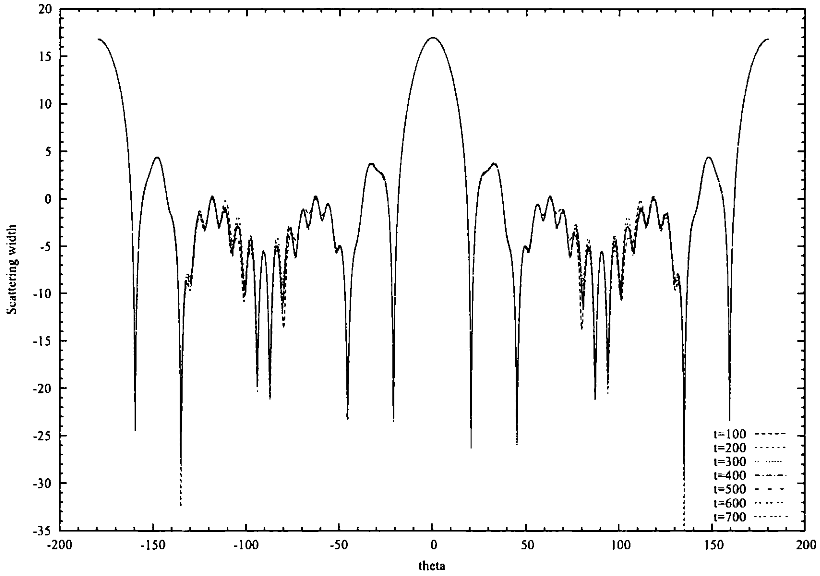

Figure 6.14: Scattering width distribution for a PEC open cavity in a TE^z polarized EM field with incident wave direction $\theta = 180°$ using a third order approximation with various solution times

As can be seen, the distributions converge towards a common solution, and hence approach a steady harmonic state, at approximately $t = 600$. Therefore, in the following work, this will be the chosen solution time.

An example of the output for this open cavity model can be seen in Figure 6.15.

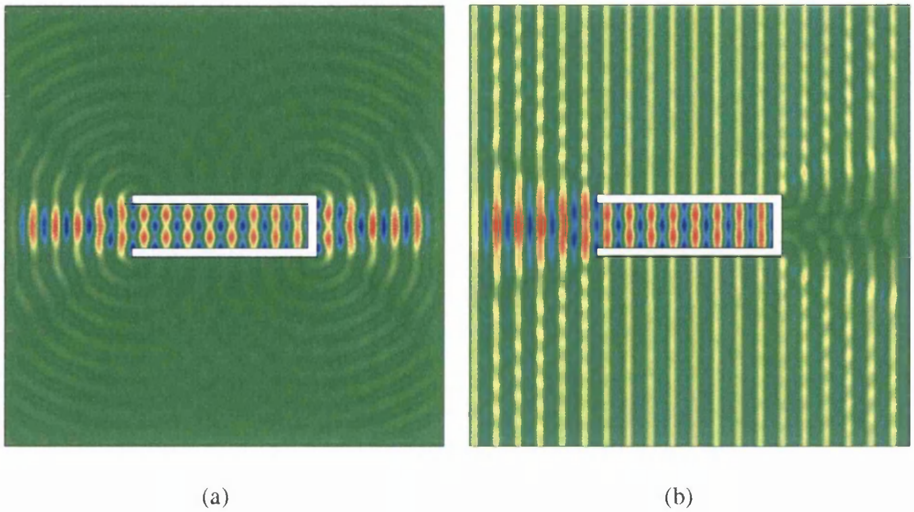
(a) (b)

Figure 6.15: H^z wave fields for fifth order model of a PEC open cavity in a TE^z polarized EM field (a) Scattered field (b) Total field

These are the scattered and total H^z wave fields generated for an incident direction of $\theta = 180°$ using a fifth order spatial approximation.

The scattered width distributions for incident wave directions $\theta = 180°, -120°$, generated using various element order, are presented in Figures 6.16 and 6.17 respectively. As can be seen, the numerical solutions are converging as the approximation order is raised and by visual inspection show close similarity with the results of Ledger [54]. For comparison with the following linear analysis applied to meshes of increased h-refinement, the computational time taken to generate the solution for the $\theta = 180°$ model are displayed in Table 6.2.

6.3.3 Computational Efficiency

In this section, we will recompute the scattering width distributions for the open cavity model using linear approximation only. To improve the accuracy of the solution we will rely solely on h-refinement, using a series of meshes of increasing refinement. The meshes used in this analysis are listed in Table 6.3.

We consider a scattering problem with an incident wave direction $\theta = 180°$. The

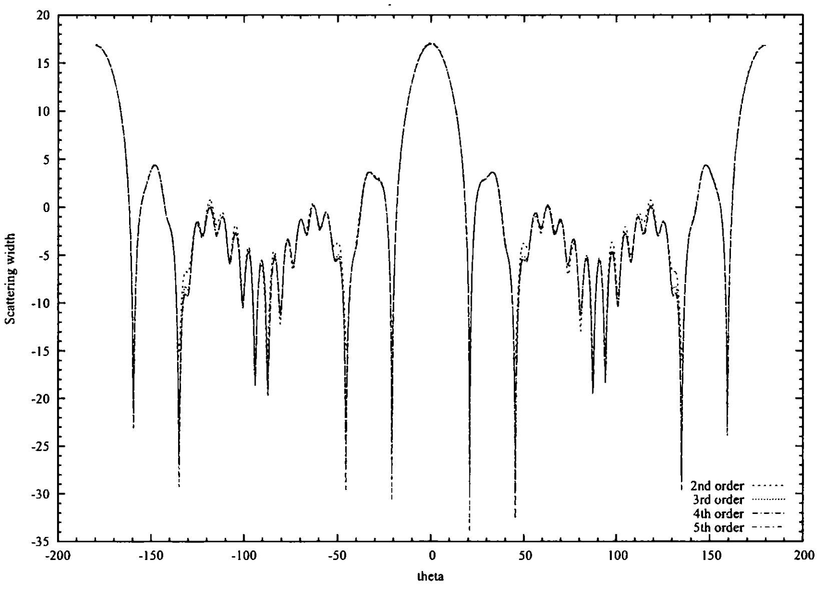

Figure 6.16: Scattering width distribution for a PEC open cavity in a TE^z polarized EM field with incident wave direction $\theta = 180°$

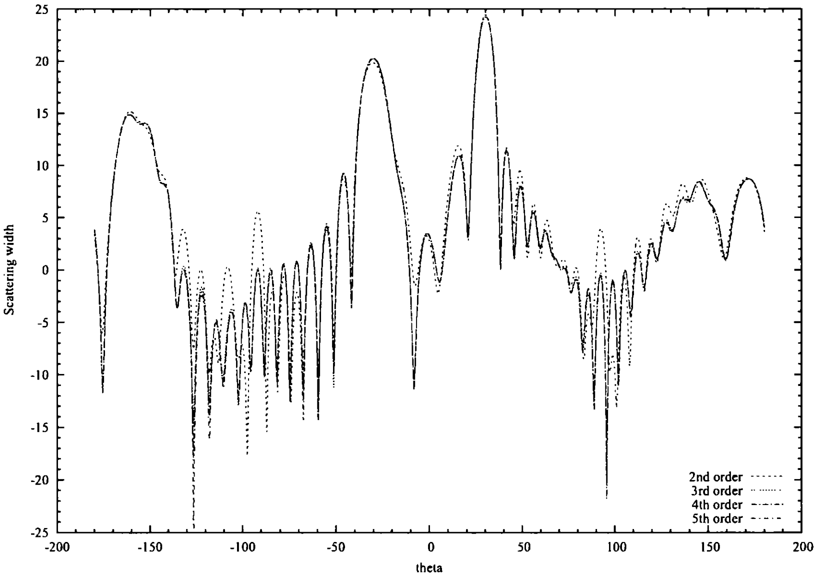

Figure 6.17: Scattering width distribution for a PEC open cavity in a TE^z polarized EM field with incident wave direction $\theta = -150°$

Order	Number of points	CPU time (s)
1	5013	939.78
2	19468	4217.40
3	43365	12368.00
4	76704	81544.09
5	119485	95911.52

Table 6.2: Number of points and computational time taken with various approximation order to generate the solution for the open cavity model with incident wave direction $\theta = 180°$

Mesh	Number of points	CPU time (s)
2	18018	7644.87
3	37927	22918.07
4	63237	42216.18
5	93825	87900.48

Table 6.3: Mesh index for open cavity linear approximation comparison, with the number of points used in each mesh and the computational time required to generate the solution

scattered width distributions generated on each mesh can be seen in Figure 6.18.

By comparison with Figure 6.16, it is clear that the use of p-refinement on the initial mesh, displayed in Figure 6.13, offers greater improvement in accuracy than offered by employing linear approximation on meshes of equivalently increased discretisation.

6.4 NACA0012 Aerofoil

As a more practical example, a model of a NACA0012 aerofoil is considered. The NACA four-digit series is a simple classification system for aerofoil geometries: the first digit represents the aerofoil's maximum camber as a percentage of its chord length, the second specifies the position of the maximum camber in terms of tenths of chord length measured from the leading edge, and the third and fourth define the maximum thickness of the aerofoil as a percentage of the chord. Hence, for the

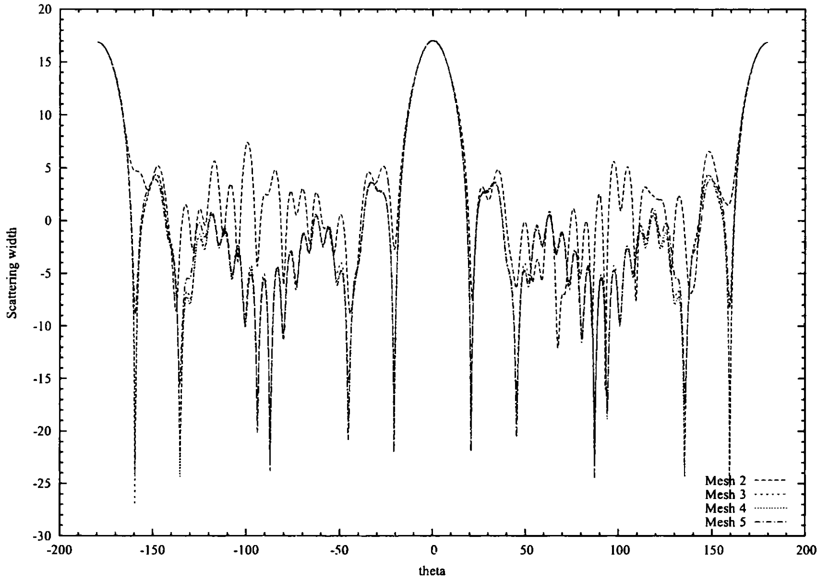

Figure 6.18: Scattering width distribution for a PEC open cavity in a TE^z polarized EM field with incident wave direction $\theta = 180°$

NACA0012 aerofoil, its camber is zero and the geometry is specified by the distribution of thickness, which can be expressed as

$$y = \pm \frac{t}{0.2}\left(0.2969\sqrt{x} - 0.1260x - 0.3537x^2 + 0.2843x^3 - 0.1015x^4\right) \qquad (6.1)$$

where t is the percentage thickness, 12% in this case, represented by the last two digits of the NACA code.

6.4.1 Practical Curved Geometry Representation

Before attempting this wave scattering model, we must first consider the curved boundary representation for the aerofoil geometry. In the analysis of Section 5.5, where various methods of boundary representation were employed, it was assumed that an analytical expression was available from which to obtain the additional element boundary points needed to form the curved scattering boundary. In practical problems this may not always be the case. For example, a higher order model may be required for a scattering object using only a given mesh data file. Hence, for the additional boundary points to be inserted between the existing points in this file, an approximation must be made.

A common method of forming a curve through a given set of points is spline interpolation [55]. By giving certain information concerning the positions of the points, the tangent of the curve or its curvature, a function can be obtained with which any additional points along the curve can be generated. The most popular method is known as a cubic spline, giving a compromise between accuracy and efficiency. Therefore, for the NACA0012 model, this approximation will be used. An expression for the cubic spline interpolation can be found in Appendix D.

However, to assess the effect of this approximation on the accuracy of the solution we must perform a comparison with a known analytical solution. Returning to our standard 2λ circular scattering model, we will repeat the analysis of Section 5.7 for the model with curved element sides. However, in this case, the additional points needed for the higher order approximation will be obtained by cubic interpolation through the initial mesh boundary points.

The scattering width distributions for the circular scattering model obtained using higher order approximation on meshes formed with cubic spline interpolation can be seen in Figure 6.19 with the L^2 error norm taken around the scattering surface presented in Table 6.4. These L^2 error norms are inferior to those generated by the circular model using the analytical expression for boundary point insertion, as shown in Table 5.3. However, the results are still an improvement over the straight sided approximation both with and without the curvature boundary condition (CBC) displayed in Tables 5.1 and 5.2 respectively. Furthermore, the scattering width distributions generated with various approximation order can be seen to converge well to that of the exact solution in Figure 6.19.

6.4.2 Scattering Model

For the NACA0012 aerofoil model, we once again consider a scattering problem with a PEC surface within an incident plane sinusoidal TE^z polarized electromagnetic

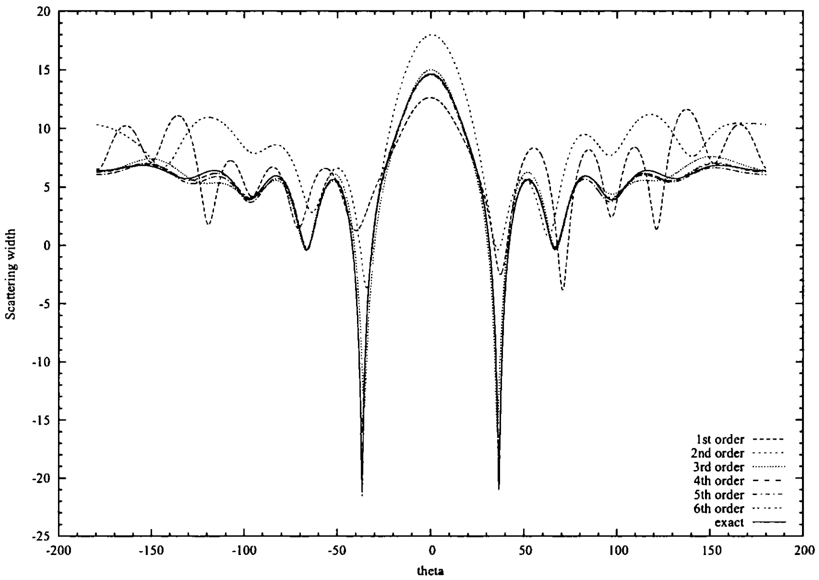

Figure 6.19: Scattering width distributions for a 2λ PEC circular scatterer in a TE^z polarized EM field with various element order using cubic spline interpolation

Order	TG2
1	0.65614525
2	0.22305403
3	0.05436597
4	0.02798900
5	0.01715972
6	0.01974077

Table 6.4: L^2-error norm taken around the scattering surface of a 2λ PEC circular object in a TE^z polarized EM field using cubic spline interpolation

field, equivalent to acoustic scattering from a hard surface. The incident field is set to propagate horizontally towards the leading edge. Three models will be considered, each with different aerofoil chord lengths giving scattering models of electrical length 2λ, 10λ and 100λ. This will increase the complexity of the model, testing the ability of the procedure to resolve both low and high wavenumber fields. Correspondingly, meshes of increased refinement will be required as we increase the electrical length and these will be presented with the results in the next section.

6.4.3 Results

We begin with the model of the 2λ aerofoil. The mesh used to discretise the space surrounding the aerofoil can be seen in Figure 6.20(a) and consists of 304 quadrilateral elements and 388 triangular elements. An example of the H^z scattered wave field generated by a fifth order approximation upon this mesh is presented in Figure 6.20(b). With this simple example, the approximation to the scattering width distribution produced by all orders is reasonably accurate, as is shown in Figure 6.21, and compares well with the results for the same model presented by Ledger *et al* [12]. The computational times required to obtain the solution with various approximation order for this model are displayed in Table 6.5.

Order	Number of points	CPU time (s)
1	558	1.51
2	2112	8.18
3	4662	27.44
4	8208	1457.01
5	12750	315.74
6	18288	14437.56

Table 6.5: Number of points used in the spatial approximation and computational time taken with various approximation order to generate the solution for the 2λ NACA0012 aerofoil model

Proceeding to the 10λ model, the mesh and typical H^z scattered field are displayed in Figures 6.22(a) and 6.22(b). Convergence of the solution does occur as the approximation order is increased, Figure 6.23, but in this case, reasonable accuracy is only achieved with third order elements and above. Information concerning each mesh used in this analysis is contained in Table 6.6.

Order	Number of points	CPU time (s)
2	7428	48.30
3	16533	156.70
4	29232	4613.78
5	45525	1440.75
6	65412	71561.93

Table 6.6: Computational time taken with various approximation order to generate the solution for the 10λ NACA0012 aerofoil model

Finally, for the case of the highest wavenumber field, Figures 6.24(a) and 6.24(b) show the mesh and H^z scattered field for the 100λ model. The scattered width distributions with various approximation order are presented in Figure 6.25. Here, we see that the lower order approximations are far from convergence, with the accuracy improving significantly as the order is increased.

6.4.4 Computational Efficiency

To permit comparison with linear models on meshes of increased h-refinement, we return firstly to the 2λ NACA0012 aerofoil model. The meshes used in this analysis are indexed in Table 6.7, which states the number of points used in each mesh and the computational time needed to generate the solution. Note that the number of points contained in mesh n is equivalent to the number of points used in the n^{th} order approximation applied to the initial mesh displayed in Figure 6.20(a). For this 2λ model, the scattering width distributions, obtained by linear approximation on the various meshes, can be seen in Figure 6.26.

Convergence of the scattering width distributions as the refinement of the mesh is increased can be seen to occur at a slower rate than that obtained by raising the order. However, the difference is less significant than in previous models, due to the

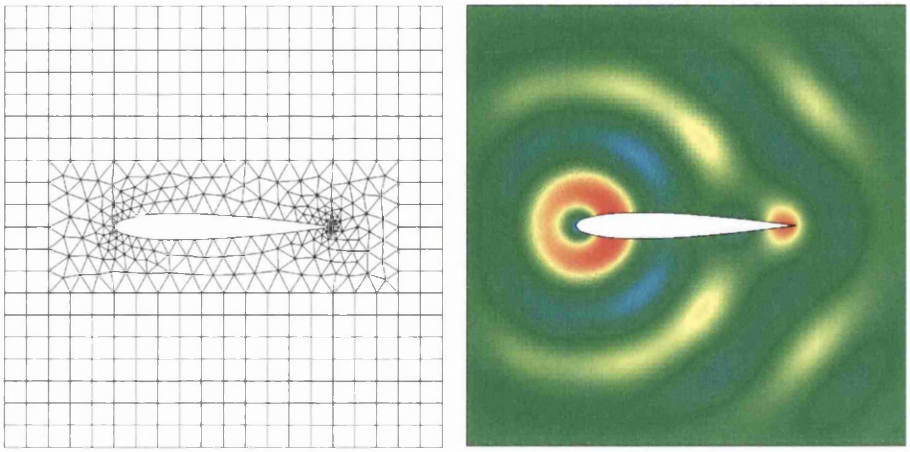

(a) (b)

Figure 6.20: 2λ PEC NACA0012 aerofoil in a TE^z polarized EM field (a) mesh (304 quadrilateral and 388 triangular elements) (b) H^z scattered field generated with fifth order elements

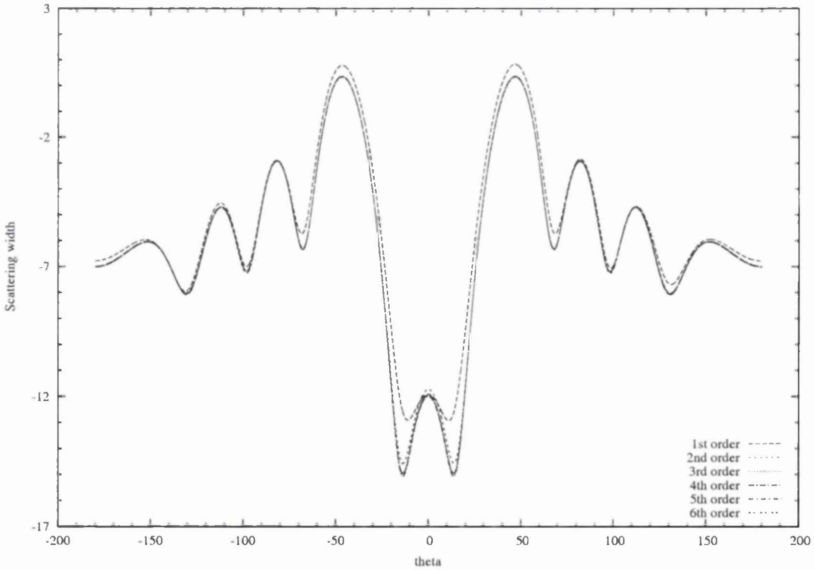

Figure 6.21: Scattering width distribution for a 2λ PEC NACA0012 aerofoil in a TE^z polarized EM field

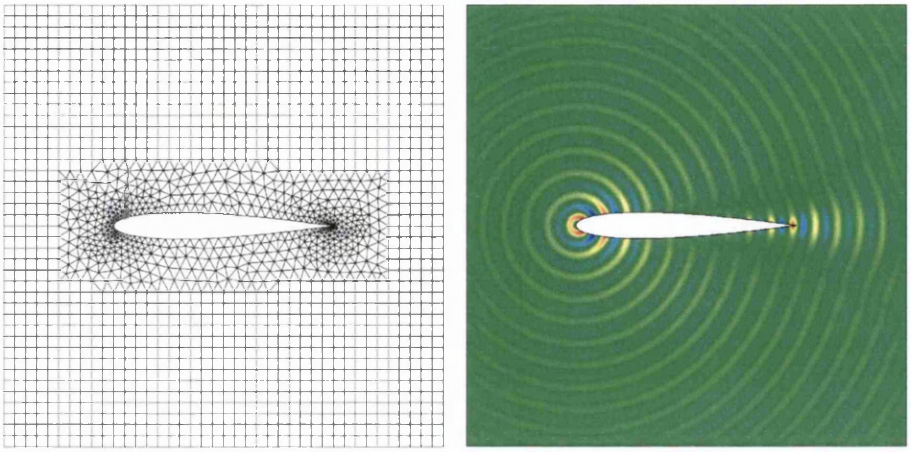

(a) (b)

Figure 6.22: 10λ PEC NACA0012 aerofoil in a TE^z polarized EM field (a) mesh (1266 quadrilateral and 1062 triangular elements) (b) H^z scattered field generated with fifth order elements

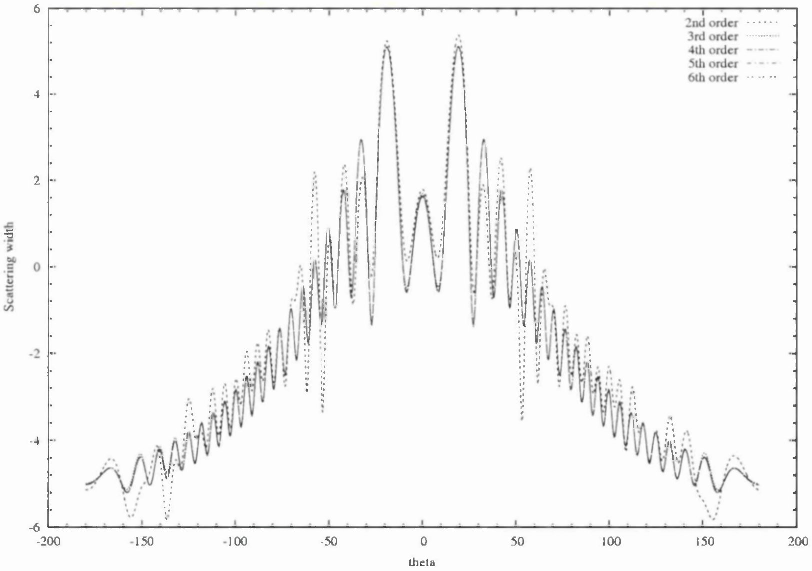

Figure 6.23: Scattering width distribution for a 10λ PEC NACA0012 aerofoil in a TE^z polarized EM field

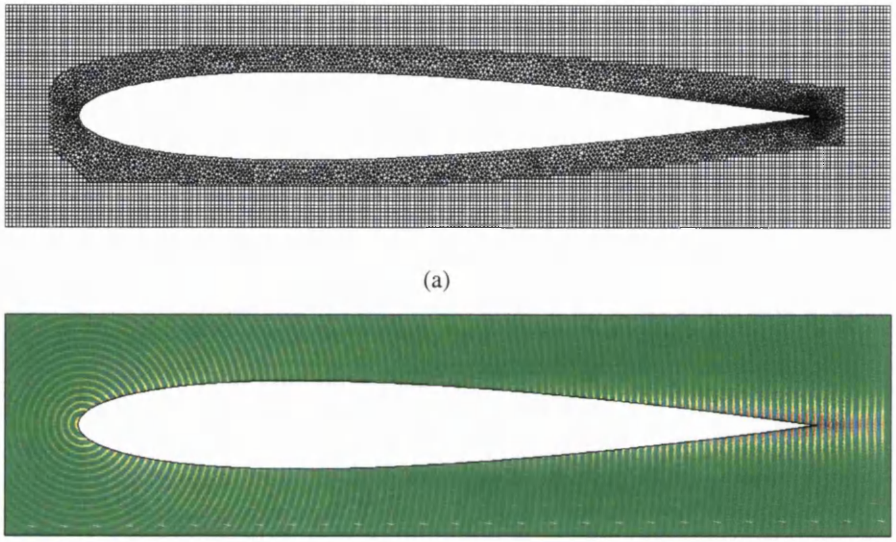
(a)

(b)

Figure 6.24: 100λ PEC NACA0012 aerofoil in a TE^z polarized EM field (a) mesh (7557 quadrilateral and 7852 triangular elements) (b) H^z scattered field generated with fifth order elements

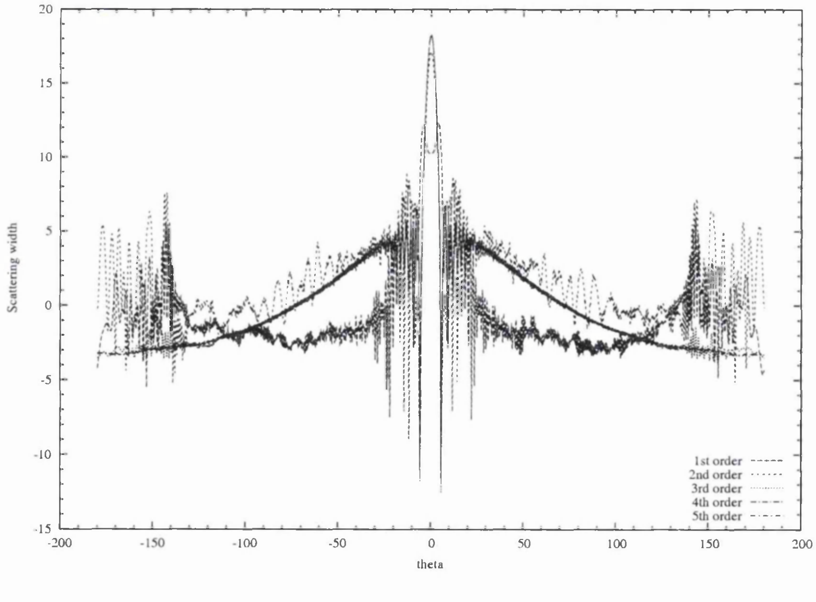

Figure 6.25: Scattering width distribution for a 100λ PEC NACA0012 aerofoil in a TE^z polarized EM field

Mesh	Number of points	CPU time (s)
1	558	1.51
2	1928	10.85
3	4214	35.46
4	7462	99.62
5	11211	178.31
6	16241	361.66

Table 6.7: Mesh index for 2λ NACA0012 aerofoil linear approximation comparison, with the number of points used in each mesh and the computational time required to generate the solution

initial level of discretisation, and both refinement strategies are near convergence by the third refinement.

Therefore, for a second linear comparison, let us use the 10λ NACA0012 aerofoil model. Again, the meshes are listed in Table 6.8 and the scattering width distributions generated on each mesh are displayed in Figure 6.27.

Mesh	Number of points	CPU time (s)
2	7349	83.48
3	16174	294.98
4	28828	746.97
5	43889	1588.22
6	63851	2891.06

Table 6.8: Mesh index for 10λ NACA0012 aerofoil linear approximation comparison, with the number of points used in each mesh and the computational time required to generate the solution

In this case, the convergence of the approximation using mesh refinement only can be seen to be inferior to that achieved by increasing the order of the elements. With linear approximation, Figure 6.27, the approximation only approaches convergence with mesh 4. In contrast, with p-refinement, Figure 6.23, the approximation is converged with a third order approximation and by comparison of the computational times found in Tables 6.8 and 6.6 respectively, the computational time ratio for these models is almost 5:1.

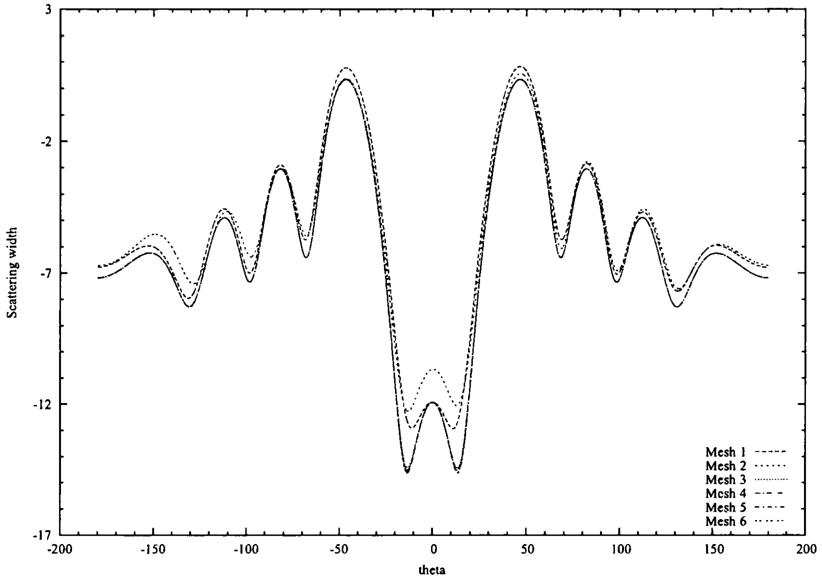

Figure 6.26: Scattering width distribution for a 2λ PEC NACA0012 aerofoil in a TE^z polarized EM field using linear approximation on various meshes

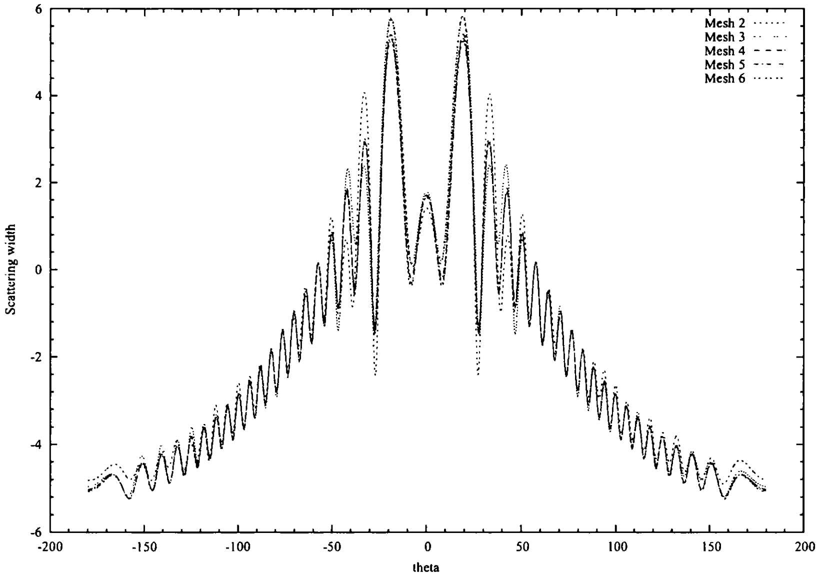

Figure 6.27: Scattering width distribution for a 10λ PEC NACA0012 aerofoil in a TE^z polarized EM field using linear approximation on various meshes

6.5 Multi Object Scattering Example

Another group of problems which may be of considerable interest is the wave fields generated by multiple scatterers. The interaction of waves propagating from the surfaces of two or more adjacent objects will produce intricate patterns which vary depending on numerous factors, including the relative size, shape, separation and orientation of the scattering geometries. Once again, the scope of such problems is vast. Hence, we will not begin an in-depth study of such models. However, we will present a simple example to introduce this set of problems and to indicate the possible application of this hybrid method for their approximation.

6.5.1 Scattering Model

The first wave scattering problem that was considered in this work, to permit the initial validation of the hybrid procedure, was that of a simple circular scatterer in Section 5.5. Now, as we move on to consider problems with multiple scattering objects, it is only natural to return to this simple geometry. Therefore, for this analysis, we will consider the simplest extension possible and examine the wave scattering generated by two adjacent circular objects.

The physical configuration of these circular objects can be seen in Figure 6.28, with the mesh used to discretise the surrounding space presented in Figure 6.29. The circular objects are identical and, placed within an incident TE^z polarized EM sinusoidal plane wave field of wavelength $\lambda = 2\pi$, propagating in the negative y direction, each has an electrical length of $(5/\pi)\lambda$.

Returning to the theory of the scattering width distribution, presented in Section 2.6, we recall that far field scattered solution values are needed to evaluate this quantity. To obtain these far field values, a surface S is needed upon which to apply a near to far field transformation. This surface S must enclose the scatterer. Hence, for the single object examples considered thus far, this surface was legitimately taken to coincide with the scattering surface. However, in the case of multi object scattering, this

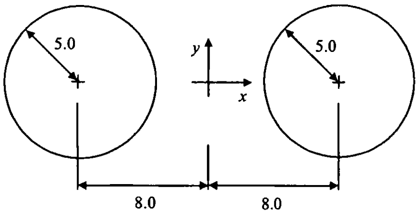

Figure 6.28: Multi object configuration (2 circles, each of electrical length $(5/\pi)\lambda$)

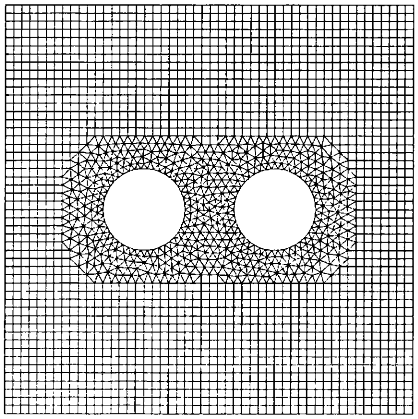

Figure 6.29: Multi object mesh (2 circles, each of electrical length $(5/\pi)\lambda$) with 1884 quadrilateral elements and 1046 triangular elements

is not a valid choice, as the surface must enclose every scattering surface. Therefore, for this example, the formulation has been changed and the surface S is taken to coincide with the hybrid mesh interface, which separates the quadrilateral and triangular parts of the mesh. As can be seen in Figure 6.29, this interface encloses both objects and, thus, is a suitable choice.

6.5.2 Results

Figure 6.30 displays examples of the magnetic H^z scattered and total wave fields for a TE^z polarized EM model. Similarly, the electric E^z scattered and total fields for a TM^z polarization can be seen in Figure 6.31. Both figures display results generated by a fifth order approximation applied to the mesh shown in Figure 6.29.

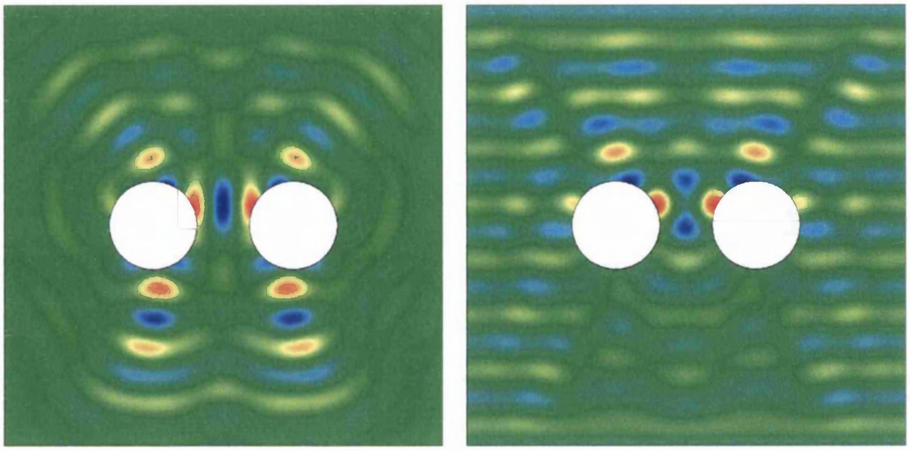

(a) (b)

Figure 6.30: H^z wave fields generated by two adjacent $(5/\pi)\lambda$ PEC circular scatterers placed in an incident TE^z EM field (a) Scattered field (b) Total field

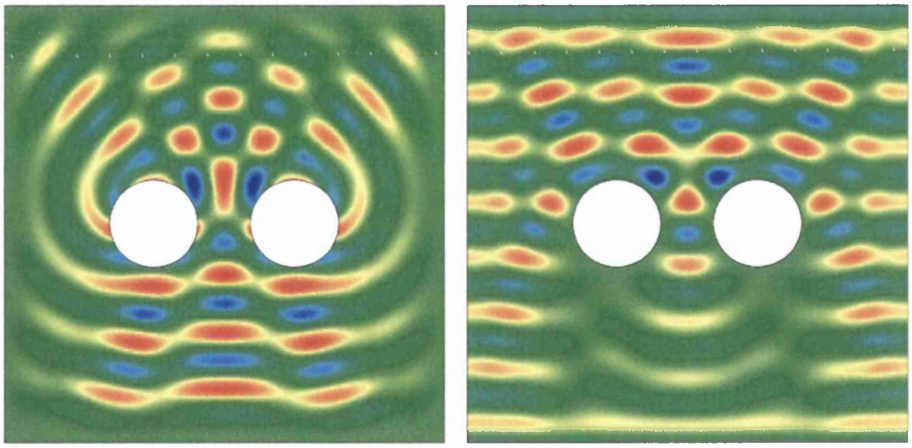

(a) (b)

Figure 6.31: E^z wave fields generated by two adjacent $(5/\pi)\lambda$ PEC circular scatterers placed in an incident TM^z EM field (a) Scattered field (b) Total field

Scattered width distributions for the TE^z and TM^z polarizations are presented in Figures 6.32 and 6.33 respectively. Convergence occurs in both cases and the scattering width distribution for the TM^z model compares well by visual inspection to that presented in [56].

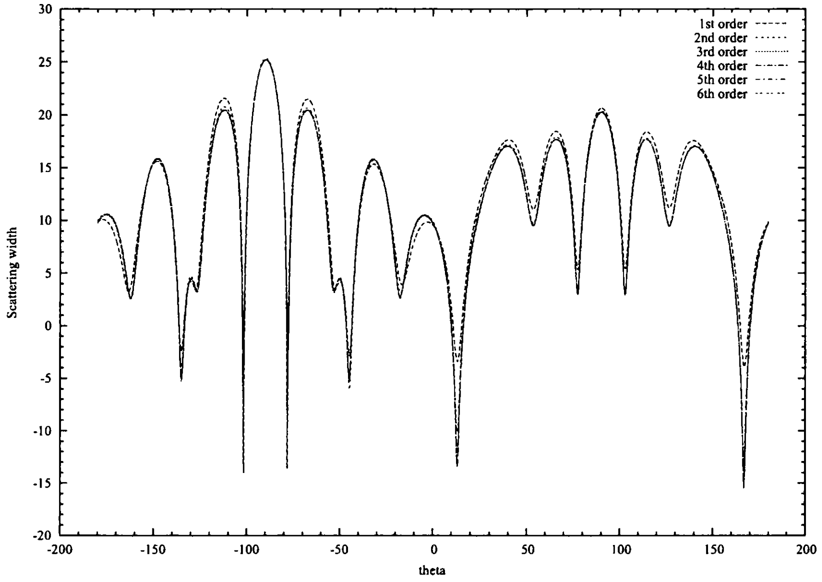

Figure 6.32: Scattering width distribution for two adjacent $(5/\pi)\lambda$ PEC circular scatterers, placed in a TE^z polarized EM field, using various approximation order

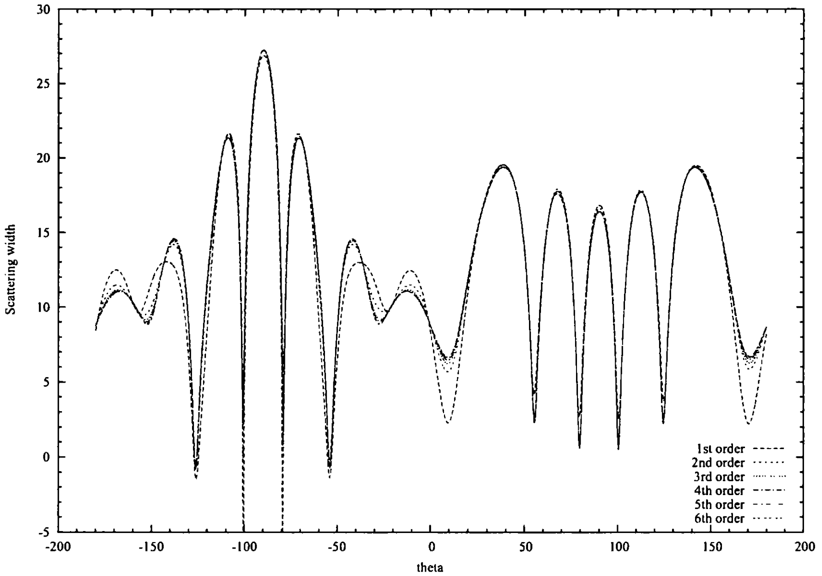

Figure 6.33: Scattering width distribution for two adjacent $(5/\pi)\lambda$ PEC circular scatterers, placed in a TM^z polarized EM field, using various approximation order

Increasing the complexity, the wave fields generated for a TE^z model by a shorter incident wavelength of $\lambda = 2.5$ units, giving each circular scatterer an electrical length of 4λ, can be seen in Figure 6.34. The scattering width distributions obtained with various approximation order are displayed in Figure 6.35 with the computational times taken to generate the solution presented in Table 6.9. This information will be used for comparison with the linear approximation discussed in the next section.

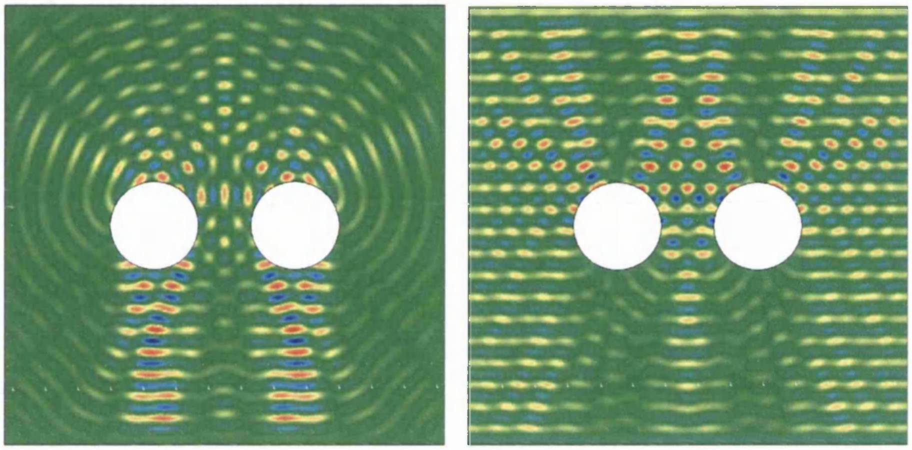

(a) (b)

Figure 6.34: H^z wave fields generated by two adjacent 4λ PEC circular scatterers placed in an incident TE^z EM field (a) Scattered field (b) Total field

Order	Number of points	CPU time (s)
1	2548	3.03
2	9911	12.35
3	22088	38.11
4	39079	253.49
5	60884	380.69
6	87503	16758.22

Table 6.9: Computational time taken with various approximation order to generate the solution for the multi object scattering model

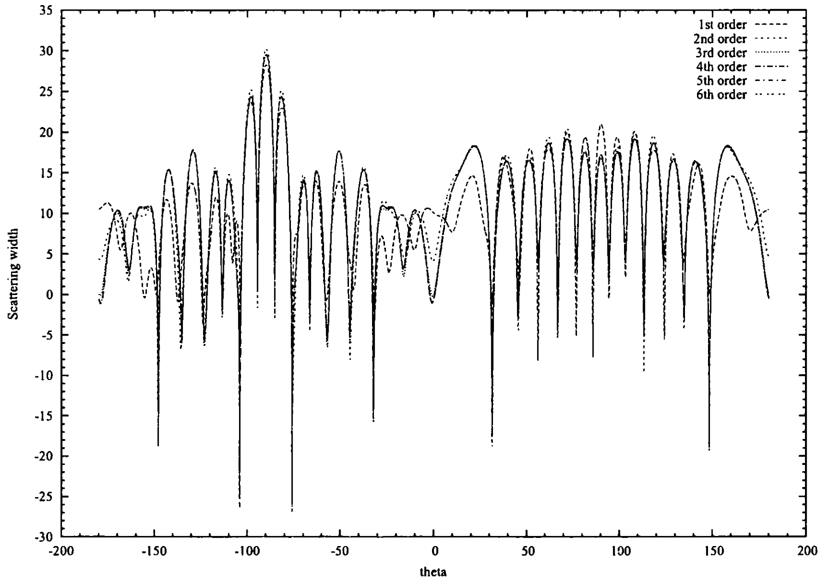

Figure 6.35: Scattering width distribution for two adjacent 4λ PEC circular scatterers, placed in a TE^z polarized EM field, using various approximation order

6.5.3 Computational Efficiency

The scattering width distributions generated by the two 4λ circular scatterers using linear approximation on meshes of various refinement can be seen in Figure 6.36. An index for the meshes used in this analysis, noting the number of points in each mesh and the computational time taken to obtain the approximation, can be found in Table 6.10.

Overall, the distributions do look reasonably similar. However, for certain viewing angles, for example $\theta = 0$, the improved convergence of the increasing order approximation can be seen as the distributions tend to a single line faster in Figure 6.35 than Figure 6.36. This may, in practical engineering terms, be viewed as only a subtle difference, but the simplicity of this example should be taken into consideration. For more complex problems, where the electrical length of the objects are increased significantly, the disparity between the accuracy of using p- and h-refinement should be more obvious.

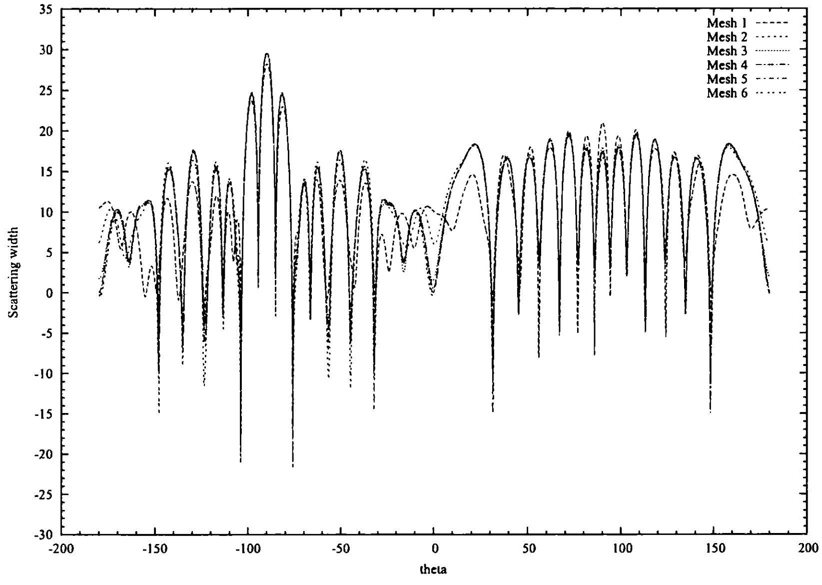

Figure 6.36: Scattering width distribution for two adjacent 4λ PEC circular scatterers, placed in a TE^z polarized EM field, using a linear approximation on meshes of various refinement

Mesh	Number of points	CPU time (s)
1	2548	3.03
2	9837	18.40
3	21941	59.15
4	38821	130.14
5	60518	291.54
6	96894	624.30

Table 6.10: Mesh index for multi object scattering model linear approximation comparison, with the number of points used in each mesh and the computational time required to generate the solution

6.6 Conclusion

In this chapter, we have analysed several examples of wave scattering problems. The complexity of these problems has been varied throughout to assess the computational procedure's ability to cope with various aspects of practical wave scattering models. These included the singularities of corner scatterers, first seen in the dihedral example of Section 6.2, and the high wavenumber fields of practical electromagnetics, as modelled with the NACA0012 aerofoil model in Section 6.4. In the first case, the dihedral model highlighted a limitation of the higher order approximation method in areas which contain singularities and demonstrated the need for increased mesh refinement to permit stable convergence as the order of the approximation was increased. On the other hand, the 100λ aerofoil model revealed the higher order procedures ability to resolve high wavenumber fields and thus produce scattering width distributions of reasonable accuracy. The final example of wave scattering from multiple bodies exhibited the procedures ability to handle effectively this type of problem.

Subsequently, the output obtained from the higher order approximation was compared with that generated by low order linear approximation on meshes of equivalent refinement. This facilitated the evaluation of both the accuracy and efficiency of the proposed higher order hybrid method when measured against a linear procedure. Favourable results were seen here demonstrating the increased convergence rates of higher order approximation and its ability to provide accurate solutions for problems with high wavenumber fields. As such, the main objective of the work has been achieved.

Chapter 7

Conclusions and Further Work

7.1 Conclusions

The purpose of this work was the development and analysis of a high-order solution procedure for temporal wave scattering problems in two spatial dimensions. Due to the requirements of the model, as explained in Chapter 1, it was essential that this method be capable of resolving high wavenumber scattered field patterns from complex surfaces in a time and memory efficient manner. To satisfy these contradictory criteria, a hybrid mesh method was put forward. This would comprise a triangular mesh discretisation in the vicinity of the scatterer and a quadrilateral discretisation beyond, extending to the truncated far field boundary.

The initially proposed method, as presented in Chapter 3, was a continuous Galerkin finite element approximation, incorporating the application of a mass iteration procedure to the triangular discretisation of the computational domain in an attempt to improve the accuracy of the solution on these triangular elements. However, having performed analyses with a higher order approximation, it became clear that the iteration was diverging. Consideration of the underlying formulation enabled a theoretical explanation to be made, showing that the instability was the result of an ill-conditioned iterative matrix. On the other hand, the properties of the quadrilateral formulation of the spectral element method (SEM) were deemed satisfactory and, accordingly, this aspect of the solution procedure was retained.

Therefore, an alternative method of solution for application to the triangular elements was sought. As discussed in Section 1.3, a popular method of approximation for time domain electromagnetic wave scattering problems is the discontinuous Galerkin method (DGM). Hence, application of this method to the triangular elements of the mesh was attempted. Due to the discontinuous nature of the scheme, inversion of a global mass matrix was avoided. This permitted the use of the full consistent mass matrix, ensuring that the accuracy of the approximation was maintained. Consequently, in Chapter 4, the use of a simple Gaussian pulse propagation test demonstrated the accuracy of this approximation and the potential for p-convergence.

Subsequently, both methods, a continuous Galerkin SEM approximation on the quadrilateral discretisation and a high order discontinuous Galerkin finite element approximation on the triangular discretisation, were coupled to form the proposed hybrid solution method. Following a simple convergence test, to see if the individual accuracy of the components of this method were retained in this coupled implementation, some initial wave scattering solutions were generated. The accuracy of these wave scattering solutions was also improved by separate studies on both the accuracy of the curved boundary representation and on an appropriate method to truncate the infinite physical domain. Convergence was clear in these models, with validation made possible due to the existence of an exact analytical solution. Furthermore, an initial assessment of the computational efficiency of higher order approximation when compared to low order linear methods demonstrated that significant time and memory reductions for wave scattering problems were possible.

Having performed these tests, the use of the method in a predictive context was assessed, analysing wave scattering problem where an exact analytical solution was unavailable. These problems included a dihedral object, a rectangular open cavity, a NACA0012 aerofoil geometry and a multi-scattering object example. Convergence with increasing element order was evident in each case and the improved efficiency of the higher order approximations was shown yet again. However, as was seen with the analysis of the first example, the dihedral object, stable convergence with increasing approximation order was only possible once a certain amount of h-refinement had been performed. In particular, it was found that the representation of the sharp corners of the geometry and small relative thickness of the dihedral legs had to be improved with an increase in element number. Only in this way would the high gradients in the solution be suitably resolved. It should be noted that this phenomenon would be less pronounced in the wave scattering examples involving circular objects due to the smoothness of the solution.

Nonetheless, it is therefore considered that this research work has succeeded in its intention to show the benefits of a higher order finite element approximation for the solution of wave scattering problems.

7.2 Further Work

With the development of this numerical procedure, we have obtained a means by which computational solutions to wave scattering problems can be generated. For the two-dimensional examples presented in this work, their high order solutions were shown to be achieved in a more efficient manner than using a low order linear approximation. As such, it was concluded above that the main objective of this work has been reached. However, there are numerous aspects of the model which could be modified and various further wave scattering problems for which to attempt an approximation. In this section, we will endeavour to give a brief discussion of these possible extensions to the work.

To begin this discussion, we will firstly consider the manner with which the order of approximation is defined for problem solution. At present, the approximation order applied to every part of the computational domain is constant. However, this need not be the case. In the limit, due to the incorporation of a discontinuous Galerkin method, the scheme could quite possibly be modified to use different orders of approximation on each of these elements. However, before discussing this, it would be worthwhile returning to the spectral element method of Chapter 3. In this chapter, it was concluded that the iterative procedure, intended to improve the solution on the triangular elements, was not fit for purpose. Consequently, the application of a continuous Galerkin approximation on this part of the mesh was abandoned, leading to the use of a discontinuous Galerkin method, as seen in Chapter 4. To clarify this, the attempted use of both the iterative scheme and the discontinuous Galerkin method were driven by the initial inaccuracy of the triangular formulation of the SEM when compared to the same order of approximation with a quadrilateral formulation, as noted in Section 3.5. Therefore, a possible alternative treatment could involve the application of a higher order continuous Galerkin approximation to the triangular part of the mesh than applied to the quadrilateral part. For example, if the approximation on the quadrilateral elements was of n^{th} order, then the approximation order on the triangular elements would be $n + 1$. In this way, a diagonal mass matrix continuous SEM would be applied to every part of the mesh, with the order of approximation as defined above. This would be an alternative method with which to attempt to achieve the objectives of accuracy and efficiency. It should be noted that a method of coupling the solutions, possibly similar to that discussed in Section 5.2.4 with an interpolation method to obtain the solution on coincident boundary points, would be required.

Returning to the chosen hybrid method, it may prove advantageous to attempt the opposite of that recommended above and apply a higher order SEM to the quadrilateral part of the mesh than the corresponding order of the spectral DGM applied to the triangular elements. This may reduce the dispersion error associated with the diagonal SEM as the scattered waves propagate beyond the unstructured mesh. However, the benefit of this formulation may only be significant for low order approximations.

Leaving the field of electromagnetics and returning to the derivation of the acoustic wave equations from the governing equations of fluid flow, as performed in Section 2.2, we recall that a simplification that was made involved the assumption of a zero or quiescent background flow through which the waves would propagate. It may be of interest to attempt to incorporate an option for a certain background flow component within the approximation, such as would be encountered in the field of aeroacoustics. This would increase the generality of the method, thus encompassing a greater field of research.

Another obvious candidate for further work would be the reformulation of the method to enable approximation of wave scattering problems in three spatial dimensions. This would permit the full analysis of real practical scattering geometries. Although requiring both increased computational time and memory, it would be hoped that the efficiency of the high order approximation, seen in this work, would extend to this enlarged solution space, thus offering a realistic means of approximation. Additionally, it would be of considerable interest to practical modelling applications to permit the analysis of an increased range of problems including, for example in the electromagnetics field, penetrable media and dielectric scatterers.

Finally, the inevitable increase in computational work required to incorporate the modelling aspects suggested above could be offset by the use of parallel computing. The popularity of this procedure has grown in recent times and its application to this work might be a worthwhile consideration. The use of the discontinuous Galerkin method lends itself to such a technique as does the coupled mesh nature of the method.

Appendix A

Analysis of Iterative Matrix

A.1 Introduction

As further clarification of the divergence of the iterative procedure introduced in Chapter 3, this discussion presents theoretically the condition for stability of the iterative matrix. Subsequently, it is shown that the corresponding iterative matrix for third element order does meet this condition, but fourth element order does not.

A.2 Stability Condition

To begin the derivation of the stability condition, we recall that the iterative equation (3.31) can be expressed as

$$\boldsymbol{U}^{n+1(r+1)} = \boldsymbol{M}_L^{-1}\boldsymbol{R}^n - \boldsymbol{B}\boldsymbol{U}^{n+1(r)} \tag{A.1}$$

where the iterative matrix $\boldsymbol{B}$ is

$$\boldsymbol{B} = \boldsymbol{M}_L^{-1}(\boldsymbol{M} - \boldsymbol{M}_L) \tag{A.2}$$

From linear algebra, we know that any vector $\boldsymbol{x}$ can be expressed as a weighted average of the eigenvectors $\boldsymbol{x}_j$ of the mathematical space under consideration [57]

$$\boldsymbol{x} = \sum_{j=1}^{n} a_j \boldsymbol{x}_j \tag{A.3}$$

Therefore, equation (A.1), omitting the time-level superscript $n+1$ for convenience, can be rewritten in terms of the eigenvectors of the mathematical solution space as

$$\boldsymbol{U}^{(r+1)} = \boldsymbol{M}_L^{-1}\boldsymbol{R}^n - \sum_{j+1}^{n} a_j \boldsymbol{B}\boldsymbol{U}_j^{(r)} \tag{A.4}$$

Furthermore, due to eigenvector theory, this can be further manipulated and written in terms of the eigenvalues λ_j of the matrix $\boldsymbol{B}$

$$\boldsymbol{U}^{(r+1)} = \boldsymbol{M}_L^{-1}\boldsymbol{R}^n - \sum_{j+1}^{n} a_j \lambda_j \boldsymbol{U}_j^{(r)} \tag{A.5}$$

Now, we assume that the initial iteration can be written as

$$\boldsymbol{U}^{(1)} = \boldsymbol{M}_L^{-1}\boldsymbol{R}^n - \sum_{j+1}^{n} a_j \lambda_j \boldsymbol{U}_j \tag{A.6}$$

Subsequently, the second iteration can be expressed in terms of this first solution by substituting (A.6) back into (A.1), thus giving

$$\boldsymbol{U}^{(2)} = \boldsymbol{M}_L^{-1}\boldsymbol{R}^n - \boldsymbol{B}\boldsymbol{M}_L^{-1}\boldsymbol{R}^n + \sum_{j+1}^{n} a_j \lambda_j^2 \boldsymbol{U}_j \tag{A.7}$$

Extending this repetition to the m^{th} iteration, the final term in the iterative equation will be

$$\boldsymbol{U}^{(m)} = \ldots + \sum_{j+1}^{n} a_j \lambda_j^m \boldsymbol{U}_j \tag{A.8}$$

Consequently, it can be seen that if any of the eigenvalues λ_j of the matrix $\boldsymbol{B}$ are greater than unity this term will increase exponentially, causing the solution to diverge.

A.3 Eigenvalue Computation for Higher Order Elements

Having derived the condition for stability, we will now compute the eigenvalues of the iterative matrix produced for the third and fourth order elements.

A.3.1 Third Order

For third order triangular elements, the components of the consistent M and lumped M_L mass matrices are:

Consistent Mass Matrix for Third Order Triangular Element

$$
\boldsymbol{M} = \begin{bmatrix}
0.0230 & -0.0084 & 0.0005 & 0.0012 & -0.0084 & 0.0000 & 0.0119 & 0.0005 & 0.0119 & 0.0012 \\
-0.0084 & 0.1389 & -0.0099 & 0.0005 & 0.0642 & 0.0536 & -0.0298 & -0.0298 & -0.0245 & 0.0119 \\
0.0005 & -0.0099 & 0.1389 & -0.0084 & -0.0298 & 0.0536 & 0.0642 & -0.0245 & -0.0298 & 0.0119 \\
0.0012 & 0.0005 & -0.0084 & 0.0230 & 0.0119 & 0.0000 & -0.0084 & 0.0119 & 0.0005 & 0.0012 \\
-0.0084 & 0.0642 & -0.0298 & 0.0119 & 0.1389 & 0.0536 & -0.0245 & -0.0099 & -0.0298 & 0.0005 \\
0.0000 & 0.0536 & 0.0536 & 0.0000 & 0.0536 & 0.5786 & 0.0536 & 0.0536 & 0.0536 & 0.0000 \\
0.0119 & -0.0298 & 0.0642 & -0.0084 & -0.0245 & 0.0536 & 0.1389 & -0.0298 & -0.0099 & 0.0005 \\
0.0005 & -0.0298 & -0.0245 & 0.0119 & -0.0099 & 0.0536 & -0.0298 & 0.1389 & 0.0642 & -0.0084 \\
0.0119 & -0.0245 & -0.0298 & 0.0005 & -0.0298 & 0.0536 & -0.0099 & 0.0642 & 0.1389 & -0.0084 \\
0.0012 & 0.0119 & 0.0119 & 0.0012 & 0.0005 & 0.0000 & 0.0005 & -0.0084 & -0.0084 & 0.0230
\end{bmatrix}
$$

Lumped Mass Matrix for Third Order Triangular Element

$$
\boldsymbol{M_L} = \begin{bmatrix}
0.0333 & 0.0000 & 0.0000 & 0.0000 & 0.0000 & 0.0000 & 0.0000 & 0.0000 & 0.0000 & 0.0000 \\
0.0000 & 0.1667 & 0.0000 & 0.0000 & 0.0000 & 0.0000 & 0.0000 & 0.0000 & 0.0000 & 0.0000 \\
0.0000 & 0.0000 & 0.1667 & 0.0000 & 0.0000 & 0.0000 & 0.0000 & 0.0000 & 0.0000 & 0.0000 \\
0.0000 & 0.0000 & 0.0000 & 0.0333 & 0.0000 & 0.0000 & 0.0000 & 0.0000 & 0.0000 & 0.0000 \\
0.0000 & 0.0000 & 0.0000 & 0.0000 & 0.1667 & 0.0000 & 0.0000 & 0.0000 & 0.0000 & 0.0000 \\
0.0000 & 0.0000 & 0.0000 & 0.0000 & 0.0000 & 0.9000 & 0.0000 & 0.0000 & 0.0000 & 0.0000 \\
0.0000 & 0.0000 & 0.0000 & 0.0000 & 0.0000 & 0.0000 & 0.1667 & 0.0000 & 0.0000 & 0.0000 \\
0.0000 & 0.0000 & 0.0000 & 0.0000 & 0.0000 & 0.0000 & 0.0000 & 0.1667 & 0.0000 & 0.0000 \\
0.0000 & 0.0000 & 0.0000 & 0.0000 & 0.0000 & 0.0000 & 0.0000 & 0.0000 & 0.1667 & 0.0000 \\
0.0000 & 0.0000 & 0.0000 & 0.0000 & 0.0000 & 0.0000 & 0.0000 & 0.0000 & 0.0000 & 0.0333
\end{bmatrix}
$$

Inserting these expressions into (A.2), the eigenvalues of the matrix $\boldsymbol{B}$ can be computed to be

$$
\lambda = \begin{pmatrix}
-0.6966 \\
-0.6197 \\
0.0003 \\
-0.2436 \\
0.5982 \\
0.5982 \\
-0.2999 \\
-0.2999 \\
-0.6197 \\
-0.7031
\end{pmatrix}
$$

As the magnitude of each eigenvalue λ_j is less than unity, then the iteration is stable and will converge. Note that these eigenvalues can be computed by using the intrinsic functions of a mathematical computer program such as *Matlab*, as was used here, or *Mathematica*.

A.3.2 Fourth Order

For fourth order triangular elements, the components of the consistent $\boldsymbol{M}$ and lumped $\boldsymbol{M}_L$ mass matrices are:

Consistent Mass Matrix for Fourth Order Triangular Element

$$M = \begin{bmatrix}
0.0109 & -0.0066 & 0.0034 & 0.0001 & -0.0004 & -0.0066 & 0.0107 & 0.0012 & -0.0033 & 0.0034 & 0.0012 & -0.0069 & 0.0001 & -0.0033 & -0.0004 \\
-0.0066 & 0.0625 & -0.0096 & 0.0016 & 0.0001 & 0.0281 & 0.0051 & -0.0065 & 0.0085 & -0.0161 & -0.0095 & 0.0115 & 0.0085 & 0.0044 & -0.0033 \\
0.0034 & -0.0096 & 0.0836 & -0.0096 & 0.0034 & -0.0161 & 0.0400 & 0.0400 & -0.0161 & -0.0097 & -0.0278 & -0.0097 & 0.0115 & 0.0115 & -0.0069 \\
0.0001 & 0.0016 & -0.0096 & 0.0625 & -0.0066 & 0.0085 & -0.0065 & 0.0051 & 0.0281 & 0.0115 & -0.0095 & -0.0161 & 0.0044 & 0.0085 & -0.0033 \\
-0.0004 & 0.0001 & 0.0034 & -0.0066 & 0.0109 & -0.0033 & 0.0012 & 0.0107 & -0.0066 & -0.0069 & 0.0012 & 0.0034 & -0.0033 & 0.0001 & -0.0004 \\
-0.0066 & 0.0281 & -0.0161 & 0.0085 & -0.0033 & 0.0625 & 0.0051 & -0.0095 & 0.0044 & -0.0096 & -0.0065 & 0.0115 & 0.0016 & 0.0085 & 0.0001 \\
0.0107 & 0.0051 & 0.0400 & -0.0065 & 0.0012 & 0.0051 & 0.3281 & 0.0231 & -0.0095 & 0.0400 & 0.0231 & -0.0278 & -0.0065 & -0.0095 & 0.0012 \\
0.0012 & -0.0065 & 0.0400 & 0.0051 & 0.0107 & -0.0095 & 0.0231 & 0.3281 & 0.0051 & -0.0278 & 0.0231 & 0.0400 & -0.0095 & -0.0065 & 0.0012 \\
-0.0033 & 0.0085 & -0.0161 & 0.0281 & -0.0066 & 0.0044 & -0.0095 & 0.0051 & 0.0625 & 0.0115 & -0.0065 & -0.0096 & 0.0085 & 0.0016 & 0.0001 \\
0.0034 & -0.0161 & -0.0097 & 0.0115 & -0.0069 & -0.0096 & 0.0400 & -0.0278 & 0.0115 & 0.0836 & 0.0400 & -0.0097 & -0.0096 & -0.0161 & 0.0034 \\
0.0012 & -0.0095 & -0.0278 & -0.0095 & 0.0012 & -0.0065 & 0.0231 & 0.0231 & -0.0065 & 0.0400 & 0.3281 & 0.0400 & 0.0051 & 0.0051 & 0.0107 \\
-0.0069 & 0.0115 & -0.0097 & -0.0161 & 0.0034 & 0.0115 & -0.0278 & 0.0400 & -0.0096 & -0.0097 & 0.0400 & 0.0836 & -0.0161 & -0.0096 & 0.0034 \\
0.0001 & 0.0085 & 0.0115 & 0.0044 & -0.0033 & 0.0016 & -0.0065 & -0.0095 & 0.0085 & -0.0096 & 0.0051 & -0.0161 & 0.0625 & 0.0281 & -0.0066 \\
-0.0033 & 0.0044 & 0.0115 & 0.0085 & 0.0001 & 0.0085 & -0.0095 & -0.0065 & 0.0016 & -0.0161 & 0.0051 & -0.0096 & 0.0281 & 0.0625 & -0.0066 \\
-0.0004 & -0.0033 & -0.0069 & -0.0033 & -0.0004 & 0.0001 & 0.0012 & 0.0012 & 0.0001 & 0.0034 & 0.0107 & 0.0034 & -0.0066 & -0.0066 & 0.0109
\end{bmatrix}$$

Lumped Mass Matrix for Fourth Order Triangular Element

$$M_L = \begin{bmatrix}
0.0035 & 0.0000 & 0.0000 & 0.0000 & 0.0000 & 0.0000 & 0.0000 & 0.0000 & 0.0000 & 0.0000 & 0.0000 & 0.0000 & 0.0000 & 0.0000 & 0.0000 \\
0.0000 & 0.0786 & 0.0000 & 0.0000 & 0.0000 & 0.0000 & 0.0000 & 0.0000 & 0.0000 & 0.0000 & 0.0000 & 0.0000 & 0.0000 & 0.0000 & 0.0000 \\
0.0000 & 0.0000 & 0.0880 & 0.0000 & 0.0000 & 0.0000 & 0.0000 & 0.0000 & 0.0000 & 0.0000 & 0.0000 & 0.0000 & 0.0000 & 0.0000 & 0.0000 \\
0.0000 & 0.0000 & 0.0000 & 0.0786 & 0.0000 & 0.0000 & 0.0000 & 0.0000 & 0.0000 & 0.0000 & 0.0000 & 0.0000 & 0.0000 & 0.0000 & 0.0000 \\
0.0000 & 0.0000 & 0.0000 & 0.0000 & 0.0035 & 0.0000 & 0.0000 & 0.0000 & 0.0000 & 0.0000 & 0.0000 & 0.0000 & 0.0000 & 0.0000 & 0.0000 \\
0.0000 & 0.0000 & 0.0000 & 0.0000 & 0.0000 & 0.0786 & 0.0000 & 0.0000 & 0.0000 & 0.0000 & 0.0000 & 0.0000 & 0.0000 & 0.0000 & 0.0000 \\
0.0000 & 0.0000 & 0.0000 & 0.0000 & 0.0000 & 0.0000 & 0.4180 & 0.0000 & 0.0000 & 0.0000 & 0.0000 & 0.0000 & 0.0000 & 0.0000 & 0.0000 \\
0.0000 & 0.0000 & 0.0000 & 0.0000 & 0.0000 & 0.0000 & 0.0000 & 0.4180 & 0.0000 & 0.0000 & 0.0000 & 0.0000 & 0.0000 & 0.0000 & 0.0000 \\
0.0000 & 0.0000 & 0.0000 & 0.0000 & 0.0000 & 0.0000 & 0.0000 & 0.0000 & 0.0786 & 0.0000 & 0.0000 & 0.0000 & 0.0000 & 0.0000 & 0.0000 \\
0.0000 & 0.0000 & 0.0000 & 0.0000 & 0.0000 & 0.0000 & 0.0000 & 0.0000 & 0.0000 & 0.0880 & 0.0000 & 0.0000 & 0.0000 & 0.0000 & 0.0000 \\
0.0000 & 0.0000 & 0.0000 & 0.0000 & 0.0000 & 0.0000 & 0.0000 & 0.0000 & 0.0000 & 0.0000 & 0.4180 & 0.0000 & 0.0000 & 0.0000 & 0.0000 \\
0.0000 & 0.0000 & 0.0000 & 0.0000 & 0.0000 & 0.0000 & 0.0000 & 0.0000 & 0.0000 & 0.0000 & 0.0000 & 0.0880 & 0.0000 & 0.0000 & 0.0000 \\
0.0000 & 0.0000 & 0.0000 & 0.0000 & 0.0000 & 0.0000 & 0.0000 & 0.0000 & 0.0000 & 0.0000 & 0.0000 & 0.0000 & 0.0786 & 0.0000 & 0.0000 \\
0.0000 & 0.0000 & 0.0000 & 0.0000 & 0.0000 & 0.0000 & 0.0000 & 0.0000 & 0.0000 & 0.0000 & 0.0000 & 0.0000 & 0.0000 & 0.0786 & 0.0000 \\
0.0000 & 0.0000 & 0.0000 & 0.0000 & 0.0000 & 0.0000 & 0.0000 & 0.0000 & 0.0000 & 0.0000 & 0.0000 & 0.0000 & 0.0000 & 0.0000 & 0.0035
\end{bmatrix}$$

Inserting these expressions into (A.2), the eigenvalues of the matrix $\boldsymbol{B}$ can be computed to be

$$\lambda = \begin{pmatrix} 2.3252 \\ 2.5425 \\ 2.5425 \\ -0.5547 \\ 0.1857 \\ -0.0002 \\ -0.6882 \\ -0.6882 \\ -0.6281 \\ -0.6281 \\ -0.4224 \\ 0.2123 \\ 0.2123 \\ -0.0460 \\ -0.0460 \end{pmatrix}$$

Here we can see that the magnitude of some of the eigenvalues is greater than unity. Therefore, noting the stability condition derived above, this will result in an unstable diverging iterative scheme.

A.3.3 Fifth Order and Higher

Using the same procedure, the iterative matrix for fifth element order and higher can also be shown not to satisfy the stability condition, thus leading to divergent iterative schemes. However, this analysis is not performed here.

Appendix B

Runge-Kutta Temporal Schemes

B.1 Introduction

The Runge-Kutta family of temporal schemes are very popular within the scientific and engineering fields for the solution of ordinary differential equations. In summary, they involve the computation of intermediate solutions within a time-step which are subsequently used to compute the solution at the next full time level.

B.2 Fourth Order Runge-Kutta Scheme (RK4)

The most commonly used scheme from this family is the fourth order Runge-Kutta scheme (RK4), which consists of four sub-steps. Each of these calculates an intermediate solution value which is used to evaluate the final solution at the next time level. Considering a general differential equation

$$\frac{du}{dt} = f(t, u) \tag{B.1}$$

the equations of the RK4 scheme can be written as

$$\begin{aligned}
1^{st}\text{ step:}\quad & k_1 = \Delta t f(t^n, u^n) \\
2^{nd}\text{ step:}\quad & k_2 = \Delta t f(t^{n+\frac{1}{2}}, u^n + \tfrac{1}{2}k_1) \\
3^{rd}\text{ step:}\quad & k_3 = \Delta t f(t^{n+\frac{1}{2}}, u^n + \tfrac{1}{2}k_2) \\
4^{th}\text{ step:}\quad & k_4 = \Delta t f(t^{n+1}, u^n + k_3)
\end{aligned}$$

$$u^{n+1} = u^n + \frac{1}{6}k_1 + \frac{1}{3}k_2 + \frac{1}{3}k_3 + \frac{1}{6}k_4 + O(\Delta t^5) \tag{B.2}$$

B.3 Spatial Discretisation

Before we can apply the RK4 scheme, we must first obtain the spatially semi-discrete form of the governing equations. Note that this is contrary to the derivation of the discretised equations for the Taylor-Galerkin schemes where spatial discretisation follows the temporal approximation. Therefore, beginning with the governing acoustic equations in vector form

$$\frac{\partial \boldsymbol{U}}{\partial t} + \frac{\partial \boldsymbol{F}}{\partial x} + \frac{\partial \boldsymbol{G}}{\partial y} = 0 \tag{B.3}$$

we can express the weighted residual statement as

$$\int_\Omega \frac{\partial \hat{\boldsymbol{U}}}{\partial t} N_I d\Omega = -\int_\Omega \left(\frac{\partial \boldsymbol{F}}{\partial x} + \frac{\partial \boldsymbol{G}}{\partial y} \right) N_I d\Omega \tag{B.4}$$

As seen in Chapter 3, we choose to write the differential terms on the RHS of the equation in terms of the unknown vector $\boldsymbol{U}$ by using the system Jacobians $\boldsymbol{A} = \partial \boldsymbol{F} / \partial \boldsymbol{U}$ and $\boldsymbol{B} = \partial \boldsymbol{G} / \partial \boldsymbol{U}$

$$\int_\Omega \frac{\partial \hat{\boldsymbol{U}}}{\partial t} N_I d\Omega = -\int_\Omega \left(\boldsymbol{A} \frac{\partial \hat{\boldsymbol{U}}}{\partial x} + \boldsymbol{B} \frac{\partial \hat{\boldsymbol{U}}}{\partial y} \right) N_I d\Omega$$

As is the norm for finite element approximations, we now apply integration-by-parts to the spatial derivatives

$$\int_\Omega \frac{\partial \hat{\boldsymbol{U}}}{\partial t} N_I d\Omega = \int_\Omega \left(\boldsymbol{A} \frac{\partial N_I}{\partial x} \hat{\boldsymbol{U}} + \boldsymbol{B} \frac{\partial N_I}{\partial y} \hat{\boldsymbol{U}} \right) d\Omega - \int_\Gamma \left(n_x \boldsymbol{A} \hat{\boldsymbol{U}} + n_y \boldsymbol{B} \hat{\boldsymbol{U}} \right) N_I d\Gamma$$

It should be noted that although this transformation is not needed here to reduce inter-element continuity constraints for the interpolation functions N due to the absence of higher order derivative terms, there are other reasons for its inclusion: to enable local conservation to be proved and, due to the generation of an additional boundary integral, to provide a convenient means by which boundary conditions can be applied.

Finally, insertion of the finite element approximation of the unknown vector

$$\hat{\boldsymbol{U}} = N_J \boldsymbol{U}_J$$

enables the semi-discrete form of the governing equations to be expressed as

$$M_{IJ} \frac{\partial \boldsymbol{U}_J}{\partial t} = C_{IJ} \boldsymbol{U}_J + f_I \tag{B.5}$$

where

$$\begin{aligned} M_{IJ} &= \int_\Omega N_I N_J \, d\Omega \\ C_{IJ} &= \int_\Omega (\boldsymbol{A} \frac{\partial N_I}{\partial x} N_J + \boldsymbol{B} \frac{\partial N_I}{\partial y} N_J) \, d\Omega \\ f_I &= -\int_\Gamma (n_x \boldsymbol{A} N_I N_J + n_y \boldsymbol{B} N_I N_J) \, d\Gamma \boldsymbol{U}_J \end{aligned}$$

B.4 Temporal Discretisation

To obtain the fully discrete form of the equations, the RK4 scheme can now be directly applied to (B.5). Therefore, the equations of the scheme can be expressed as

$$\begin{aligned} &1^{st} \text{ step:} \quad k_1 = \Delta t M_{IJ}^{-1} [C_{IJ} \boldsymbol{U}_J^n + f_I^n] \\ &2^{nd} \text{ step:} \quad k_2 = \Delta t M_{IJ}^{-1} [C_{IJ} (\boldsymbol{U}_J^n + \tfrac{1}{2} k_1) + f_I^{n+\frac{1}{2}}] \\ &3^{rd} \text{ step:} \quad k_3 = \Delta t M_{IJ}^{-1} [C_{IJ} (\boldsymbol{U}_J^n + \tfrac{1}{2} k_2) + f_I^{n+\frac{1}{2}}] \\ &4^{th} \text{ step:} \quad k_4 = \Delta t M_{IJ}^{-1} [C_{IJ} (\boldsymbol{U}_J^n + k_3) + f_I^{n+1}] \end{aligned}$$

$$\boldsymbol{U}^{n+1} = \boldsymbol{U}^n + \frac{1}{6} k_1 + \frac{1}{3} k_2 + \frac{1}{3} k_3 + \frac{1}{6} k_4 \tag{B.6}$$

Appendix C

PML Analysis

C.1 Introduction

Due to the infinite nature of the physical domains for the wave scattering problems encountered in this work, some form of truncation is needed to enable a computational model to be generated. This is achieved by introducing an artificial outer boundary to the domain. However, to avoid spurious wave reflection from this surface, some form of transmitting or absorbing condition must be applied and, in Section 5.4, a perfectly matched layer (PML) was proposed.

Within the formulation of this layer some variable parameters exist which may alter its absorbing performance. These parameters include the minimum distance from the scattering surface to the PML, the thickness of the PML, the maximum value of the damping coefficient σ and its distribution across the absorbing layer. Therefore, in this appendix, a brief analysis is presented to demonstrate the effects of the variation of these four parameters and to evaluate some appropriate values. Note that this is by no means intended to be an in-depth study of the effects of each parameter, but provides an initial test to assess the working range of the PML.

C.2 Model

To provide an appropriate method of validation, we will employ a model of a simple circular scatterer for which an analytical solution exists. The scatterer will be an acoustically hard object with a radius of 2 units placed in a incident sinusoidal plane wave field, as expressed in equation (5.20), of unit wavelength λ. In an electromagnetic context, this is equivalent to a transverse electric (TE^z) polarization of the electromagnetic field with scattering from a perfectly electrical conducting object of electrical length 4λ.

The basic mesh used in this analysis is presented in Figure C.1. It consists of 1012 triangular elements, which directly surround the scatterer, and 8164 quadrilateral elements.

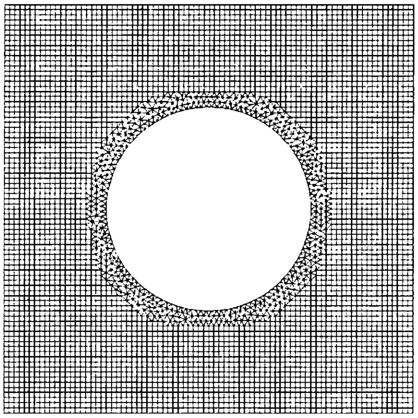

Figure C.1: Circular scatterer mesh used for PML analysis

In an attempt to ensure fairness, only one parameter will be varied in each test. The remaining three parameters will be constant to focus on the effect on the approximate solution generated by the variation of the parameter in question. Therefore, it should be noted that, due to the nature of the first test, concerning the minimum distance from the scattering surface to the PML, the extent of the mesh will be increased or reduced as required from that displayed in Figure C.1. In the remaining tests, the mesh will be constant.

Due to the use of higher order approximation, the PML parameter analysis will be conducted on models of both first and third order elements. This will indicate whether a significant difference is required in the value of the parameters for different element orders.

C.3 Results

C.3.1 First Order Element Approximation

The first order element models show no significant trend in the accuracy of the solution over the range of distances from the scattering surface to the PML used in the first test, the results of which can be seen in Table C.1. From Table C.2, it can be seen that the error begins to increase for PML thicknesses below 0.5λ.

Domain Size	Minimum Distance	E_Γ
9.5x9.5	2λ	0.01849939
9x9	1.75λ	0.01764371
8.5x8.5	1.5λ	0.01851132
8x8	1.25λ	0.01763899
7.5x7.5	1.0λ	0.01850769
7x7	0.75λ	0.01764742
6.5x6.5	0.5λ	0.01849609

Table C.1: PML Test 1: Minimum distance from scattering surface to PML. L^2-error norm of pressure taken around the scattering surface with first order elements

PML Thickness	E_Γ
1.25λ	0.01764148
1.00λ	0.01764022
0.75λ	0.01763899
0.50λ	0.01766158
0.25λ	0.01793850
0.10λ	0.01857756

Table C.2: PML Test 2: PML thickness. L^2-error norm of pressure taken around the scattering surface with first order elements

When considering the damping parameter, the results in Table C.3 show a notable increase in error for maximum damping parameter values below $5/\lambda$. A quadratic order for the distribution of this parameter is shown to offer marginally the most accurate approximation in Table C.4.

Maximum Damping Parameter	E_Ω	E_Γ
$50/\lambda$	0.07968349	0.01764312
$25/\lambda$	0.07981215	0.01764002
$10/\lambda$	0.07999116	0.01763899
$5/\lambda$	0.08001582	0.01766350
$2.5/\lambda$	0.08010914	0.01787152
$1/\lambda$	0.08042448	0.01848582

Table C.3: PML Test 3: Maximum Damping Coefficient. L^2-error norm of pressure taken over the domain (excluding PML) and around the scattering surface with first order elements

Damping Parameter Distribution Order	E_Ω	E_Γ
Linear	0.08006912	0.01764901
Quadratic	0.07999116	0.01763899
Cubic	0.08005244	0.01764319
Quartic	0.08001807	0.01766533
Quintic	0.08002142	0.01771507

Table C.4: PML Test 4: Damping Coefficient Distribution. L^2-error norm of pressure taken over the domain (excluding PML) and around the scattering surface with first order elements

C.3.2 Third Order Element Approximation

Contrary to the first order element model, there is a significant increase in the error of the approximation, presented in Table C.5, for the minimum PML distance of 0.5λ when using third order elements. The results from the second test, Table C.6, concerning the thickness of the PML, also demonstrates a clear increase in error for thicknesses of 0.5λ and under.

Domain Size	Minimum Distance	E_Γ
9.5x9.5	2λ	0.00026029
9x9	1.75λ	0.00032578
8.5x8.5	1.5λ	0.00025876
8x8	1.25λ	0.00031822
7.5x7.5	1.0λ	0.00028311
7x7	0.75λ	0.00026719
6.5x6.5	0.5λ	0.00044479

Table C.5: PML Test 1: L^2-error norm of pressure taken around the scattering surface with third order elements

PML Thickness	E_Γ
1.25λ	0.00029873
1.00λ	0.00030485
0.75λ	0.00031822
0.50λ	0.00046778
0.25λ	0.00118162
0.10λ	0.00222518

Table C.6: PML Test 2: L^2-error norm of pressure taken around the scattering surface with third order elements

For the third order element model, Table C.7 shows there is a significant rise in the approximation error for maximum damping parameter values below $10/\lambda$, whilst for the distribution order of this function, there is an obvious increase with cubic and higher order, as shown in Table C.8.

C.4 Conclusion

From the results of this analysis, the PML parameter values used in the scattering model will be: minimum distance from scattering surface to PML = 1.0λ, PML thickness = 0.75λ, maximum damping parameter value = $10/\lambda$, damping parameter distribution order will be quadratic.

Maximum Damping Parameter	E_Ω	E_Γ
$50/\lambda$	0.00047664	0.00029684
$25/\lambda$	0.00047658	0.00029689
$10/\lambda$	0.00053055	0.00031822
$5/\lambda$	0.00157366	0.00067403
$2.5/\lambda$	0.00414338	0.00211859
$1/\lambda$	0.00776359	0.00490590

Table C.7: PML Test 3: L^2-error norm of pressure taken over the domain (excluding PML) and around the scattering surface with third order elements

Damping Parameter Distribution Order	E_Ω	E_Γ
Linear	0.00048027	0.00029996
Quadratic	0.00053055	0.00031822
Cubic	0.00075095	0.00037322
Quartic	0.00114142	0.00049838
Quintic	0.00161333	0.00069066

Table C.8: PML Test 4: L^2-error norm of pressure taken over the domain (excluding PML) and around the scattering surface with third order elements

Appendix D

Spline Interpolation

D.1 Introduction

Spline interpolation generates piecewise polynomial approximations to a curve. The approximating polynomials are defined by a finite number of constraints. These constraints can be information on the positioning of certain points, the tangent or curvature of the function.

D.2 Cubic Spline Interpolation

Cubic spline interpolation approximates a function through a given set of points by generating a third order polynomial in the intervals between two adjacent points, such as

$$f_i(x) = a_i x^3 + b_i x^2 + c_i x + d_i \tag{D.1}$$

For a set of $n+1$ points there will be n expressions of this kind, where n is the number of intervals. The conditions used to evaluate the unknown constants are:

i. The value of the function must be equal at the interior points.

ii. The first and last functions pass through the end points.

iii. The gradient of the function f' at the interior points must be equal.

iv. The curvature of the function f'' at the interior points must be equal.

v. The curvature at the end points of the set is zero.

When these conditions are applied, the expression for the polynomial in each interval can be written as [55]

$$\begin{aligned} f_i(x) = {} & \frac{f_i''(x_{i-1})}{6(x_i - x_{i-1})}(x_i - x)^3 + \frac{f_i''(x_i)}{6(x_i - x_{i-1})}(x - x_{i_1})^3 \\ & + \left[\frac{f(x_{i_1})}{6(x_i - x_{i-1})} - \frac{f''(x_{i-1})(x_i - x_{i-1})}{6}\right](x_i - x) \\ & + \left[\frac{f(x_i)}{6(x_i - x_{i-1})} - \frac{f''(x_i)(x_i - x_{i-1})}{6}\right](x - x_{i-1}) \end{aligned} \tag{D.2}$$

The only unknowns in this equation are the curvature of the function f'' at the ends of the interval. However, if similar equations are stated for all intervals, a system of simultaneous equations is obtained which can be solved for all unknowns. Note that the second derivatives at the end points of the set are taken as zero.

Bibliography

[1] K.S. Yee. Numerical solution of initial boundary value problems involving maxwell's equations in isotropic media. *IEEE Transactions on Antennas and Propagation*, 14(8):302–307, 1966.

[2] R. Holland. Finite difference solutions of maxwell's equations in generalized nonorthogonal coordinates. *IEEE Transactions on Nuclear Science*, 30:4589–4591, 1983.

[3] T.G. Jurgens A. Taflove K. Umashankar T.G. Moore. Finite-difference time-domain modelling of curved surfaces. *IEEE Transactions on Antennas and Propagation*, 40(4):357–366, 1992.

[4] K.S. Yee J.S. Chen A.H. Chang. Conformal finite difference time domain (fdtd) with overlapping grids. *IEEE Transactions on Antennas and Propagation*, 40(9):1068–1075, 1992.

[5] A. Ditkowski K. Dridi J.S. Hesthaven. Convergent cartesian grid methods for maxwell's equations in complex geometries. *Journal of Computational Physics*, 170:39–80, 2001.

[6] O.C. Zienkiewicz. *The Finite Element Method.* McGraw Hill, 3rd edition, 1977.

[7] O.C. Zienkiewicz K. Morgan. *Finite Elements and Approximations.* Dover, 2006.

[8] K. Morgan O. Hassan J. Peraire. Parallel processing for the simulation of problems involving scattering of electromagnetic waves. *Computer Methods in Applied Mechanics and Engineering*, 152:157–174, 1998.

[9] G. Karniadakis S.J. Sherwin. *Spectral/hp Element Methods for CFD.* Oxford University Press, 1999.

[10] L. Demkowicz L. Vardapetyan. Modeling of electromagnetic absorption/scattering problems using *hp* adaptive elements. *Computer Methods in Applied Mechanics and Engineering*, 152:103–124, 1998.

[11] W. Cecot L. Demkowicz W. Rachowicz. A two-dimensional infinite element for maxwell's equations. *Computer Methods in Applied Mechanics and Engineering*, 188:625–643, 2000.

[12] P.D. Ledger K. Morgan O. Hassan N.P. Weatherill. Arbitrary order edge elements for electromagnetic scattering simulations using hybrid meshes and a pml. *International Journal of Numerical Methods in Engineering*, 55:339–358, 2002.

[13] J.S. Hesthaven T. Warburton. Nodal high-order methods on unstructured grids. i. time-domain solution of maxwell's equations. *Journal of Computational Physics*, 181:186–221, 2002.

[14] B. Cockburn C.W. Shu. Runge-kutta discontinuous galerkin methods for convection dominated problems. *Journal of Scientific Computing*, 16(3):173–261, 2001.

[15] J.S. Hesthaven. High-order accurate methods in time-domain computational electromagnetics - a review. *Advances in Imaging and Electron Physics*, 127:59–123, 2002.

[16] D. Komatitsch J.P. Vilotte R. Vai J.M. Castillo-Covarrubias F.J. Sanchez-Sesma. The spectral element method for elastic wave equations - applications to 2-d

and 3-d seismic problems. *International Journal for Numerical Methods in Engineering*, 45:1139–1164, 1999.

[17] D. Komatitsch C. Barnes J. Tromp. Simulation of anisotropic wave propagation based upon a spectral element method. *Geophysics*, 65(4), 2000.

[18] D. Komatitsch R. Martin J. Tromp M.A. Taylor B.A. Wingate. Wave propagation in 2-d elastic media using a spectral element method with triangles and quadrangles. *Journal of Computational Acoustics*, 9:703–718, 2001.

[19] A. Patera. A spectral element method for fluid dynamics: Laminar flow in a channel expansion. *Journal of Computationl Physics*, 54:468–488, 1984.

[20] M.A. Taylor B.A. Wingate. A generalized diagonal mass matrix spectral element method for non-quadrilateral elements. *Applied Numerical Mathematics*, 33:259–265, 2000.

[21] M.A. Taylor B.A. Wingate R.E. Vincent. An algorithm for computing fekete points in the triangle. *SIAM Journal on Numerical Analysis*, 38(5), 2000.

[22] M. Iskandarani D.B. Haidgovel J.P. Boyd. A staggered spectral element model with application to the oceanic shallow water equations. *International Journal for Numerical Methods in Fluids*, 20:393–414, 1995.

[23] F.X. Giraldo T Warburton. A nodal triangle based spectral element method for the shallow water equations on the sphere. *Journal of Computational Physics*, 207:129–150, 2005.

[24] J.F. Claerbout. Coarse grid calculations of waves in inhomogeneous media with application to delineation of complicated seismic structure. *Computer Methods in Applied Mechanics and Engineering*, 35:407–418, 1970.

[25] R. Clayton B. Engquist. Absorbing boundary conditions for acoustic and elastic wave equations. *Bulletin of the Seismological Society of America*, 67:1529–1540, 1977.

[26] J.P. Berenger. A perfectly matched layer for the absorption of electromagnetic waves. *Journal of Computational Physics*, 114:185–200, 1994.

[27] F. Bonnet F. Poupaud. Berenger absorbing boundary condition with time finite-volume scheme for triangular meshes. *Applied Numerical Mathematics*, 25:333–354, 1997.

[28] F.Q. Hu. A stable, perfectly matched layer for linearized euler equations in unsplit physical variables. *Journal of Computational Physics*, 173:455–480, 2001.

[29] J.S. Hesthaven. On the analysis and construction of perfectly matched layers for the linearized euler equations. *Journal of Computational Physics*, 142:129–147, 1998.

[30] E. Turkel A. Yefet. Absorbing pml boundary layers for wave-like equations. *Applied Numerical Mathematics*, 27:533–557, 1998.

[31] O. Hassan K. Morgan N.P. Weatherill. The effect of inaccuracies in geometry modelling on the results of electromagnetic scattering simulations. In *proceedings of the 8th International Conference on Numerical Grid Generation in Computational Field Simulation*, pages 69–80, Honolulu, Hawaii, June 2002.

[32] F. Bassi S. Rebay. High-order accurate discontinuous finite element solution of the 2d euler equations. *Journal of Computational Physics*, 138:251–285, 1997.

[33] L. Krivodonova M. Berger. High-order accurate implementation of solid wall boundary conditions in curved geometries. *Journal of Computational Physics*, 211:492–512, 2006.

[34] R.W. Davies. *Solution of Wave Scattering Problems using a Spectral Element Method on 2D Quadrilateral Grids*. MRes thesis, University of Wales Swansea, 2005.

[35] C.A. Balanis. *Advanced Engineering Electromagnetics.* John Wiley & Sons, New York, 1989.

[36] G.N. Watson. *A Treatise on the Theory of Bessel Functions.* Cambridge University Press, 2nd edition, 1962.

[37] D.G. Duffy. *Solutions of Partial Differential Equations.* Tab Books Incorporated, 1986.

[38] G.T. Ruck D.E. Barrick W.D. Stuart C.K. Krichbaum. *Radar Cross Section Handbook.* Plenum Press, 1970.

[39] K. Morgan O. Hassan J. Peraire. A time domain unstructured grid approach to the simulation of electromagnetic scattering in piecewise homogeneous media. *Computer Methods in Applied Mechanics and Engineering,* 134:17–36, 1996.

[40] O.C. Zienkiewicz R.L. Taylor P. Nithiarasu. *The Finite Element Method for Fluid Dynamics.* Elsevier Butterworth-Heinemann, 6th edition, 2005.

[41] J. Donea A. Huerta. *Finite Element Methods for Flow Problems.* John Wiley & Sons, 2003.

[42] G.D. Smith. *Numerical Solution of Partial Differential Equations.* Oxford University Press, 3rd edition, 2004.

[43] J. Lee R. Lee A. Cangellaris. Time-domain finite element methods. *IEEE Transactions on Antennas and Propagation,* 45(3), 1997.

[44] Q. Chen I. Babuska. Approximate optimal points for polynomial interpolation of real functions in an interval and in a triangle. *Computer Methods in Applied Mechanics and Engineering,* 128:405–417, 1995.

[45] K. Morgan M. El hachemi O. Hassan N.P. Weatherill. Explicit time domain finite element methods for electromagnetics. *Frontiers of Computational Fluid Dynamics 2006, World Scientific,* pages 161–181, 2005.

[46] J. Donea S. Giuliani. A simple method to generate high-order accurate convection operators for explicit schemes based on linear finite elements. *Journal for Numerical Methods in Fluids*, 1:63–79, 1981.

[47] R.W. Davies K. Morgan O. Hassan. A time domain spectral element method for acoustic scattering problems. In *proceedings of the 14th ACME Conference*, pages 91–94, Queen's University Belfast, April 2006.

[48] E. Kreyszig. *Advanced Engineering Mathematics*. John Wiley & Sons, 8th edition, 1999.

[49] M. Zhang C-W. Shu. An analysis of and a comparison between the discontinuous galerkin and the spectral finite volume methods. *Computers & Fluids*, 34(4-5):581–592, 2005.

[50] P.L. Roe. Approximate riemann solvers, parameter vectors and difference schemes. *Journal of Computational Physics*, 43:357–372, 1981.

[51] N.P. Weatherill O. Hassan. Efficient three-dimensional delaunay triangulation with automatic point creation and imposed boundary constraints. *International Journal for Numerical Methods in Engineering*, 37(12):2005–2039, 1994.

[52] H. Luo J.D. Baum R. Lohner. A fast, p-multigrid discontinuous galerkin method for compressible flows at all speeds. In *proceedings of the 44^{th} AIAA Aerospace Sciences Meeting and Exhibit*, Reno, Nevada, January 2006.

[53] B. Szabo I. Babuska. *Finite Element Analysis*. John Wiley & Sons, 1991.

[54] P.D. Ledger. *An* hp-*Adaptive Finite Element Procedure for Electromagnetic Scattering Problems*. PhD thesis, Swansea University, Singleton Park, Swansea, 2001.

[55] S.C. Chapra R.P. Canale. *Numerical Methods for Engineers*. WCB/McGraw-Hill, Singapore, 3rd edition, 1998.

[56] A.Z. Elsherbeni M. Hamid. Scattering by parallel conducting circular cylinders. *IEEE Transactions on Antennas and Propagation*, 35(3):355–358, 1987.

[57] G. James. *Advanced Modern Engineering Mathematics*. John Wiley & Sons, 2003.